NUMERICAL STUDY OF CONVECTIVE HEAT TRANSFER IN FLAT TUBE HEAT EXCHANGERS OPERATING IN SELF-SUSTAINED OSCILLATORY FLOW REGIMES

A Dissertation

by

TRACY LEO FULLERTON

Submitted to the Office of Graduate Studies of
Texas A&M University
in partial fulfillment of the requirements for the degree of

DOCTOR OF PHILOSOPHY

December 2011

Major Subject: Mechanical Engineering

Numerical Study of Convective Heat Transfer in Flat Tube Heat Exchangers Operating in Self-Sustained Oscillatory Flow Regimes

NUMERICAL STUDY OF CONVECTIVE HEAT TRANSFER IN FLAT TUBE HEAT EXCHANGERS OPERATING IN SELF-SUSTAINED OSCILLATORY FLOW REGIMES

A Dissertation

by

TRACY LEO FULLERTON

Submitted to the Office of Graduate Studies of
Texas A&M University
in partial fulfillment of the requirements for the degree of

DOCTOR OF PHILOSOPHY

Approved by:

Chair of Committee,	N. K. Anand
Committee Members,	Dennis O'Neal
	Gerald Morrison
	H. C. Chen
Head of Department,	J. A. Caton

December 2011

Major Subject: Mechanical Engineering

ABSTRACT

Numerical Study of Convective Heat Transfer in Flat Tube Heat Exchangers Operating in Self-Sustained Oscillatory Flow Regimes. (December 2011)

Tracy Leo Fullerton, B.S.; M.S., Texas Tech University

Chair of Advisory Committee: Dr. N. K. Anand

Laminar, two-dimensional, constant-property numerical simulations of flat tube heat exchanger devices operating in flow regimes in which self-sustained oscillations occur were performed. The unsteady flow regimes were transition flow regimes characterized by cyclic variations of flow parameters such as stream-wise or cross-stream velocity.

A computer code was developed to perform the numerical simulations. Spatial discretization was based upon a Control Volume Finite Element Method (CVFEM). Temporal discretization was based upon a semi-implicit Runge-Kutta method. Double Cyclic conditions were used to limit the numerical domains to one repeating geometric module.

Nine geometric domains representing flat tube heat exchanger devices were tested over a range of Reynolds numbers. A maximum Reynolds number (*Re*) of 2000 was established to keep the study within the transition range. For each domain, a critical Reynolds number (Re_{crit}) was found such that for $Re < Re_{crit}$ the flow was steady, laminar flow and for $Re > Re_{crit}$ the flow exhibited cyclic oscillations. For the cases tested, the

variation in longitudinal pitch had little impact on the Re_{crit} value for a fixed transverse pitch. However, for a fixed longitudinal pitch, the Re_{crit} was increased for decreasing transverse pitch.

The results demonstrate the importance of using unsteady simulation methods for these cases. Nusselt numbers predicted by the unsteady method were on the order of 65% higher than predicted by steady methods for the same Reynolds numbers.

Data for required pumping power versus resultant Nusselt number were collected which showed four distinct operating regions for these devices spanning the low Reynolds number, steady flow region through the self-sustained oscillating flow region. Based on the data, the recommended operating region is the region of self-sustained oscillations as this region is characterized by the highest increase in Nusselt number per increase in required pumping power.

DEDICATION

To Sophie.

ACKNOWLEDGEMENTS

I would like to thank my committee chair, Dr. Anand, and my committee members, Dr. O'Neal, Dr. Morrison, and Dr. Chen for their guidance and support throughout the course of this research.

Special thanks go to Dr. Anand who allowed me the freedom to pursue a course of research of my choosing and for supporting me in every conceivable way.

Thanks to Mr. Vernon R. Goldberg who has been a mentor and friend.

Thanks to my mother and father.

Thanks to friends and family still with us and to those that have passed.

This research was supported by the *James and Ada Forsyth Professorship* endowment funds.

NOMENCLATURE

a's and b's	Coefficients in discretization equations
A, B, and C	Coefficients in interpolation functions
A_{cs}	Cross-sectional area of domain
A^{nbe}	Area of neighboring element
AR	Tube aspect ratio
AREA	Area of element
$C_{D,press}$	Pressure drag coefficient
$C_{D,skin}$	Skin friction coefficient
c_p	Fluid specific heat
D_h	Hydraulic diameter
D_{min}	Tube minimum diameter
D_{maj}	Tube maximum diameter
f	Friction factor
freq	Oscillation frequency
Gap_L	Longitudinal distance between columns of tubes
Gap_T	Transverse distance between rows of tubes
H	Domain height
HEM	Heat exchange module
Hz	Hertz (1/s)
$\overline{J}$	Flux vector

$\overline{J}^{EV}$	Flux vector based on element velocity
k	Fluid thermal conductivity
L	Domain length
m	Periodicity
$\dot{m}$	Mass flow rate
nbe	Neighboring element
$\hat{n}$	Normal vector to element link
Nu	Nusselt number
P	Pressure
Pe	Peclet number
Pr	Prandtl number
$\hat{P}$	Locally varying pressure
$\overline{PTP}$	Normalized peak-to-peak amplitude of oscillation
P_L	Longitudinal pitch
P_T	Transverse pitch
$q"$	Heat flux
Q	Total heat added per module
Re	Reynolds number
Re_{crit}	Critical Reynolds number
Re_{max}	Maximum Reynolds number
S	Source term in transport equation

Str	Strouhal number (non-dimensional frequency)
S_L	Non-dimensional longitudinal pitch
S_T	Non-dimensional transverse pitch
T	Temperature
$\hat{T}$	Locally varying temperature
T_b	Bulk temperature
T_s	Surface temperature
$\hat{T}_b$	Locally varying bulk temperature
$\hat{T}_s$	Locally varying surface temperature
u	Stream-wise velocity
$\tilde{u}$	Stream-wise component of element velocity
$\overline{u}_{inlet}$	Average stream-wise velocity at domain inlet
U_{avg}	Average velocity within an element
v	Cross-stream velocity
$\tilde{v}$	Cross-stream component of element velocity
$\overline{v}$	Velocity vector
$\tilde{\overline{v}}$	Element velocity vector
W	Width of domain (W=1 for 2D)
(x, y)	Global coordinates
(X,Y)	Element local coordinates

Greek Symbols

β	Global pressure gradient
γ	Global temperature gradient
θ_{arc}	Included angle in chord across arc for meshing tube
λ_i	Coefficient in integrated flux expression
μ	Fluid dynamic viscosity
ν	Fluid kinematic viscosity
ρ	Fluid density
ϕ	General transported scalar
χ	General field variable
ψ	Non-dimensional pumping power
Γ	Fluid diffusion coefficient
Φ	Non-dimensional pumping power (Amon)
Φ_{link}	Integrated flux
Ω	Dimensionless frequency

Abbreviations and Acronyms

2D	Two-dimensional
3D	Three-dimensional
CTDMA	Cyclic Tri-Diagonal Matrix Algorithm
CV	Control Volume
CVFEM	Control Volume Finite Element Method

DC	Double Cyclic
ESDIRK	Explicit first stage, Single diagonal coefficient, Diagonally Implicit, Runge-Kutta
FE	Finite Element
FV	Finite Volume
LHS	Left-Hand Side
PFD	Periodically Fully-Developed
RHS	Right-Hand Side
SSOF	Self-Sustained Oscillating Flow
TDMA	Tri-Diagonal Matrix Algorithm
TS	Tollmien-Schlichting

TABLE OF CONTENTS

Page

ABSTRACT iii

DEDICATION v

ACKNOWLEDGEMENTS vi

NOMENCLATURE vii

LIST OF FIGURES xv

LIST OF TABLES xviii

1. INTRODUCTION 1

2. THEORY AND LITERATURE REVIEW 5

2.1 Flat Tube Flow and Heat Transfer 5
2.2 Self-Sustained Oscillatory Flows 7
2.2.1 Grooved Channel and Communicating Channel 9
2.2.2 Arrays of Rectangular Tubes 14
2.3 Summary 16

3. NUMERICAL METHODS 18

3.1 Overview 18
3.2 General Transport Equation 19
3.3 Control Volume Finite Element Method (CVFEM) 21
3.3.1 Overview 21
3.3.2 Element Velocity and the General Transport Equation 22
3.3.3 Domain Discretization 23
3.3.4 Flux Integration for $\phi = u, v, or T$ 25
3.3.5 Integration of Source Term 28

Page

3.3.6 Momentum Equations 29
3.3.7 Energy Equation 30
3.3.8 Definition of Element Velocity 30
3.3.9 Solution for Nodal Pressure 32
3.3.10 Boundary Conditions and Solution Process 33
3.4 ESDIRK 34
3.5 Periodically Fully-Developed Flow and Double Cyclic Conditions 38
3.5.1 Periodically Fully Developed (PFD) Flow 38
3.5.2 Double Cyclic Conditions 42
3.6 Parameter Definitions 43
3.6.1 Reynolds Number 43
3.6.2 Friction Factor for PFD/DC Solution 44
3.6.3 Bulk Temperature and Nusselt Number for PFD/DC Solution 44
3.6.4 Strouhal Number 45
3.6.5 Non-Dimensional Pumping Power 46
3.6.6 Tube Drag Coefficients 47

4. CODE VALIDATION 49

4.1 Steady Validation 49
4.2 Unsteady Validation 52
4.3 Previously Published Work 54
4.3.1 Fullerton and Anand [5] 54
4.3.2 Fullerton and Anand [30] 57

5. RESULTS AND DISCUSSION 64

5.1 Domain Geometry 64
5.2 CVFEM Mesh 66
5.3 Grid Independence Study 68
5.4 Time Step Independence 72
5.5 Unsteady Solutions 73
5.5.1 Note on Required Solution Times 74

Page

5.5.2 Tabular Listing of Unsteady Results 75
5.5.3 Notes on Unsteady Solution Characteristics 76
5.6 Steady Solutions 81
5.6.1 Tabular Listing of Steady Results 82
5.7 Estimation of Re_{crit} 86
5.8 Discussion of Flow Results 89
5.8.1 General Characterization of the Flow Oscillations 89
5.8.2 Skin Friction and Pressure Drag 90
5.8.3 Stream Function Plots 91
5.8.4 Pumping Power 92
5.9 Discussion of Heat Transfer Results 96
5.10 Discussion of Combined Flow and Heat Transfer 98

6. SUMMARY 105

6.1 Recommendations for Future Work 107

REFERENCES 109

APPENDIX A 113

APPENDIX B – INTERPOLATION FUNCTION FOR ϕ WITHIN AN ELEMENT 138

APPENDIX C – FLUX INTEGRATION FOR ELEMENT LINKS 141

APPENDIX D - CV COEFFICIENT ASSEMBLY PROCESS 148

APPENDIX E – INTERPOLATION FUNCTION FOR PRESSURE *(P)* 152

VITA 154

LIST OF FIGURES

Page

Figure 1-1. A flat tube and its orientation with respect to the flow.....1

Figure 2-1. U-velocity at a point: (a) steady flow; (b) SSOF; (c) turbulent flow.....8

Figure 2-2. (a) Grooved channel geometry; (b) communicating channel geometry. 9

Figure 2-3. Rectangular tube arrays: (a) inline; (b) staggered.....15

Figure 3-1. CVFEM domain discretization: (a) typical element; (b) internal CV; (c) boundary CV. 24

Figure 4-1. Computational domain for steady, developing-flow code validation.....50

Figure 4-2. Comparison of current work to Zhang *et al.* [14] for rectangular tubes: (a) friction factor versus Reynolds number; (b) j factor versus Reynolds number. 53

Figure 4-3. Computational domain geometries for Fullerton and Anand [5]: (a) round tube; (b) flat tube; (c) oval tube. 55

Figure 4-4. Heat transfer enhancement ratio versus Reynolds number for Fullerton and Anand [5]: (a) Pr=0.7; (b) Pr=7.0. 56

Figure 4-5. Heat transfer performance ratio versus Reynolds number for Fullerton and Anand [5]: (a) Pr=0.7; (b) Pr=7.0. 57

Figure 4-6. Diagram describing the alternative method. 59

Figure 4-7. Staggered plate domains for Fullerton and Anand [30]: (a) PFD flow domain; (b) DF temperature domain. 62

Figure 4-8. Plot of (*fRe*)/96 from various sources [30]. 62

Figure 4-9. Plot of *Nu*/7.54 versus *Re* from various sources [30]. 63

Figure 5-1. Computational domain geometry: staggered array of flat tubes.....65

Figure 5-2. Typical CVFEM element mesh. 68

Page

Figure 5-3. Comparison of domains used for grid independence study: (a) SL7_ST2; (b) SL8_ST3.....69

Figure 5-4. Oscillating u-velocity at a point for two values of β.....80

Figure 5-5. Reynolds number versus time for two values of β.....80

Figure 5-6. Estimation of Re_{crit} from steady and unsteady β v. Re curves. 88

Figure 5-7. Stream function plots for one period of oscillation (τ) for SL7.5_ST2.5 at Re=2025.6.....93

Figure 5-8. Non-dimensional pumping power (ψ) versus Reynolds number: constant S_T plots.....94

Figure 5-9. Non-dimensional pumping power (ψ) versus Reynolds number: constant S_L plots.....95

Figure 5-10. Nusselt number versus Reynolds number for unsteady SL7.5 cases.....97

Figure 5-11. Nusselt number versus Reynolds number for SL7.5_ST2.5: unsteady and steady data.....97

Figure 5-12. Non-dimensional pumping power (ψ) versus Nusselt number: constant S_T plots.....101

Figure 5-13. Non-dimensional pumping power (ψ) versus Nusselt number: constant S_L plots.....102

Figure 5-14. Non-dimensional pumping power (ψ) versus Nusselt number: SL7.5_ST2.5 (Extended). 103

Figure 5-15. Non-dimensional pumping power (ψ) versus Nusselt Number: SL7.5_ST2.5 (steady only). 104

Figure 5-16. Non-dimensional pumping power (ψ) versus Nusselt Number: SL7.5_ST2.5 (unsteady only). 104

Figure C-1. CVFEM domain discretization: (a) typical element; (b) internal CV; (c) boundary CV. 141

Page

Figure D-1. Typical internal CV formed from four elements. 149

Figure D-2. Exploded view of Figure D-1 showing individual elements. 149

LIST OF TABLES

Page

Table 3-1. Definitions of ϕ, Γ, and S for the general transport equation 20

Table 3-2. Definitions of ϕ, Γ, and S for PFD flow conditions 42

Table 4-1. Comparison of average Nusselt numbers 50

Table 4-2. Flow results for parallel plate example 51

Table 5-1. Definition of domain geometries 66

Table 5-2. Description of SL7_ST2 meshes for grid independence study 69

Table 5-3. Grid independence results: SL7_ST2 at $\beta = 4.0$ 70

Table 5-4. Description of SL8_ST3 meshes for grid independence study 71

Table 5-5. Grid independence results: SL8_ST3 at $\beta = 1.25$ 71

Table 5-6. Description of meshes for all computational domains 72

Table 5-7. Unsteady data for SL7 cases 77

Table 5-8. Unsteady data for SL7.5 cases 78

Table 5-9. Unsteady data for SL8 cases 79

Table 5-10. Steady data for SL7 cases 83

Table 5-11. Steady data for SL7.5 cases 84

Table 5-12. Steady data for SL8 cases 85

Table 5-13. Estimated values of Re_{crit} 89

1. INTRODUCTION

The use of flat tubes in heat exchangers has become common, especially in the automotive air conditioning industry. [1] [2] Figure 1-1 shows the geometry of a typical flat tube. Tubes of this shape are available commercially in a variety of sizes. Because of their lower profile, external "air-side" pressure drop characteristics of flat tubes are generally better than those for round tubes. With proper design, one may expect the heat transfer performance of a flat tube heat exchanger to rival that of a round tube heat exchanger. However, there is a shortage of data in the literature for flat tube performance, either as individual tubes or in tube banks. Published studies include only steady, laminar data or unsteady data at relatively low Reynolds numbers. Data for flat tubes operating in unsteady flow conditions at moderate to high Reynolds numbers is lacking.

Figure 1-1. A flat tube and its orientation with respect to the flow.

For some flow domains, including tube-in-cross-flow domains, one of the transition pathways from steady, laminar flow to fully turbulent flow is a flow regime characterized by self-sustained oscillations in velocity. This transition flow regime is characterized by velocities that vary with time, but in a repeating or cyclic manner, as

---

This dissertation follows the style and format of *Numerical Heat Transfer*.

opposed to the random oscillations observed in fully turbulent flows. These oscillations provide additional mixing of fluid layers which leads to thinner thermal boundary layers and subsequently to enhanced heat transfer. The same may be said of turbulent flow oscillations, however, the oscillations in this oscillatory transition flow regime are expected to have smaller friction losses associated with them as compared to those in fully turbulent flows. Operating a heat exchanger device in this oscillatory transition regime, one may expect an increase in heat transfer compared to operating in a steady, laminar flow regime. There may also be advantages to operating in this oscillatory transition regime as compared to operating in a fully turbulent regime.

The current work consists of a numerical study of the performance of simple flat tube heat exchanger devices operating in the oscillatory transition flow regime described above. Solutions to test problems for steady, laminar flow and for the transitional oscillatory regime were obtained for performance comparison for several two-dimensional (2D) domains of varying geometry. For all cases, data were collected for flow performance in terms of Reynolds number (*Re*), friction factor (*f*), and non-dimensional pumping power (ψ) and for heat transfer performance in terms of Nusselt number (*Nu*). Other collected data include tube skin friction, tube pressure drag, non-dimensional frequency of oscillation (Strouhal number (*Str*)), and peak-to-peak magnitude of oscillations ($\overline{PTP}$).

An original computer code was developed to perform the numerical study for the current work. There are three features of these oscillating flows and their associated geometric domains that had to be addressed in the development of the code. First, as

seen in Figure 1-1, the flat tube geometry has radiused ends. The chosen method must therefore be capable of handling irregular geometric features such as this. Second, while the oscillations of parameters such as velocities are cyclic, the flow is still unsteady and the chosen method must be capable of solving unsteady flow problems. Third, the solution of these unsteady problems was expected to be very resource intensive in terms of computer hardware and solution time. Fortunately, the regular geometric spacing of tubes which promote the transitional oscillatory flows also lead to periodically fully-developed (PFD) flows. Imposing PFD flow conditions on a numerical solution allow solution for just one domain module of several identical modules. Imposing PFD flow conditions limits the size of the domain and makes for more efficient use of computer resources.

Features of the code were developed and validated over the course of the project. The basis for this code is a Control Volume Finite Element Method (CVFEM) as described in the literature. This method features a triangular element mesh allowing irregular geometric features to be modeled easily. The development of this original code began with a steady-flow version for 2D laminar constant-property flows. This was followed by steady-flow versions which incorporated PFD flow conditions and the related Double Cyclic (DC) conditions. Finally, unsteady versions of the code were developed using a semi-implicit Runge-Kutta method. At each stage of development, the code was validated using published or theoretical data. While the three features of the code are not original, the combination of these three features into one computer code is original.

This dissertation is organized into six sections. Section 2 presents a discussion of flat tube performance based on published results. Section 2 also includes a discussion of the theory behind self-sustained oscillating flow and presentation of some published performance data. Section 3 describes the numerical methods used to conduct the current work. This section includes a discussion of CVFEMs and the semi-implict Runge-Kutta method chosen. Section 3 also includes a discussion of periodically fully-developed flow and Double Cyclic conditions and how the implementation of these conditions in the code limit the required solution domain to one repeating module. Section 4 presents code validation data for both steady and unsteady cases. Section 4 also describes previously published work. Section 5 presents the results from the current study of flat tube heat exchanger devices. Section 6 presents a summary of the current work and recommendations for continuation of this effort.

2. THEORY AND LITERATURE REVIEW

As stated in Section 1 above, for the current work the primary interest is the performance of flat tube heat exchanger devices operating in flow regimes that exhibit self-sustained oscillations. This section will provide a discussion of relevant theory and literature references for both flat tube flow/heat transfer and for self-sustained oscillations.

2.1 Flat Tube Flow and Heat Transfer

While flat tubes have gained popularity and acceptance in some industries, especially in the air conditioning industry, there are few references in the literature discussing the performance of flat tubes in heat exchanger devices. [2]

Bahaidarah *et al.* [3] performed a numerical study of the performance of banks of flat tubes under 2D steady, laminar, constant-property conditions at Reynolds numbers between 25 and 400. This study included cases of flat tubes arranged in both inline and staggered configurations for varying longitudinal and transverse spacing of tubes. The results indicated that, in general, flat tubes did not perform as well as equivalent round tubes under the same conditions when only heat transfer was considered. However, when both heat transfer and pumping power were considered, the flat tube outperformed the equivalent round tube. Due to the flat tube's lower profile for the equivalent heat transfer area, the pressure drop required for a given flow rate was less for the flat tube than for the round tube thereby making the pumping power and operating cost less. Another conclusion was that the staggered configurations out-performed the inline configurations from a heat transfer standpoint.

Bahaidarah *et al.* [4] also considered flat tubes as part of a numerical study of round tubes and non-circular tubes. For these 2D steady, laminar, constant-property cases, a row of tubes confined between parallel plates was studied for varying Reynolds number flows. One of the main conclusions from this study was that for Re >50, when both heat transfer and pumping power were considered, the flat tube outperformed the equivalent round tube.

Fullerton and Anand [5] performed a 2D steady, laminar, constant-property study of flat tubes, circular tubes, and oval tubes similar to Bahaidarah *et al*. [4]. In this study, periodically fully-developed conditions were imposed for the numerical simulation of a row of tubes between two flat plates. Reynolds numbers between 50 and 350 were considered for fluids of Prandtl number 0.7 and 7.0. The results were similar to those from [3] and [4] above. When both heat transfer and pumping power were considered, the flat tube outperformed the equivalent round tube. (This paper, Fullerton and Anand [5] appears in its entirety as Appendix A.)

Benarji *et al.* [6] performed a numerical study of unsteady cases over inline and staggered banks of flat tubes. The geometry and Reynolds number range were the same as for Bahaidarah *et al.* [3] above. Fluids of Prandtl number 0.7 and 7.0 were considered. Few transient effects were reported. Only transient start-up conditions were seen due to the low Reynolds number range considered. The cases tested all converged to a steady state. No self-sustained oscillations were reported. Also, symmetry was used in such a way that unsteady oscillatory effects would have been prevented.

The literature review for flat tube data is brief due to the lack of references. However, there does seem to be a consensus that flat tubes have a performance advantage over other tube shapes under certain steady operating conditions if both heat transfer performance and cost of operation in terms of pumping power are considered.

2.2 Self-Sustained Oscillatory Flows

Self-sustained oscillatory flows (SSOFs) are flows in which velocities and other quantities at a specific location vary with time in a periodic manner. The oscillations in such flows occur naturally in that they are not induced by artificially varying the flow rate or by inducing oscillations mechanically. Figure 2-1 demonstrates the difference between steady laminar flow, self-sustained oscillatory flow, and fully turbulent flow by comparing plots of u-velocity versus time at a point. Figure 2-1(a) shows the plot of u versus t for a steady flow. Since the u-velocity is constant with time for steady flow, the plot is a horizontal line. Figure 2-1(b) shows the plot of u versus t for a point in a self-sustained oscillatory flow. In this case, while u varies with time, the variation is cyclic and repeats itself with time. Figure 2-1(c) shows the plot of u versus t for a point in a fully turbulent flow. In this case, the variation of u with time is not periodic but appears random.

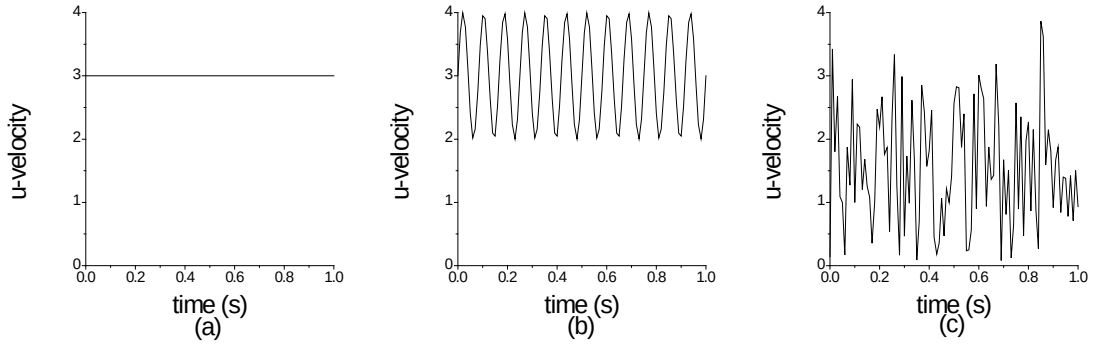

Figure 2-1. U-velocity at a point: (a) steady flow; (b) SSOF; (c) turbulent flow.

These SSOFs lie on the path of transition from steady, laminar flow to fully turbulent flow for certain flow geometries and flow conditions. One type of domain geometry for which self-sustained oscillations have been observed and studied is a flow domain having regularly spaced geometric features such as fins, plates, or tubes. For some, but not necessarily all, such geometries, as Reynolds number is increased from low-speed, steady, laminar flow, a critical Reynolds number (Re_{crit}) is reached above which the flow is unsteady and characterized by periodic oscillations.

Self-sustained oscillatory flows are of interest for heat exchanger devices because the oscillations of *u*- and *v*-velocities enhance mixing and keep thermal boundary layers from growing, both of which enhance heat transfer rates.

Combining SSOFs with flat tubes is attractive because operating in a SSOF regime may help to increase heat transfer performance of flat tubes. Pressure drop requirements, and therefore pumping power requirements, are expected to be higher than for steady flows, but if heat transfer performance increases at a faster rate than the pressure drop increases, a net gain in performance may be realized.

2.2.1 Grooved Channel and Communicating Channel

SSOFs have been observed and studied for several flow geometries associated with heat exchangers. Two such geometries are the grooved channel geometry and the communicating channel geometry as shown in Figure 2-2. Both geometries exhibit regularly spaced geometric features, which, as stated above, may lead to self-sustained oscillations under certain conditions.

Several references may be found in the literature related to these two problems. The reported results share some commonality. The commonalities will be discussed first, followed by a discussion of specific references.

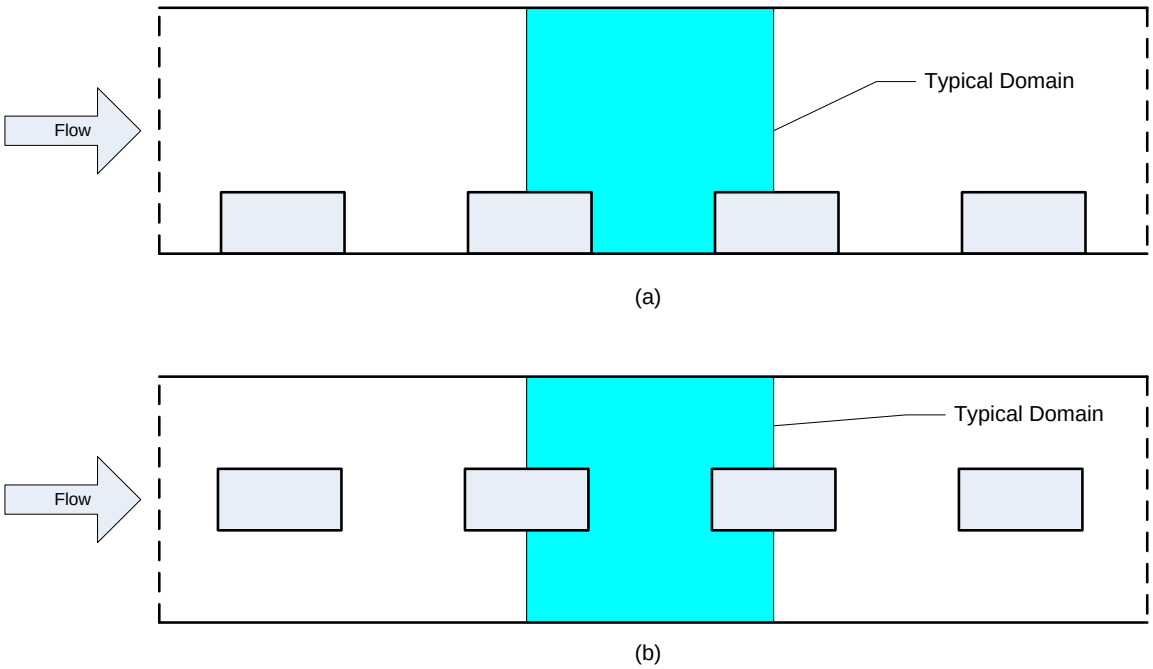

Figure 2-2. (a) Grooved channel geometry; (b) communicating channel geometry.

2.2.1.1 General Characteristics

Both the grooved channel and communicating channel geometries may be viewed as plane channels with periodically-spaced geometric disturbances. At low Reynolds numbers, the flow is steady. As the Reynolds number is increased, a critical Reynolds number Re_{crit} is reached and the flow undergoes a Hopf bifurcation and transitions from steady, laminar flow to flow characterized by self-sustained oscillations. A Hopf bifurcation occurs when a steady solution is unstable to an oscillatory disturbance. In this case, the flow bifurcates into a periodic solution of a particular frequency. [7] As the Reynolds number is increased further, the magnitude and frequency of the oscillations increases. As the Reynolds number is increased still further, the oscillations begin exhibiting the randomness associated with turbulent flow.

For both geometries, the frequency of oscillation is closely tied to the frequency of Tollmien-Schlichting (TS) waves predicted for the plane channel flow by linear and nonlinear stability analysis. TS waves exist due to the viscous interaction between the channel walls and the fluid. These TS waves are present in plane channel flow, but are stable up a Reynolds number of approximately 5772. For both the grooved channel and communicating channel flows, the periodically spaced obstructions trigger oscillations for existing modes at lower Reynolds numbers that would otherwise be stable in plane channel flow. The oscillations are stabilized by nonlinear forces.

For both geometries, oscillations were observed for domains of varying periodicity. Here, the term periodicity refers to the number of identical repeating modules included in the solution domain. For example, if only one module is included,

that is referred to as a periodicity *m=1* condition. If two modules are included, this is a periodicity *m=2* condition, and so forth. Published results indicate that different frequencies of oscillation may be found depending upon the periodicity of the solution domain.

For both geometries, if constant heat flux is applied to the bounding plates, the heat transfer is enhanced compared to the plane channel flow. First, the presence of the obstructions enhances heat transfer at $Re<Re_{crit}$ due to the breakup of the thermal boundary layer in the channel flow. Second, after the onset of self-sustained oscillations, mixing of fluid layers is greatly enhanced which also enhances heat transfer.

2.2.1.2 Specific References

Ghaddar *et al.* [8] studied the grooved channel problem. They used linear stability to predict the critical Reynolds number for varying grooved channel geometries. The critical Reynolds numbers were found to be shifted only slightly from those predicted by both linear and nonlinear stability theory. They also demonstrated a square root relationship between the amplitude of oscillation and the degree of criticality ($Re-Re_{crit}$) that suggested the behavior was associated with a regular Hopf bifurcation.

Majumdar and Amon [9] studied the communicating channel problem. They performed a numerical study for 2D constant-property cases using a spectral element method. The authors considered this communicating channel domain to be two plane channels separated by the row of obstructions along the centerline as shown in Figure 2-2(b). As part of their study, the authors predicted TS wave frequencies for the plane channel flows above and below the row of obstructions. Their results showed that for

cases of self-sustained oscillatory flow for the communicating channel geometry, there was only a minor shift in oscillation frequency from predictions based on plane TS waves to the observed oscillations in the flow. According to their results, the oscillations were the result of a primary Hopf bifurcation. The primary channel flow was unstable to small disturbances but at $Re>Re_{crit}$, nonlinear affects stabilized the flow such that time periodic self-sustained oscillations resulted. From their results, Majumdar and Amon concluded that self-sustained oscillatory flows are ordered flows compared to turbulent flows. Ordered supercritical flows require less pumping power than turbulent flow to achieve the same transport rates. Also, a self-sustained oscillatory flow has less viscous dissipation than turbulent flow. These conclusions are of interest when one considers pumping power as a cost of operation of a device.

Amon and Mikic [10] studied the communicating channel problem. They performed a numerical study for 2D constant-property cases using a spectral element method. According to their results, the match of TS frequencies depends on depth of the plate and width of the gap along the domain centerline. They also caution that the domain with periodicity $m=1$ may or may not give the least stable mode. It is possible that a domain with periodicity of $m=2$, $m=3$, or higher may produce the lowest Re_{crit}. They also reported that while heat transfer increased for these oscillating cases, that the required pressure drop to drive the flow also increased. They defined a non-dimensional pumping power based on required pressure drop and showed that pumping power is proportional to $(Nu\ Re^2)$ for these flows. They stated that self-sustained oscillatory

flows have less viscous dissipation than turbulent flows and therefore require less pumping power to achieve same transport rate.

In Mujumdar and Amon [11], the authors apply techniques usually associated with turbulent flow to study the kinetic energy equation term-by-term. One interesting result was a difference between these SSOFs and turbulent flows. They found that the pressure term contributed to the production of kinetic energy for SSOF, but for turbulent flows the contribution of the pressure fluctuations was almost negligible.

In Amon *et al.* [12], both numerical and experimental work was performed with communicating channels. Good agreement was obtained between numerical and experimental results. The results confirmed that the presence of the plates along the centerline of the channel enhanced heat transfer compared to plane channel flow even for steady flow cases $Re<Re_{crit}$. After the onset of SSOF, the heat transfer rates were enhanced at an even greater rate. A plot of *Nu* versus *Re* shows a steeper slope for $Re>Re_{crit}$.

Guzman *et al.* [13] studied the transition scenario for the communicating channel problem. For the geometry and flow conditions used, they found the least stable frequency to occur in a domain of period $m=2$. As the pressure drop driving the flow was increased, the flow underwent a Hopf bifurcation to an oscillatory mode with a $Re<Re_{crit}$. As the pressure drop was increased further, second Hopf bifurcation was observed and accompanied by a further increase in *Re*.

2.2.2 Arrays of Rectangular Tubes

Two other geometries for which self-sustained oscillations have been observed and studied are inline and staggered arrangements of rectangular fins or tubes. Figure 2-3(a) and Figure 2-3(b) show the inline and staggered arrangements, respectively. In both geometric domains, the tubes are periodically arranged in both the stream-wise and cross-stream direction whereas in the grooved channel and communicating channel, the interruptions were arranged only in the stream-wise direction.

In Zhang *et al.* [14], a numerical study was conducted to isolate the heat transfer and friction effects associated with two mechanisms: the prevention of the continuous growth of thermal boundary layers at both steady and oscillatory modes, and the increased mixing due to oscillatory modes.

For both tube arrangements, the flow showed the same characteristics as *Re* was increased from a low value. The flow was in a steady, laminar state up to Re_{crit}. For $Re>Re_{crit}$, self-sustained oscillations occurred at a single frequency. As *Re* was increased, another low frequency was observed followed by random fluctuations. The Strouhal number (non-dimensional frequency) remained relatively constant throughout although a slight increase was observed as the second low frequency appeared.

Conclusions from this work were that steady simulation under-predicts both heat transfer and friction because it misses the effects of the oscillations. Vortices generated at the leading edge of the rectangular tube roll down the top and bottom of each tube enhancing local Nusselt number and decreasing skin friction due to flow reversal. Flow

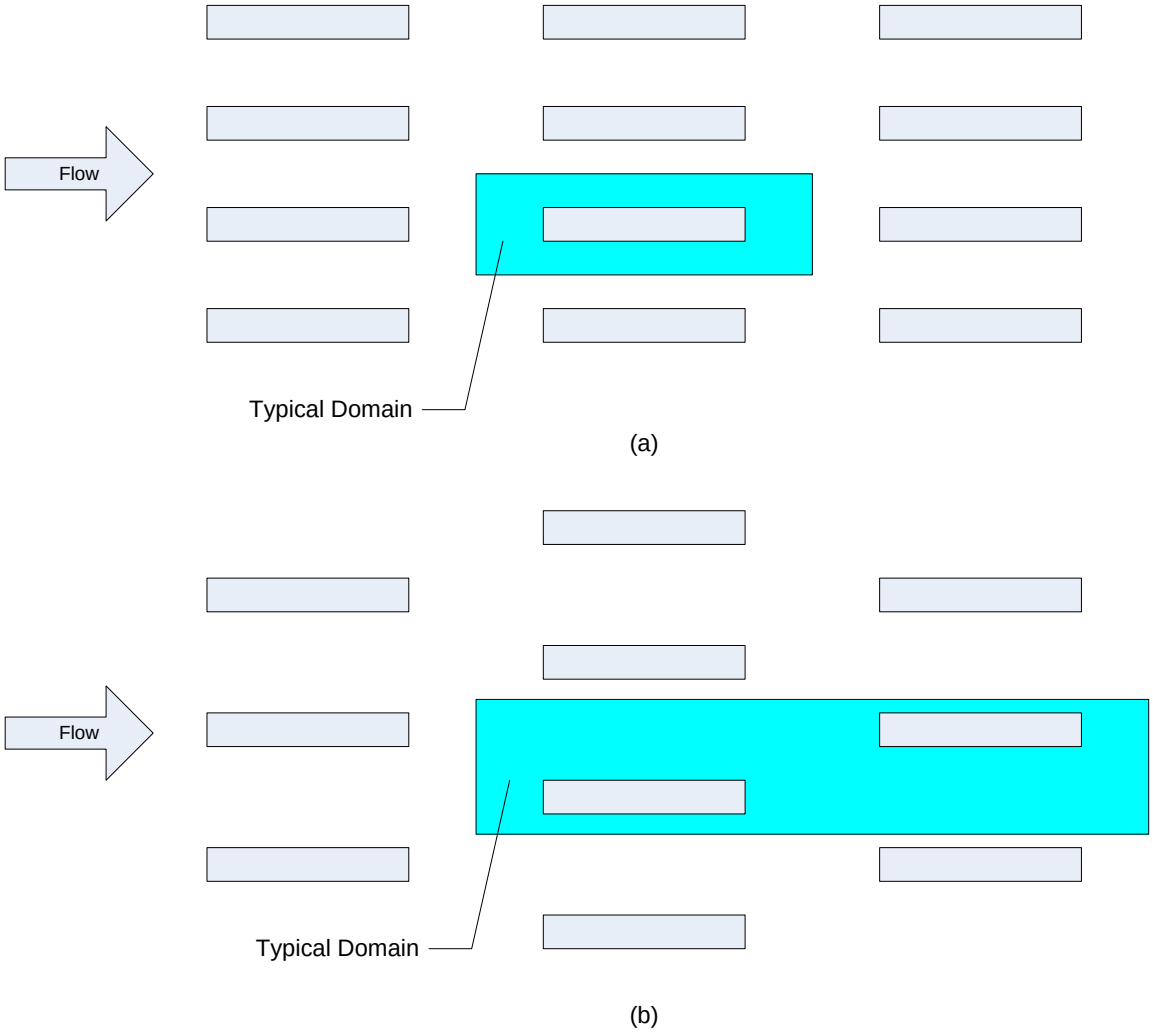

Figure 2-3. Rectangular tube arrays: (a) inline; (b) staggered.

unsteadiness in the wake makes form drag increase. Therefore, steady simulation under-predicts form drag and over-predicts skin friction.

In Zhang *et al.* [15] and Zhang *et al.* [16], the authors considered the effect of 3D features in the flow on the predicted heat transfer and friction for the geometry shown in Figure 2-3. The distinction was made between intrinsic 3D effects, which occur for 2D

geometry at higher Reynolds numbers, and extrinsic 3D effects which occur for all Reynolds numbers. They showed that for higher Reynolds numbers, 2D simulations tend to over-predict Nusselt number and under-predict friction. In other words, 3D effects tend to decrease predicted heat transfer rates based on 2D predictions. 3D effects on friction depend on *Re*. For lower *Re*, just above the onset of 3D, skin drag dominates so the increase in skin drag leads to an overall increase in friction. For higher *Re* where form drag is higher relative to skin drag, the decrease in form drag leads to an overall decrease in friction and pumping power.

Balachandar and Parker [17] studied inline and staggered arrays of rectangular cylinders as shown in Figure 2-3 in addition to isolated cylinders to observe the effect of the array on the onset of oscillatory behavior. The important effect of the periodic array is to promote vortex shedding at lower Reynolds numbers than for isolated cylinders. For the inline case, the stream-wise periodic spacing was shown to have a weak effect on the onset of vortex shedding while the transverse spacing had a large influence.

2.3 Summary

The material above explains the origin of self-sustained oscillatory flow for the grooved channel and communicating channel geometry. The close match between TS frequencies for the plane channel and the oscillation frequencies of the grooved channel and communicating channel problem help explain the origin of these oscillations. These geometries may be viewed as plane channels with periodic geometric interruptions. As such, the main flow is that of a channel flow. The presence of the periodic interruptions destabilizes some modes that appear as stable modes in plane channel flow as evidenced

by the fact that the resulting frequencies closely match those predicted for plane channel flow.

The material on arrays of rectangular tubes focuses more on the effects of SSOF on heat transfer and friction than on the origin of the SSOF itself. The current work also focuses on the effects of SSOF rather than on the origins. The geometry of the flat tube arrays considered in the current work was based on the geometry of arrays of rectangular tubes which was known to produce self-sustained oscillations with the expectation that small changes in geometry will still leave a geometry for which SSOFs will exist. Tube spacing and flow conditions were varied to establish Re_{crit} and document *Nu* and friction factor and break down friction into skin friction and form drag. The Reynolds number was limited to a maximum value of approximately 2000 to stay well within the boundaries of where the 2D simulation is valid. This maximum value is based on the results in Zhang *et al.* [14] in which flow unsteadiness was observed for the staggered configuration of rectangular tubes for a Reynolds number of 1465. Converting the Reynolds number value to match the definition in the current work, this translates to a value of approximately 2344. This value of Re=2344 was further reduced to Re_{max}= 2000 based on differences in geometry and the fact that observations of chaotic behavior would tend to invalidate the results. A module of periodicity $m=1$ was used.

3. NUMERICAL METHODS

3.1 Overview

The current work involves the application of numerical methods to investigate the performance characteristics of flat tube heat exchanger devices operating in flow regimes exhibiting self-sustained oscillations. As established in the previous section, the current work will include determining values for the primary quantities of interest including friction factor, Strouhal number and Nusselt number for a series of 2D geometric domains under varying constant-property flow conditions. To determine values for derived quantities such as these, a numerical solution provides values of stream-wise velocity (u), cross-stream velocity (v), pressure (P), and temperature (T) at discrete locations in the domain of interest at suitable intervals of time. Once the u, v, P, and T fields have been determined, values for the derived quantities of interest may be calculated.

For the current work, a computer code was developed based on the principles of a particular Control Volume Finite Element Method (CVFEM) for 2D, steady, constant-property flows. This code was then modified to allow for unsteady solutions using a particular semi-implicit Runge-Kutta method. For the cases of interest, Double Cyclic flow conditions were imposed as stated above.

This section includes a discussion of the general transport equation, spatial discretization using CVFEM, temporal discretization using an ESDIRK (**E**xplicit first stage, **S**ingle diagonal coefficient, **D**iagonally **I**mplicit, **R**unge-**K**utta) method, and solution subject to Double Cyclic conditions. Also included here is a discussion of how

the various derived quantities of interest are calculated using numerical methods. As no originality is claimed for any of these pieces of the numerical method, only material essential to an overall understanding of the methods used is included here. The originality in the current work lies in the combination of these methods in one computer code. The interested reader will find additional details for specific topics in the appendices provided as noted.

3.2 General Transport Equation

Many numerical methods for solving flow and heat transfer problems are based on the general transport equation for the transported scalar ϕ as shown in Eq.(3.1) below.

$$\frac{\partial(\rho\phi)}{\partial t} + \overline{\nabla}\bullet(\rho\bar{v}\phi) = \overline{\nabla}\bullet(\Gamma\overline{\nabla}\phi) + S \qquad \text{Eq.(3.1)}$$

In Eq.(3.1), ρ is the fluid density, Γ is the diffusivity, S is a generalized source term, and $\bar{v}$ is the velocity vector while ϕ may represent either stream-wise velocity (u), cross-stream velocity (v), or temperature (T). It should be noted that pressure (P) is not a transported scalar and may not be represented by ϕ in Eq.(3.1).

In Eq.(3.1), the term $\frac{\partial(\rho\phi)}{\partial t}$ represents the time rate of change of ϕ in a fluid element, the term $\overline{\nabla}\bullet(\rho\bar{v}\phi)$ represents the change of ϕ in a fluid element due to advection, the term $\overline{\nabla}\bullet(\Gamma\overline{\nabla}\phi)$ represents the change of ϕ in a fluid element due to diffusion, and the term S the change of ϕ in a fluid element due to sources. Depending on the choice of ϕ, Γ, and source term S, Eq.(3.1) may represent conservation of x-

momentum, of *y*-momentum, of energy, or of mass for a differential fluid element. Table 3-1 shows the definition of Γ and *S* for the various quantities that ϕ may represent for 2D flows.

Table 3-1. Definitions of ϕ, Γ, and *S* for the general transport equation

Conserved Quantity	ϕ	Γ	*S*
Mass	1	0	0
X-Momentum	u	μ	$-\partial P / \partial x$
Y-Momentum	v	μ	$-\partial P / \partial y$
Energy	T	k / c_p	Q

Many numerical methods, including the CVFEM chosen for the current work, are based on an integral form of Eq.(3.1). By integrating each term of Eq.(3.1) with respect to the volume of a control volume (CV), and by applying Gauss Divergence Theorem to the advective and diffusive terms, Eq.(3.2) below is obtained.

$$\int_{CV} \frac{\partial(\rho\phi)}{\partial t} dV + \int_{s} \left(\rho \bar{v}\phi\right) \bullet \hat{n}\, ds = \int_{s} \left(\Gamma \bar{\nabla}\phi\right) \bullet \hat{n}\, ds + \int_{CV} S\, dV \qquad \text{Eq.(3.2)}$$

In Eq.(3.2), *s* represents the surface of the CV and $\hat{n}$ represents the outward surface normal of the CV. Further simplification results from defining a combined flux vector $\bar{J}$ representing the combination of advective and diffusive flux as shown by Eq.(3.3) and Eq.(3.4) below.

$$\bar{J} \equiv \rho \bar{v}\phi - \Gamma \bar{\nabla}\phi \qquad \text{Eq.(3.3)}$$

$$\int_{CV} \frac{\partial(\rho\phi)}{\partial t} dV + \int_{s} \bar{J} \bullet \hat{n}\, ds = \int_{CV} S\, dV \qquad \text{Eq.(3.4)}$$

Eq.(3.4) is the basis for the overall numerical method chosen. Spatial discretization is required for the flux integral and source integral while temporal discretization is required for the unsteady term. Various methods (and their combinations) exist for discretization of Eq.(3.4). What follows is a discussion of discretization and solution methods used in the current work.

3.3 Control Volume Finite Element Method (CVFEM)

3.3.1 Overview

In general, CVFEMs are methods of spatial discretization that combine features of both Finite Element (FE) methods and Finite Volume (FV) methods. Like FE methods, the domain is discretized into regions called *elements* to which material properties are assigned and within which interpolation functions are defined which describe the variation of velocity, pressure, and temperature within an element. Like FV methods, *control volumes* (CVs) are defined to which conservation equations in integral form are applied resulting in sets of algebraic equations for the domain which may be solved for the u, v, P, and T fields.

There are several 2D CVFEM's described in the literature. References are available that describe various formulations for 2D CVFEM's using both triangular- and quadrilateral-shaped elements. Comparing and contrasting the various versions is beyond the scope of the current work. The basic method for the particular CVFEM employed in the current work is the co-located, equal-order, triangular-element method

described by Prakash [18] [19]. Additional material directly influencing the current work may be found in Sabaas [20] [21] [22] and Husain [23].

This section on CVFEM will describe Prakash's CVFEM for steady, 2D, laminar, constant-property flows.

3.3.2 Element Velocity and the General Transport Equation

Prakash's CVFEM is referred to above as a co-located and equal order method. This refers to the fact that values for *u*- and *v*-velocity, pressure, and temperature are obtained at the same discrete locations in the domain of interest. Co-located methods may produce physically unrealistic solutions, particularly in the pressure field. This is generally referred to as *checkerboarding* and staggered grid methods (as opposed to co-located methods) were developed to prevent this effect. For the co-located CVFEM used in the current work, the concept of *mass-conserving* or *element velocity* is introduced to prevent checkerboarding effects. While the concept of element velocity cannot be fully defined at this point in the discussion, it is important to introduce it at this point. A detailed definition of element velocity may be found in Section 3.3.8 below.

For now, the following statements regarding the element velocity will be made:

1) The element velocity vector ($\overline{\tilde{v}}$) replaces the nodal velocity vector ($\overline{v}$) in the definition of the combined flux vector, Eq.(3.3) above, regardless of the choice of ϕ;
2) The components of the element velocity are known numerically at a given element's nodes;

3) The numerical values of the element velocity components vary linearly with position within the element.

With these statements in mind, Eq.(3.3) may be rewritten by substituting the element velocity vector for the nodal velocity vector.

$$\overline{J}^{EV} = \rho\overline{\overline{v}}\phi - \Gamma\overline{\nabla}\phi \qquad \text{Eq.(3.5)}$$

The superscript EV signifies that the flux is calculated using the element velocity rather than the nodal velocity.

As stated above, the discussion to follow considers spatial discretization using CVFEM for steady flows only. Therefore, the unsteady term in Eq.(3.4) plays no part in the discussion. Eq.(3.4) may now be rewritten by dropping the unsteady term and by substituting the flux vector based on element velocity for the flux vector based on nodal velocity.

$$\int_s \overline{J}^{EV} \bullet \hat{n} ds = \int_{CV} S dV \qquad \text{Eq.(3.6)}$$

Eq.(3.6) is the general transport equation upon which Prakash's CVFEM is based. Eq.(3.6) is in steady-flow form assuming that sources, if they exist, are not time-dependent. The unsteady term in Eq.(3.4) will be considered in Section 3.4 for the discussion of temporal discretization.

3.3.3 Domain Discretization

For Prakash's 2D CVFEM, the computational domain is first discretized as a set of triangular elements which completely fill the domain without overlap. The vertices of these triangles are called *nodes* and are the locations at which *u*, *v*, *P*, and *T* are

calculated. Each element is divided into three equal-area sub-regions by defining links from the element centroid to the midpoint of each of the three sides as shown in Figure 3-1(a). Each sub-region is associated with one of the element's three nodes. The fact that the domain is meshed with triangles makes this method a good candidate for the solution of flat tube heat exchanger problems in that the irregular domain geometry associated with the tube shape may be meshed to desired accuracy using triangles. Also, the variables *u*, *v*, *P*, and *T* may remain in their native (*x*, *y*) coordinates without coordinate transformation.

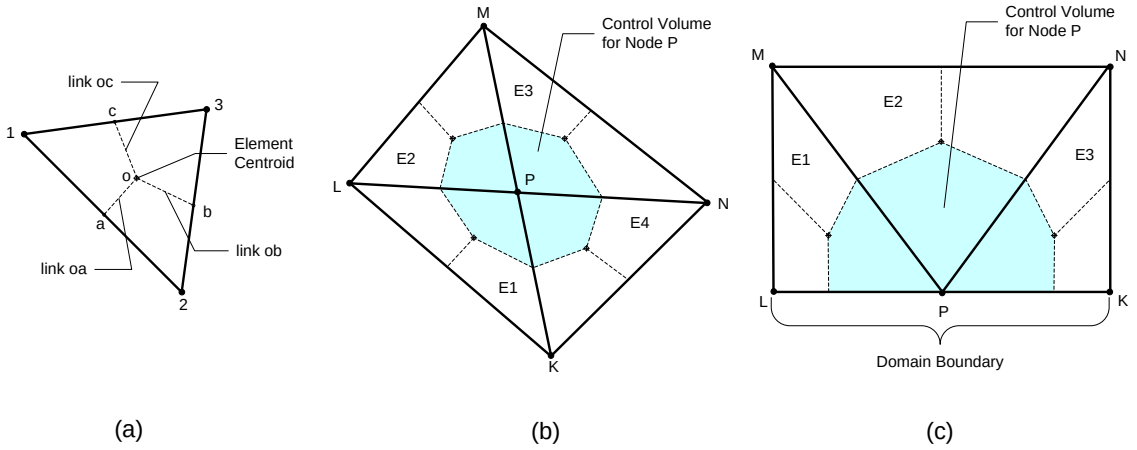

Figure 3-1. CVFEM domain discretization: (a) typical element; (b) internal CV; (c) boundary CV.

The domain is further discretized as a set of polygonal CVs such that each node in the domain has an associated CV. The set of CVs defined in this manner completely fills the domain without overlap. The CV associated with a given node is formed from sub-regions of the elements that share that particular node. The element links of

contributing elements form the boundary of the CV for internal CVs as shown in Figure 3-1(b). For boundary CVs, the boundary is formed from a combination of element links and segments of the domain boundary as shown in Figure 3-1(c). Integral forms of the various conservation equations as given by Eq.(3.6) are applied to the CVs resulting in four sets of algebraic equations, one set for each of the unknown field variables of interest: *u*, *v*, *P*, and *T*. If the general variable χ represents *u*, *v*, *P*, or *T* then the various conservation equations for the CV associated with Node P may be written in the following form:

$$a_P \chi_P + \sum_{nb} a_{nb} \chi_{nb} = b_P \qquad \text{Eq.(3.7)}$$

The set of all such equations for all CVs in the domain are solved simultaneously using an iterative solution technique based on the SIMPLER algorithm [24].

3.3.4 Flux Integration for $\phi = u, v, or T$

Applying integral forms of the conservation equations to a given CV involves, in part, determining expressions for the integrated flux of *x*-momentum, *y*-momentum, energy, and mass across the element links that form the CV boundary as shown by the LHS of Eq.(3.6) above. Boundary CVs are special cases involving integrated flux across segments of the domain boundary itself. The integration along the boundary of a particular CV is performed piece-wise by first calculating the integrated flux across each element link for the entire set of elements and then assembling the appropriate expressions for the set of links that form the boundary of a particular CV. Adjustments

to account for flux through domain boundary segments may be added after the assembly process.

To perform the integrated flux calculations across an element link, expressions for *u*- and *v*-velocity, temperature, and the spatial gradients of pressure are required at points along the link. Once these expressions are known, Simpson's One-Third Rule may be applied to derive an expression for the integrated flux. Interpolation functions are defined to provide the distribution of velocity, pressure, and temperature within each element. For the general transported scalar variable ϕ representing stream-wise velocity (*u*), cross-stream velocity (*v*), or temperature (*T*) (but not pressure (*P*)), the interpolation function takes the following exponential form:

$$\phi(X,Y) = AZ(X) + BY + C$$

$$\text{where} \quad Z(X) = \frac{\Gamma}{\rho \tilde{U}_{avg}} \left\{ \exp\left[Pe \frac{(X - X_{\max})}{(X_{\max} - X_{\min})} \right] - 1 \right\}$$

$$Pe = \frac{\rho \tilde{U}_{avg} (X_{\max} - X_{\min})}{\Gamma} \qquad \text{Eq.(3.8)}$$

$$X_{\max} = \max(X_1, X_2, X_3)$$

$$X_{\min} = \min(X_1, X_2, X_3)$$

In Eq.(3.8), ρ and Γ are the density and diffusion coefficient of the fluid, respectively. *Pe* is the element Peclet number. $\tilde{U}_{avg}$ is the average magnitude of the element velocity vector for the element's three nodes. The interpolation function is defined in an element-local coordinate system *(X, Y)* such that the *X*-axis is aligned with the average flow direction within the element, the *Y*-axis direction is determined by the right-hand rule, and the origin is located at the element centroid. The interpolation function is exponential along the *X* direction and linear along the *Y* direction. In this way, the

method takes into account the local flow direction within the element during flux calculations, thus minimizing false diffusion. X_{max} and X_{min} are the maximum and minimum, respectively, of the *X* coordinate values at the element's three nodes as specified in the element-local coordinate system.

The coefficients *A*, *B*, and *C* in Eq.(3.8) do not represent numerical constants. Rather, they are expressions in terms of the unknown values of ϕ at the element's three nodes. The expressions for *A*, *B*, and *C* are determined by assuming that Eq.(3.8) is valid at each of the element's three nodes. (See Appendix B.) Eq.(3.8) therefore provides an expression for ϕ at a point *(X, Y)* within the element in terms of the unknown values of ϕ at the element's nodes. If one uses Simpson's One-Third Rule for the integration of flux along a link, the expressions for ϕ at the two endpoints and at the midpoint of each link may be used to determine the final expression for the integrated flux of ϕ across the link in terms of the unknown values of ϕ at the element's three nodes. The integrated flux across an element link (Φ_{link}) may be represented as follows:

$$\Phi_{link} = \lambda_i \phi_i \quad i = 1,2,3 \qquad \text{Eq.(3.9)}$$

where ϕ_i represents the unknown value of ϕ at node i and λ_i represents a numerical coefficient. The expressions for λ_i may be found in Appendix C.

After the expressions for integrated flux in the form of Eq.(3.9) are obtained for all element links in the domain, an assembly process is used to combine the expressions for all links forming the boundary of a given CV. The result is an expression of the form

$$Integrated\ \ Flux = a_P \phi_P + \sum_{nb} a_{nb} \phi_{nb} \qquad \text{Eq.(3.10)}$$

representing integrated flux for the x- or y-momentum equation or for conservation of energy equation for that particular CV. Details of the assembly process may be found in Appendix D.

3.3.5 Integration of Source Term

The RHS of Eq.(3.6) is an integral over the area of the CV. (In 2D, the "volume" of the control volume is actually an area.) The area of each CV is composed of sub-regions of contributing elements. The area of each sub-region is one-third the area of the contributing element by definition and the source *S* is defined to be constant over the area of the element. The average *S* over the CV may be defined as an area-weighted average of *S* over the set of contributing elements for the CV.

$$\overline{S}_{CV} = \frac{\sum_{nbe} \left[S^{nbe} \frac{A^{nbe}}{3} \right]}{AREA_{CV}} \qquad \text{Eq.(3.11)}$$

In Eq.(3.11), the superscript *nbe* signifies neighboring element. Using Eq.(3.11) to evaluate the integral on the RHS of Eq.(3.6), Eq.(3.12) below is obtained.

$$\int_{CV} S dV = \int_{CV} \overline{S}_{CV} dV = \left[\frac{\sum_{nbe} \left[S^{nbe} \frac{A^{nbe}}{3} \right]}{AREA_{CV}} \right] AREA_{CV} = \sum_{nbe} \left[S^{nbe} \frac{A^{nbe}}{3} \right] \qquad \text{Eq.(3.12)}$$

Thus, the source integral has been converted to a summation of quantities over the set of contributing elements. For the current work, the source integration will

evaluate to a numerical constant b_P. Thus, after flux integration and source term integration, Eq.(3.6) is converted to an algebraic equation of the form of Eq.(3.13) below.

$$a_P\phi_P + \sum_{nb} a_{nb}\phi_{nb} = b_P \qquad \text{Eq.(3.13)}$$

Eq.(3.13) may represent either conservation of *x*-momentum, of *y*-momentum, or of energy depending on the choice of ϕ.

3.3.6 Momentum Equations

When solving the *x*- or *y*-momentum equations, either $\phi = u$ or $\phi = v$. For either choice, $\Gamma = \mu$, the fluid viscosity. Because the diffusion coefficient is the same for either choice of $\phi = u$ or $\phi = v$, the flux coefficients will be identical for the *x*- and *y*-momentum equations and will be denoted a^{uv}. The source integrals will, in general, be different.

For the current work, the source integrals for the momentum equations will involve only the spatial derivatives of pressure as shown in Table 3-1 above. In this method, $\partial P/\partial x$ and $\partial P/\partial y$ are considered constants for elements although they may change values during the solution process. Writing the momentum equation in the form of Eq.(3.13) using the notation discussed the following expressions for conservation of *x*- and *y*-momentum for a CV associated with Node P are obtained.

$$a_P^{uv}u_P + \sum_{nb} a_{nb}^{uv}u_{nb} = \sum_{nbe}\left[\frac{-\partial P}{\partial x}\frac{A^{nbe}}{3}\right] \qquad \text{x-momentum} \qquad \text{Eq.(3.14)}$$

$$a_P^{uv} u_P + \sum_{nb} a_{nb}^{uv} u_{nb} = \sum_{nbe} \left[\frac{-\partial P}{\partial y} \frac{A^{nbe}}{3} \right] \qquad \text{y-momentum} \qquad \text{Eq.(3.15)}$$

3.3.7 Energy Equation

When solving the energy equation, $\phi = T$ and $\Gamma = k/c_p$. For the current work, volumetric energy sources are not considered and the source integral from Eq.(3.12) is identically zero. However, the application of known heat flux to the domain boundary may result in a constant on the RHS of the equation denoted as c_P. The flux coefficients are denoted by a^e. Writing the energy equation in the form of Eq.(3.13) using the notation discussed the following expression for conservation of energy for a CV associated with Node P is obtained.

$$a_P^e T_P + \sum_{nb} a_{nb}^e T_{nb} = c_P \qquad \text{energy} \qquad \text{Eq.(3.16)}$$

3.3.8 Definition of Element Velocity

This section will present the definition of the element velocity used previously in the derivation of the momentum and energy equations. It is necessary to define this prior to discussing the method of solving for nodal pressures.

Beginning with the *x*-momentum equation Eq.(3.14) above, the RHS of Eq.(3.14) may be rewritten in terms of the average pressure gradient over the CV.

$$a_P^{uv} u_P + \sum_{nb} a_{nb}^{uv} u_{nb} = AREA_{CV} \left. \frac{\overline{\partial P}}{\partial x} \right|_{CV} \qquad \text{Eq.(3.17)}$$

Solving Eq.(3.17) for the nodal velocity u_P results in Eq.(3.18) below.

$$u_P = \frac{-\sum_{nb} a_{nb}^{uv} u_{nb}}{a_P^{uv}} + \frac{AREA_{CV} \left.\overline{\frac{\partial P}{\partial x}}\right|_{CV}}{a_P^{uv}} \qquad \text{Eq.(3.18)}$$

For convenience, $\hat{u}_P$ and d_P^u are defined as follows

$$\hat{u}_P = \frac{-\sum_{nb} a_{nb}^{uv} u_{nb}}{a_P^{uv}} \qquad d_P^u = \frac{AREA_{CV}}{a_P^{uv}} \qquad \text{Eq.(3.19)}$$

such that the nodal velocity may be written as

$$u_P = \hat{u}_P + d_P^u \left[\left.\overline{\frac{\partial P}{\partial x}}\right|_{CV} \right] \qquad \text{Eq.(3.20)}$$

Eq.(3.20) represents the *nodal* velocity at Node P. The *x*-component of the *element* velocity ($\tilde{u}_P$) is now defined by replacing the CV's average pressure gradient with the pressure gradient for Element E that contains Node P.

$$\tilde{u}_P = \hat{u}_P + d_P^u \left[\left.\frac{\partial P}{\partial x}\right|_{E} \right] \qquad \text{Eq.(3.21)}$$

While $\hat{u}_P$ and d_P^u have unique values at nodes in the domain, $\tilde{u}_P$ is valid only for calculations performed within Element E.

By similar logic, the expression for the y-component of the element velocity ($\tilde{v}_P$) may be developed as Eq.(3.22) below.

$$\tilde{v}_P = \hat{v}_P + d_P^v \left[\left.\frac{\partial P}{\partial y}\right|_{E} \right] \qquad \text{Eq.(3.22)}$$

Eq.(3.21) and Eq.(3.22) represent the *x*- and *y*-components of the element velocity, respectively. Note that each is written in terms of the pressure gradient within a particular element.

3.3.9 Solution for Nodal Pressure

Pressure is not a transported scalar. Therefore the method described above for solution for ϕ is not directly applicable to the solution for nodal pressures in the domain of interest. Pressure *P* does not appear explicitly in the set of conservation equations for CVs. For the incompressible flows of interest in the current work, there is no equation of state to evaluate *P*.

The conservation of mass version of Eq.(3.6) together with the previously defined element velocity components and a linear interpolation function for pressure within an element will be used to write algebraic equations that have nodal pressures as explicit unknowns.

By choosing $\phi = 1$ in Eq.(3.6), the conservation of mass equation is obtained in the form of Eq.(3.23) below.

$$\int_s \rho(\bar{\tilde{v}} \bullet \hat{n}) ds = 0 \qquad \text{Eq.(3.23)}$$

Recall that $\bar{\tilde{v}}$ represents the element velocity vector, the components of which are represented by Eq.(3.21) and Eq.(3.22) above. From these equations, it may be seen that the components of the element velocity vector involve the spatial gradients of pressure within elements.

A linear interpolation function of the form of Eq.(3.24) below is used for pressure within an element.

$$P = Ax + By + C \qquad \text{Eq.(3.24)}$$

The spatial derivatives of pressure within the element are therefore as follows

$$\begin{aligned} \frac{\partial P}{\partial x} &= A = A_1 P_1 + A_2 P_2 + A_3 P_3 \\ \frac{\partial P}{\partial y} &= A = B_1 P_1 + B_2 P_2 + B_3 P_3 \end{aligned} \qquad \text{Eq.(3.25)}$$

The details of this derivation may be found in Appendix E.

The combination of using a linear interpolation function for pressure within an element, the definition of element velocity, and the use of element velocity in the expression for mass flux in Eq.(3.23) allow the mass flux to be written in terms of nodal pressures rather than in terms of the spatial derivatives of nodal pressures. This allows equations to be constructed for the solution of the unknown nodal pressures.

Once again, the flux integrations are performed on an element basis and the resulting expressions assembled for a CV. The result is an equation of the form

$$a_P P_P + \sum_{nb} a_{nb} P_{nb} = d_P \qquad \text{Eq.(3.26)}$$

representing conservation of mass for a CV in terms of the unknown nodal pressure values at Node P and at each of the neighbor nodes.

3.3.10 Boundary Conditions and Solution Process

Typical boundary conditions for steady flow problems are specified *u*- and *v*-velocity at the domain inlet, and zero *u*- and *v*-velocity at solid boundaries. For heat

transfer problems, either temperature *(T)* or heat flux ($q"$) is specified along specified boundaries. For boundary CVs, the integrated flux of a variable across the domain boundary is added to the expression in the form of Eq.(3.13) or Eq.(3.26). The boundary conditions are known numerically, so this process modifies the general source term b_P or d_p in these equations.

As stated earlier, conservation equations are assembled for each CV for each field variable of interest (*u*, *v*, *P*, and *T*). The resulting sets of equations are solved iteratively using a combination of the line-by-line procedure and the Tri-Diagonal Matrix Algorithm (TDMA). The order of solution is determined by the SIMPLER algorithm.

3.4 ESDIRK

The section above on CVFEM covered spatial discretization for steady flows. This section will cover the temporal discretization necessary for solving unsteady problems such as the oscillating flows of interest in the current work.

The method used for the current work is a semi-implicit Runge-Kutta method known as an ESDIRK (**E**xplicit first stage, **S**ingle diagonal coefficient, **D**iagonally **I**mplicit, **R**unge-**K**utta) method. This method was used by Ijaz [25] in developing his SIMPLE DIRK method for solving unsteady combined flow and heat transfer problems. SIMPLE DIRK combines the spatial discretization methods of SIMPLE [24] with the temporal discretization methods of ESDIRK to create a method capable of arbitrarily high order of accuracy.

In the current work, the spatial discretization methods of CVFEM are combined with the temporal discretization methods of ESDIRK to solve the unsteady problems of interest. More specifically, a two-stage second-order ESDIRK is used. The ESDIRK is well documented in the literature and a full mathematical development of the method is beyond the scope of the current work. In this section, a simple geometric interpretation of the two-stage second-order ESDIRK is presented and it is shown that the results from the CVFEM spatial discretization may be incorporated into the unsteady equation.

In general, the unsteady equation of interest is of the form shown in Eq.(3.27) below.

$$\frac{\partial \phi}{\partial t} = g(t, \phi) \qquad \text{Eq.(3.27)}$$

A solution for ϕ at some time ($t+1$) is required given that a solution at time (t) is known. The function $g(\phi, t)$ may be interpreted as the slope of the ϕ versus t curve. The mean value theorem of calculus guarantees that for some average value of the slope ($\overline{g}$) between time (t) and time ($t+1$), that the value of ϕ at time ($t+1$) can be represented by Eq.(3.28) below.

$$\phi^{t+1} = \phi^{t} + \Delta t \, \overline{g} \qquad \text{Eq.(3.28)}$$

The key is in estimating $\overline{g}$. When working forward in time, the value of g at time (t) is known, but the value of g at time ($t+1$) is not known.

For the two-stage second-order ESDIRK used in the current work, the average slope is estimated by the arithmetic mean of the slopes at the beginning and at the end of the time step. Thus, the solution for ϕ^{t+1} is given by the following equation.

$$\phi^{t+1} = \phi^t + \Delta t\left[\frac{1}{2}\left(g^{t+1} + g^t\right)\right] \qquad \text{Eq.(3.29)}$$

The ESDIRK uses the known solution at time t to calculate the slope g^t explicitly. Therefore, in Eq.(3.29), ϕ^t and g^t are known numerically. The unknown slope at time (*t+1*) may be written as an expression including the unknown values of ϕ thus exposing them for solution. This process may be demonstrated by applying Eq.(3.29) to the general transport equation in integral form.

Eq.(3.30) below is obtained by rearranging Eq.(3.4) from above, using the flux vector based on the element velocity as given by Eq.(3.5), and including the unsteady term that was ignored for CVFEM development above.

$$\int_{CV} \frac{\partial(\rho\phi)}{\partial t}\, dV = -\int_s \overline{J}^{EV} \bullet \hat{n}\, ds + \int_{CV} S\, dV \qquad \text{Eq.(3.30)}$$

For constant fluid properties, the unsteady term may be integrated with respect to volume to produce Eq.(3.31) below.

$$\rho V \frac{\partial \phi}{\partial t} = -\int_s \overline{J}^{EV} \bullet \hat{n}\, ds + \int_{CV} S\, dV \qquad \text{Eq.(3.31)}$$

The RHS of Eq.(3.31) may be recognized as a rearrangement of Eq.(3.6) above. The spatial discretization techniques associated with CVFEM described above led to an equivalent expression in terms of unknown nodal ϕ values and coefficients a_p*'s* and b_p*'s* as seen in Eq.(3.13). Substituting a rearranged Eq.(3.13) into Eq.(3.31) and dividing both sides by ρV , obtain Eq.(3.32) below is obtained.

$$\frac{\partial \phi_p}{\partial t} = \frac{1}{\rho V}\left\{-\left[a_p\phi_p + \sum_{nb} a_{nb}\phi_{nb}\right] + b_p\right\} = g(\phi, t) \qquad \text{Eq.(3.32)}$$

Eq.(3.32) represents the slope of the $\phi(t)$ curve.

The slope at time (t) may be evaluated explicitly as a number based on the stored solution at the beginning of the time step. Rewriting Eq.(3.29) by substituting Eq.(3.32) for g^t Eq.(3.33) is obtained.

$$\phi_p^{t+1} = \phi_p^t + \Delta t \frac{1}{2} g_p^t + \Delta t \frac{1}{2}\frac{1}{\rho V}\left\{-\left[a_p^{t+1}\phi_p^{t+1} + \sum_{nb} a_{nb}^{t+1}\phi_{nb}^{t+1}\right] + b_p^{t+1}\right\} \qquad \text{Eq.(3.33)}$$

Multiplying through by $\dfrac{\rho V}{\Delta t \dfrac{1}{2}}$ and moving the unknowns to the LHS results in Eq.(3.34) below.

$$\phi_p^{t+1}\left[\frac{\rho V}{\Delta t \frac{1}{2}} + a_p^{t+1}\right] + \sum_{nb} a_{nb}^{t+1}\phi_{nb}^{t+1} = \left[\frac{\rho V}{\Delta t \frac{1}{2}}\right]\left[\phi_p^t + \Delta t \frac{1}{2} g_p^t\right] + b_p^t \qquad \text{Eq.(3.34)}$$

This is the same as the steady flow equation with only two differences. The coefficient of ϕ_p^{t+1} is modified as is the source term on the RHS of the equation.

The solution procedure is the same as developed for steady solutions using CVFEM. Solution procedure at time (t) is as follows.

1) At the end of the previous time step, calculate and store g_p. This becomes g_p^t for current time step.

2) Use steady solution routines to determine coefficients a_p and b_p.

3) Modify a_p per Eq.(3.34).

4) Modify the source term per Eq.(3.34).

5) Solve using the same solver routines as for steady solution.

6) After convergence, calculate and store g_p for the next time step.

3.5 Periodically Fully-Developed Flow and Double Cyclic Conditions

Double Cyclic (DC) conditions are a special case of Periodically Fully-Developed (PFD) flow conditions. This section begins with a discussion of PFD conditions followed by a discussion of DC conditions.

3.5.1 Periodically Fully Developed (PFD) Flow

Commonly, heat exchanger devices such as the ones of interest in the current work exhibit regular geometric spacing of tubes or fins in the stream-wise direction leading to the development of PFD flow conditions at some distance from the inlet. Once developed, the PFD conditions persist until near the device exit. For such devices, the majority of tubes or fins lie in flow modules exhibiting PFD conditions. Therefore, the performance of such a device may be characterized by the flow and heat transfer characteristics in a single PFD module. That the desired performance data may be obtained from solution of a single PFD module means faster solution times and better utilization of available computer resources.

Mathematical formulation of PFD flow and heat transfer is well established and may be found in Patankar *et al.* [26] and Kim and Anand [27]. In this section, a brief discussion of PFD conditions is presented followed by a discussion of how these

conditions are implemented in the CVFEM code. In the discussion to follow, x represents the stream-wise direction, y represents the cross-stream direction, and L represents the length of the module.

In a periodically fully-developed flow domain, velocity profiles in the stream-wise direction repeat themselves periodically and pressure drop per module length (β) remains constant.

$$\begin{aligned} u(x,y) &= u(x+L,y) = u(x+2L,y)\cdots \\ v(x,y) &= v(x+L,y) = v(x+2L,y)\cdots \\ \beta &\equiv \frac{P(x,y)-P(x+L,y)}{L} = \text{constant} \end{aligned} \qquad \text{Eq.(3.35)}$$

Pressure in a PFD module may be represented as a combination of global pressure drop per module and local pressure variation $\hat{P}$.

$$P(x,y) = -\beta x + \hat{P}(x,y) \qquad \text{Eq.(3.36)}$$

While pressure itself does not repeat with periodicity, the local pressure variation does.

$$\hat{P}(x,y) = \hat{P}(x+L,y) = \hat{P}(x+2L,y)\cdots \qquad \text{Eq.(3.37)}$$

In the CVFEM representation of the *x*- and *y*-momentum equations, the spatial derivatives of pressure are included in the source term of the general transport equation Eq.(3.1). By taking the spatial derivatives of pressure using Eq.(3.36), the following expressions for the source terms in the conservation of *x*- and *y*-momentum equations are obtained:

$$\begin{aligned} &\text{X-Momentum Source} \\ &-\frac{\partial P}{\partial x} = \beta - \frac{\partial \hat{P}}{\partial x} \end{aligned} \qquad \text{Eq.(3.38)}$$

Y-Momentum Source

$$-\frac{\partial P}{\partial y} = -\frac{\partial \hat{P}}{\partial y} \qquad \text{Eq.(3.39)}$$

Both the *x*-momentum and *y*-momentum equations are therefore written in terms of the spatial derivatives of the locally-varying pressure component $\hat{P}$. The spatial derivatives of pressure (*P)* do not appear explicitly in the equations. The *x*-momentum equation includes a β term representing the global pressure gradient in the stream-wise direction for the module.

For the case of specified wall heat flux, the temperature values do not repeat module-to-module for neighboring PFD modules. Rather, the temperature differences repeat from module to module and a global temperature gradient γ in the stream-wise direction may be defined for a PFD module of length (*L*) by performing a global energy balance on a PFD module.

$$\Big[T(x+L,y) - T(x,y)\Big] = \Big[T(x+2L,y) - T(x+L,y)\Big] \cdots$$
$$\gamma \equiv \frac{T(x+L,y) - T(x,y)}{L} = \frac{Q}{\dot{m} c_p L} \qquad \text{Eq.(3.40)}$$

In Eq.(3.40) *Q* is the total heat into (or out of) the module, $\dot{m}$ is the mass flow rate through the module, and c_p is the fluid specific heat.

The temperature at any point *(x, y)* in the domain may be expressed in terms of a global component involving γ and a locally varying component $\hat{T}$ as shown below.

$$T(x,y) = \gamma x + \hat{T}(x,y) \qquad \text{Eq.(3.41)}$$

The locally varying component $\hat{T}$ is periodic in the stream-wise direction.

$$\hat{T}(x,y) = \hat{T}(x+L,y) = \hat{T}(x+2L,y)\cdots \qquad \text{Eq.(3.42)}$$

Substituting for *T(x, y)* in terms of the global temperature rise and local variation components into the conservation of energy equation for 2D, steady, laminar flows, a form involving γ and $\hat{T}$ is obtained. Two new source terms, each involving γ are revealed.

$$\text{Energy Equation Source Terms}$$
$$S_1^E = -\rho c_p \gamma u \qquad \text{Eq.(3.43)}$$
$$S_2^E = \frac{\partial}{\partial x}\left(k\gamma\right)$$

The term $-\rho c_p \gamma u$ is an added source term involving the global temperature gradient for the PFD module. The second added source term $\frac{\partial}{\partial x}\left(k\gamma\right)$ is identically zero if the thermal conductivity (*k*) is constant throughout the domain. This second source term is important for domains including conducting solids such that the thermal conductivity for the solid differs from the thermal conductivity for the fluid. (Kim and Anand [27]). For the current work, the second source term may be ignored.

Thus, for a PFD solution, one does not solve for pressure (*P*) or temperature (*T*), but rather for the locally-varying components $\hat{P}$ and $\hat{T}$. Table 3-2 below shows the changes in ϕ and source terms.

Table 3-2. Definitions of ϕ, Γ, and S for PFD flow conditions

Conserved Quantity	ϕ	Γ	S
Mass	1	0	0
X-Momentum	u	μ	$\beta - \partial\hat{P} / \partial x$
Y-Momentum	v	μ	$-\partial\hat{P} / \partial y$
Energy	$\hat{T}$	k / c_p	$-\rho c_p \gamma u + \frac{\partial}{\partial x}\left(k\gamma\right)$

3.5.2 Double Cyclic Conditions

Double Cyclic conditions occur in a heat exchanger device like that shown in Figure 2-3. There is a recurring geometric spacing of tubes in both the stream-wise and cross-stream direction. A typical domain is shown in Figure 2-3. From the figure, it is clear that the velocities along the top boundary of the domain must be the same as for the bottom boundary of the domain. The pressures and temperatures are also identical along the transverse boundaries. However, in the stream-wise direction, PFD conditions exist as described above.

Many times, for cases like these, symmetry is applied at the transverse boundaries. Symmetric conditions are a special case of Double Cyclic conditions. In a domain with repeating geometric features in both stream-wise and cross-stream directions, the boundaries of the module considered for solution are arbitrary as long as the module repeats. So, for example one may choose a transverse line that is a line of symmetry and symmetric conditions may be applied. Double Cyclic conditions are more general in that the choice of transverse boundary need not lie along a line of symmetry.

A CVFEM code to implement the above conditions was developed. Rather than solving for *u*, *v*, *P*, and *T*, the DC version of the code provides the solution for *u*, *v*, $\hat{P}$, and $\hat{T}$ for a single DC module. The DC code is based on an existing code which implements the standard CVFEM algorithms described above. The required code modifications include the addition of the source terms for the momentum and energy equations as explained above in reference to PFD conditions and the implementation of repeating conditions on the transverse boundaries. The Cyclic Tri-Diagonal Matrix Algorithm (CTDMA) is used in the iterative solver when operating on either rows of nodes aligned in the stream-wise direction or on columns of nodes aligned in the cross-stream direction.

Solution for a DC module involves first specifying a value of β and solving the flow problem for *u*, *v*, and $\hat{P}$. Next, the flow solution is used to calculate $\dot{m}$ for the domain and the specified heat flux is used to calculate *Q*. Eq.(3.40) may then be used to calculate γ. The solution process concludes with the solution for the $\hat{T}$ field. Note that for the PFD solution, β is specified rather than velocity. Because of this, Reynolds numbers cannot be explicitly specified.

3.6 Parameter Definitions

3.6.1 Reynolds Number

The Reynolds number is calculated using the average *u*-velocity at the inlet of the module as shown by Eq.(3.44) below.

$$Re = \frac{\rho D_h \bar{u}_{inlet}}{\mu} \qquad \text{Eq.(3.44)}$$

In Eq.(3.44), module hydraulic diameter (D_h) is taken as twice the module height (H). Also, ρ and μ represent the fluid density and viscosity, respectively.

3.6.2 Friction Factor for PFD/DC Solution

The current work involves calculating friction factor and Nusselt number for the flow and temperature fields associated with the cases of interest. However, with the DC code, the solution does not actually involve pressure or temperature. Rather, the solution is in terms of the locally varying components $\hat{P}$ and $\hat{T}$ subject to a specified value of β. Therefore, friction factor and Nusselt number must be defined in terms of β and $\hat{T}$.

The friction factor (f) may be defined as follows:

$$f \equiv \frac{\beta(D_h/2)}{\rho \bar{u}_{inlet}^2} \qquad \text{Eq.(3.45)}$$

The friction factor definition in Eq.(3.45) is used for compatibility with Zhang *et al.* [14]. In this equation, β is the specified global pressure drop and D_h is the hydraulic diameter.

3.6.3 Bulk Temperature and Nusselt Number for PFD/DC Solution

Calculating the Nusselt number requires calculating the bulk temperature at cross-stream sections of the domain. Because these flows may exhibit recirculation, the definition of bulk temperature is modified to include the absolute value of velocity rather

than simply the velocity itself. For the case of DC flow with specified surface heat flux, the solution process yields the $\hat{T}$ field rather than the *(T)* field. Therefore, the fluctuating component of the bulk temperature $\hat{T}_b$ is defined in terms of $\hat{T}$ rather than in terms of (*T*).

$$\hat{T}_b(x) \equiv \frac{\int_y \hat{T}(x,y)\left|u(x,y)\right| dy}{\int_y \left|u(x,y)\right| dy} \qquad \text{Eq.(3.46)}$$

The Nusselt number is defined as follows:

$$Nu(x) \equiv \frac{q'' D_h}{\left[\hat{T}_s(x) - \hat{T}_b(x)\right] k} \qquad \text{Eq.(3.47)}$$

In Eq.(3.47), *k* is the fluid conductivity. It can be shown that *Nu* defined in Eq.(3.47) in terms of fluctuating temperatures $\hat{T}_s$ and $\hat{T}_b$ is directly comparable to the standard definition in terms of actual temperatures T_s and T_b.

3.6.4 Strouhal Number

The Strouhal number representing non-dimensional frequency of oscillation was defined in the current work to be compatible with Zhang *et al.* [14]. This was used for oscillations of *u*- and *v*-velocity at points of interest in the domain. Given the *u* versus time or *v* versus time data, the period of oscillation was found by computing the time between peaks. The frequency of oscillation was computed as the reciprocal of the period. The Strouhal number (*Str*) was then calculated using Eq.(3.48) below.

$$Str = \frac{(freq) D_{\min}}{\bar{u}_{inlet}} \qquad \text{Eq.(3.48)}$$

Here, $D_{\min}$ is the minor diameter of the flat tube.

3.6.5 Non-Dimensional Pumping Power

In this work, one of the measures of cost of operation for the heat exchanger devices of interest is pumping power. Amon and Mikic [10] used a dimensionless pumping power (Φ) defined as follows.

$$\Phi = \frac{3}{4}\left\langle \frac{dp}{dx} \right\rangle \frac{Vh^4}{\rho \nu^3} \qquad \text{Eq.(3.49)}$$

This same expression appears as non-dimensional viscous dissipation in Karniakis *et al.* [28]. In Eq.(3.49), $\left\langle \frac{dp}{dx} \right\rangle$ is equivalent to the global pressure gradient β in the current work. Also, V is equivalent to $\bar{u}_{inlet}$ and h is equivalent to the domain height H.

Amon and Mikic [10] used the definition of Φ above to compare cases of varying flow conditions for fixed domain geometry. For the current work, however, there are nine combinations of domain length and height. A definition for non-dimensional pumping power that takes into account the varying geometry is required. The new definition is obtained by starting with an expression for the dimensional pumping power. Pumping power was defined as the product of the required pressure drop to sustain the flow, the average flow velocity at the inlet, and the cross-sectional area of the domain.

$$\text{Pumping Power} = \Delta P \bar{u}_{inlet} A_{cs} \qquad \text{Eq.(3.50)}$$

For these Double Cyclic domains, $\Delta P = \beta L$ and $A_{cs} = HW$ where W is the width of the domain which is taken as 1 for 2D. Therefore, the dimensional pumping power may be written as follows.

$$\text{Pumping Power} = \beta \overline{u}_{inlet} LH \qquad \text{Eq.(3.51)}$$

This may be rewritten in terms of the friction factor (f) from Eq.(3.45) above.

$$\text{Pumping Power} = f \rho \overline{u}_{inlet}^3 L \qquad \text{Eq.(3.52)}$$

This may then be non-dimensionalized using fluid properties and the tube minor diameter $D_{\min}$.

$$\psi = \frac{f \overline{u}_{inlet}^2 L D_{\min}}{\nu^3} \qquad \text{Eq.(3.53)}$$

Eq.(3.53) represents the non-dimensional pumping power for the cases of interest. Even with varying L and H, plots of this non-dimensional quantity retain the trends shown with the dimensional quantity. This was not true of the definition used by Amon an Mikic [10].

3.6.6 Tube Drag Coefficients

Skin friction and pressure drag were calculated for each tube for each time step of solution. The values of each were then time-averaged and presented in the form of non-dimensional coefficients.

The non-dimensional skin friction coefficient ($C_{D,skin}$) was based on the time-averaged skin friction (τ_w), the average inlet velocity (u_{inlet}^2), and the tube minor diameter ($D_{\min}$) as shown in Eq.(3.54) below.

$$C_{D,skin} \equiv \frac{\overline{\tau}_w \big/ D_{\min}}{\rho u_{inlet}^2} \qquad \text{Eq.(3.54)}$$

The non-dimensional pressure drag coefficient ($C_{D,press}$) was based on the time-averaged pressure drag ($drag_{press}$), the average inlet velocity (u_{inlet}^2), and the tube minor diameter ($D_{\min}$) as shown in Eq.(3.55) below.

$$C_{D,press} \equiv \frac{drag_{press} \big/ D_{\min}}{\rho u_{inlet}^2} \qquad \text{Eq.(3.55)}$$

Both $C_{D,skin}$ and $C_{D,press}$ are presented in the data tables in Section 5. It should be noted that while there are two tube surfaces present in each DC domain used for analysis, that the above coefficients are based on the skin friction and pressure drag of one tube only. The time-average values are identical for each of the two tubes.

4. CODE VALIDATION*

The first version of the computer code was developed to solve steady, developing flow problems. Next, versions of the steady code were developed which implemented periodically fully-developed (PFD) flow conditions and Double Cyclic (DC) flow conditions. Finally, unsteady versions of developing flow, PFD, and DC codes were developed. At each step in development, the code was tested against published or theoretical results. For this section, selected validation results involving Poiseiulle flow and tubes in cross-flow are presented as these topics relate directly to the current work. Also in this section is a discussion of previously published work involving use of the steady versions of the code.

4.1 Steady Validation

Many validation runs were performed with the steady code during development. Classic validation problems such as the driven cavity and backward facing step were used. In each case, the code produced results that compared well with published results or theory.

As part of the work for the publication of Fullerton and Anand [5], a problem involving tubes in cross-flow between parallel flat plates was solved and the results compared to previously published results for the same domain geometry and flow conditions. Figure 4-1 shows the domain which consists of five regularly spaced round

---

*Part of this section is reprinted with permission from "Periodically Fully-Developed Flow and Heat Transfer over Flat and Oval Tubes Using a Control Volume Finite-Element Method" by T.L. Fullerton and N.K. Anand, 2010. *Numerical Heat Transfer, Part A*, vol. 57, pp. 642-665, Copyright 2010 by Taylor & Francis Group, LLC.

tubes confined between parallel plates. There is also an entry and exit region. Periodically fully-developed conditions were not imposed for this validation effort. Rather, a developing flow version of the code was used. The results, however, indicate that PFD conditions develop downstream from the entry region due to the regularly spaced flow interruptions. Table 4-1 shows a comparison of average Nusselt numbers using the CVFEM code compared to computed results from Kundu *et al*. [29] and Bahaidarah *et al*. [4]. These results demonstrate good agreement.

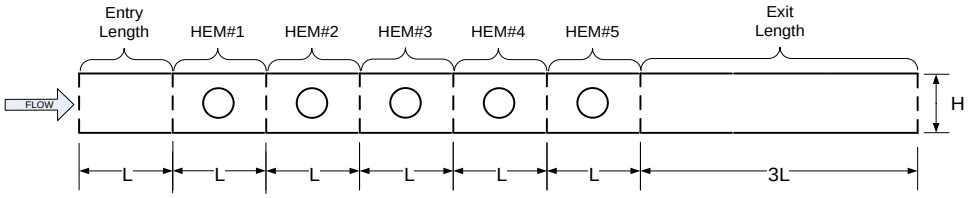

Figure 4-1. Computational domain for steady, developing-flow code validation.

Table 4-1. Comparison of average Nusselt numbers

	HEM#2	HEM#3	HEM#4
Re 50			
Kundu *et al*. [29]	9.4	9.4	9.8
Bahaidarah *et al.* [4]	9.23	9.23	9.23
Fullerton&Anand [5]	9.24	9.24	9.24
Re 200			
Kundu *et al*. [29]	12.5	12.6	12.8
Bahaidarah *et al.* [4]	12.44	12.43	12.42
Fullerton&Anand [5]	12.50	12.46	12.45

A steady PFD version of the code was developed for use in collecting data for the publication of [5] and [30]. As part of the validation effort for [5], the PFD code was used to solve 2D Poiseiulle flow for the case of constant specified wall heat flux for

several meshes of increasing density. As the mesh density increased, the Nusselt number approached the theoretical value of $140/17 \approx 2.235$. The finest mesh used produced a Nusselt number of 2.234 along both the top and bottom walls which is within 0.04% of the theoretical value.

As part of the work for [30], results were obtained for Poiseiulle flow with specified constant wall temperature. The subject of [30] was the development of a new method whereby the constant wall temperature problem could be solved using PFD flow conditions without solving the eigenvalue problem for temperature. For this problem, the flow is characterized by the product of friction factor and Reynolds number *(fRe)* which should converge to a value of 96. The heat transfer is characterized by a Nusselt number value of 7.54. Table 4-2 shows the flow results for several Reynolds number values. In each case, the quantity (*fRe*/96) is a value of 1.000 to three decimal places. Table 4-2 also shows Nusselt number values that are 7.54 to two decimal places. Both the flow and heat transfer results indicate good agreement with theoretical values for the steady PFD code.

Table 4-2. Flow results for parallel plate example

Nominal *Re*	Calculated Re	*f*	*(fRe)/96*	*Nu*
100	99.896	0.961	1.000	7.543
150	150.132	0.640	1.000	7.542
200	199.791	0.481	1.000	7.542
250	250.028	0.384	1.000	7.542
300	299.975	0.320	1.000	7.542

4.2 Unsteady Validation

The first validation effort with the unsteady code was to replicate the driven cavity results from Ijaz [25] . The CVFEM results and the results of Ijaz closely matched.

An attempt was made using the unsteady CVFEM code to recreate the results presented by Zhang *et al.* [14] for the staggered configuration of rectangular tubes. For this exercise, no attempt at establishing grid independence was made. Rather, a mesh was built for use with the CVFEM code with the same number of nodes as the mesh used in the Zhang *et al.* [14] study. Figure 4-2(a) and Figure 4-2(b) below show friction factor versus Reynolds number and *j-factor* versus Reynolds number, respectively, for both the Zhang results and for the current work. The *j-factor* is a measure of heat transfer defined by the following equation.

$$j \equiv \frac{\overline{\langle Nu \rangle}}{RePr^{0.4}} \qquad \text{Eq.(4.1)}$$

In Eq.(4.1), $\overline{\langle Nu \rangle}$ is the time-averaged Nusselt number, *Re* is the time-averaged Reynolds number, and *Pr* is the Prandtl number. The exponent of 0.4 is for fully developed flow.

Figure 4-2(a) and Figure 4-2(b) represent good agreement between the two sets of data. Good agreement was also obtained with the integrated values of skin friction and pressure drag on the tube between the two sets of results, as well as the Strouhal numbers. One difference in the results was that the Zhang *et al.* [14] data shows an increase of Strouhal number from 0.15 to 0.16 to 0.17 with increasing Reynolds number

for the range of Reynolds numbers tested. Results with the CVFEM code showed a smaller increase in Strouhal number from 0.153 to 0.164 over the same range of Reynolds numbers tested. This difference between the two sets of results may be due to the coarseness of the mesh used for the CVFEM solutions. As indicated above, no attempt was made to establish grid independence for this exercise. As will be seen below in the discussion of the results of the current work, there is a variation of Strouhal number with Reynolds number for many of the cases considered.

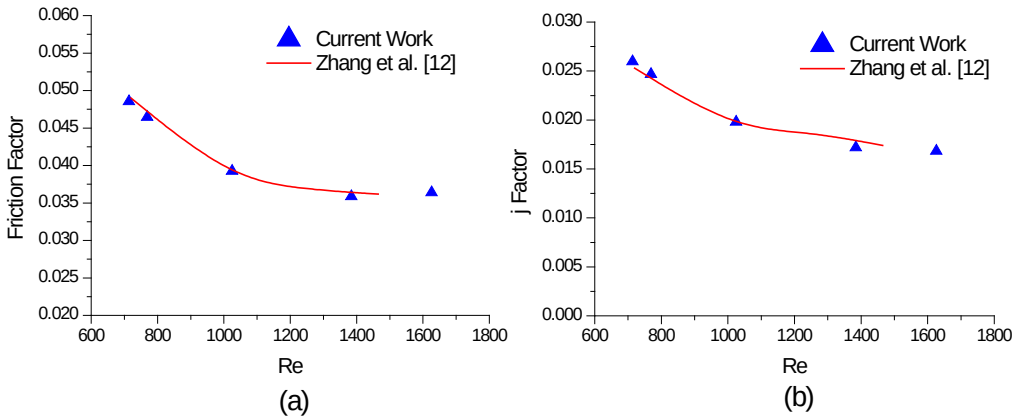

Figure 4-2. Comparison of current work to Zhang *et al.* [14] for rectangular tubes: (a) friction factor versus Reynolds number; (b) j factor versus Reynolds number.

4.3 Previously Published Work

4.3.1 Fullerton and Anand [5]

A journal article entitled “Periodically Fully-Developed Flow and Heat Transfer Over Flat and Oval Tubes Using A Control Volume Finite-Element Method” was published in *Numerical Heat Transfer,* Part A in 2010. [5] This article appears in its entirety in Appendix A of this document. What follows is a description of the work performed and a brief summary of relevant results.

For this work, the steady version of the CVFEM code was used along with imposed PFD conditions for a numerical study of the performance of flat and oval tubes as compared to the performance of round tubes in a heat exchanger device. Each two-dimensional domain consisted of a single tube confined between two insulated parallel plates. Figure 4-3 shows the geometry of the computational domains studied. Once the diameter of the round tube was selected, the shapes of the flat and oval tubes were selected such that the perimeter of all tubes would be equal. This also ensured that the heat transfer area was the same for each domain given that constant heat flux was specified on the surface of each tube.

For each of the computational domains shown in Figure 4-3, steady, laminar, 2D, constant-property solutions were obtained for Reynolds number range of 50-350 for two different fluids of Prandtl number 0.7 and 7.0.

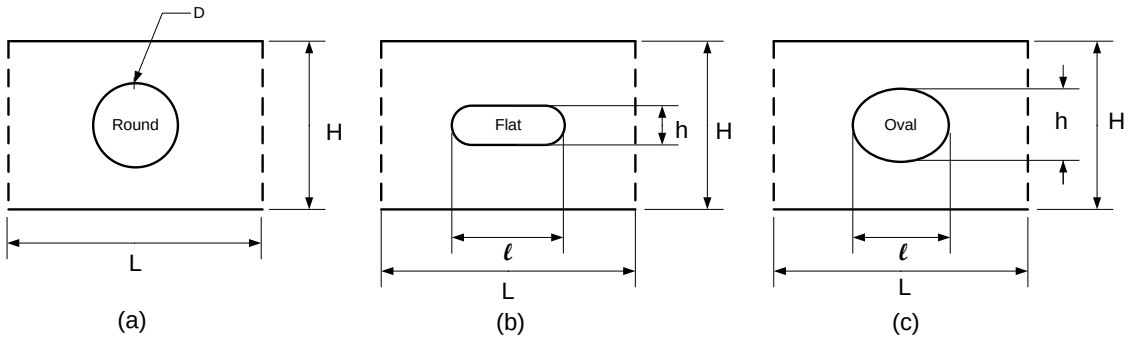

Figure 4-3. Computational domain geometries for Fullerton and Anand [5]:
(a) round tube; (b) flat tube; (c) oval tube.

In comparing the performance of flat and oval tubes to that of round tubes under similar conditions, two parameters were used. The heat transfer enhancement ratio (Nu^+) was used for comparison on the basis of heat transfer performance alone.

$$Nu^+ \equiv \frac{Nu_{avg,noncircular}}{Nu_{avg,round}} \qquad \text{Eq.(4.2)}$$

In Eq.(4.2), Nu_{avg} represents the average *Nu* along the perimeter of the top half of any of the three tube shapes for matching Reynolds numbers.

The second performance parameter, the heat transfer performance ratio (Nu^*) takes into account not only the heat transfer performance, but the required pumping power to maintain the flow.

$$Nu^* \equiv \frac{Nu^+}{\left[f_{flat \text{ or } oval} / f_{round} \right]^{1/3}} \qquad \text{Eq.(4.3)}$$

In Eq.(4.3), Nu^+ is the heat transfer enhancement ratio from above, and f is the friction factor. The denominator is proportional to the required pumping power for a flat or oval tube domain to that required of a round tube domain at the same Reynolds number.

Figure 4-4 and Figure 4-5 show plots of Nu^+ and Nu^* for Prandtl number 0.7 and 7.0. These plots show that for all cases considered, the heat transfer enhancement ratio is less than one meaning that the round tube outperforms both the flat and the oval tube on the basis of heat transfer only. However, the heat transfer performance ratio is greater than one for all cases considered meaning that if both heat transfer and required pumping power are considered, then both the flat and oval tubes outperform the round tube.

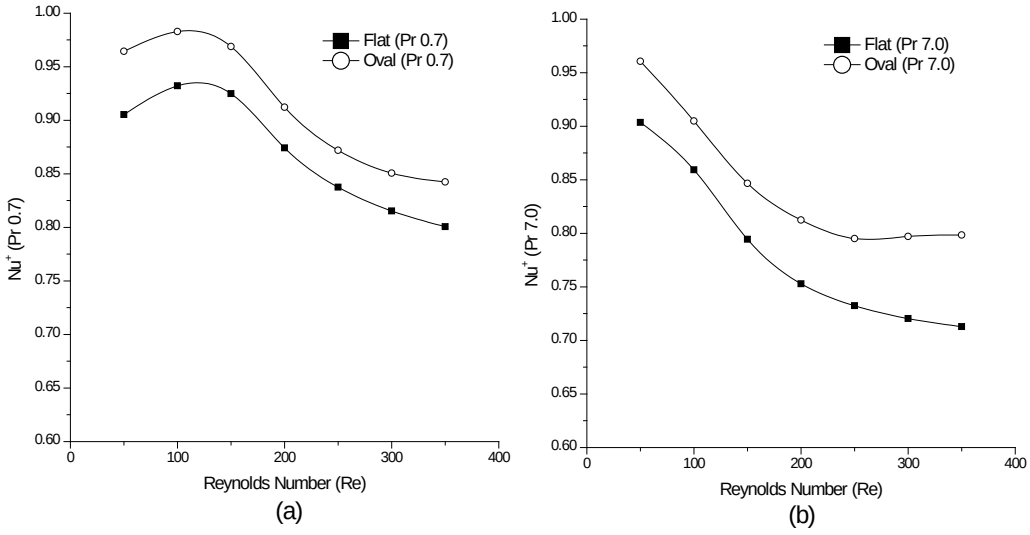

Figure 4-4. Heat transfer enhancement ratio versus Reynolds number for Fullerton and Anand [5]: (a) Pr=0.7; (b) Pr=7.0.

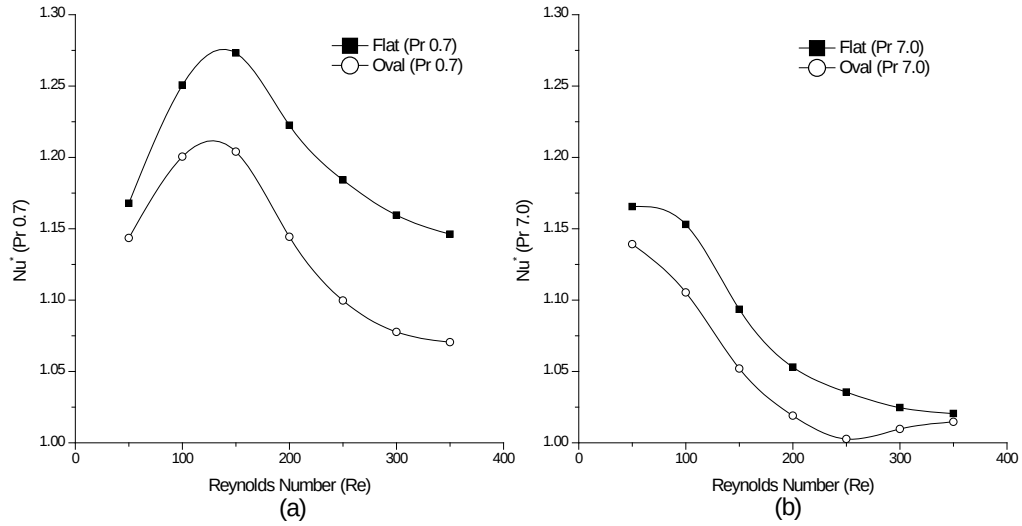

Figure 4-5. Heat transfer performance ratio versus Reynolds number for Fullerton and Anand [5]: (a) Pr=0.7; (b) Pr=7.0.

4.3.2 Fullerton and Anand [30]

A journal article entitled "An alternative approach to study periodically fully-developed flow and heat transfer problems subject to isothermal heating conditions" was published in *International Journal of Engineering Science* in 2010. [30] The subject of this paper is a method of solving the PFD heat transfer problem with constant specified wall temperature without solving an eigenvalue problem. [26]

Periodically fully-developed flow conditions are fully described in Patankar *et al.* [26]. Section 3.5.1 in this document gives a summary of PFD conditions including a discussion of the periodic condition for the heat transfer problem when constant wall heat flux is specified. For that case, the temperature may be expressed in terms of a

global component involving γ and a locally varying component $\hat{T}$ as seen in Eq.(3.41). Solution may then proceed using standard methods except solving for $\hat{T}$ instead of *T*.

For the case of specified wall temperature, however, the PFD solution for temperature involves the solution of an eigenvalue problem involving both the unknown temperature at each node in the domain and the unknown bulk temperature at each stream-wise location in the domain. Keeping in mind that PFD conditions arise from having a series of equally-spaced geometric features in the stream-wise direction, many researchers have chosen to not use PFD conditions to solve the problem. Instead, they use a developing flow (DF) code with a domain consisting of several identical modules connected inlet-to-outlet. PFD conditions are not imposed for solution, but periodicity may be recognized by monitoring the values of flow parameters and heat transfer parameters in the modules. A DF solution of a multi-module domain produces the same result as a PFD solution, but with the penalty of solving a much larger domain.

In Fullerton and Anand [30], the authors present an alternative approach to solving the case of specified wall temperature under PFD conditions. The method may be viewed as a hybrid approach between the two methods described above. This alternative method involves first obtaining a PFD solution for the flow field in a single-module domain. The temperature solution is then obtained with a DF code by first importing the PFD flow solution into each module of a multi-module DF domain. Thus, the flow field in the DF code is represented by the exact PFD solution and need not be solved using the DF code. The temperature solution may then be obtained in the usual

way and a PFD temperature module may be identified from the resulting solution. This process is shown diagrammatically in Figure 4-6.

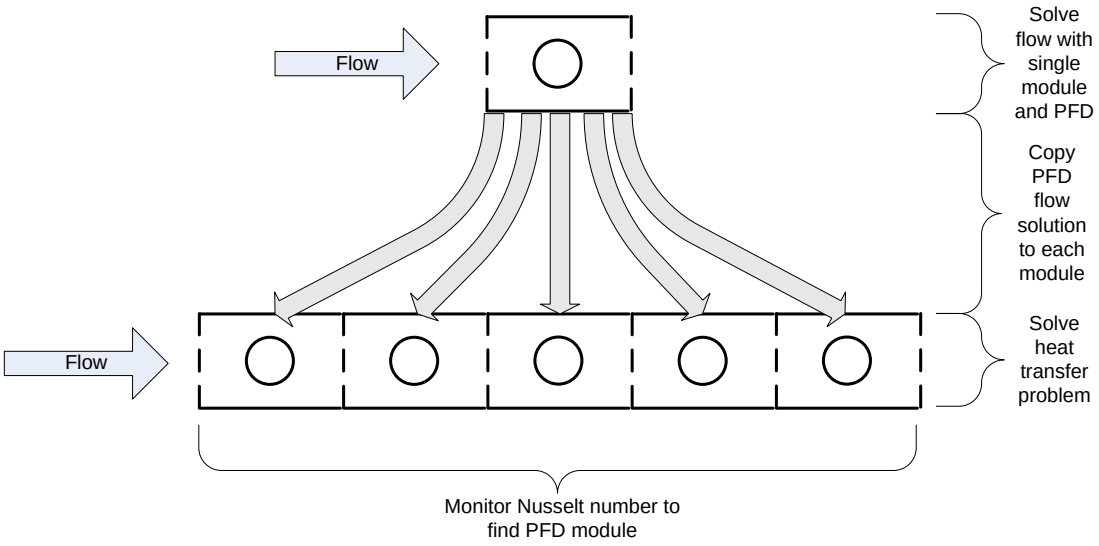

Figure 4-6. Diagram describing the alternative method.

Both of the solution methods discussed above should produce valid results. Setting up the specified wall temperature problem as an eigenvector problem has the advantage of requiring only a single-module domain. It does, however, involve extra code for the solution. It should be noted that the authors (Fullerton and Anand) have not attempted this type of solution. The DF solution approach has the advantage of not imposing PFD conditions, but, assuming that one is interested only in the performance in a PFD module, the solution must be obtained for a domain that is much larger than the actual domain of interest. This is of particular disadvantage in that the flow field must

be solved for such a large domain. For both approaches, solution of the flow field is much more time consuming than solution of the temperature field.

The alternative approach obviates the need to address the eigenvalue problem at the expense of having to produce the flow and temperature solutions in separate processes. Compared to a regular DF solution, the alternative approach eliminates the need to solve the flow problem for multi-module domains when one is generally only interested in the solution at a PFD module.

The alternative approach to solving the PFD specified wall temperature problems was tested using two CVFEM codes: one for the PFD flow problem, and one for the DF temperature problem. It should be noted that while testing used CVFEM codes, the method is not dependent on using CVFEM. It may be used with other finite difference or finite volume methods to solve combined flow and heat transfer problems.

One problem for which the alternative approach was tested was flow in a parallel plate channel with staggered plate fins. The domain of interest is shown in Figure 4-7. Several researchers have studied this problem using a variety of analysis techniques. Kelkar *et al*. [31] used a control volume technique as presented in Patankar [24]. Kelkar *et al*. [31] not only imposed PFD conditions for both the flow problem and the heat transfer problem, they also took advantage of the inverted symmetry in the domain to recast the PFD conditions for solution of only one-half of the PFD module. Santos and de Lemos [32] studied the problem for both solid and porous baffles using a control volume technique and the SIMPLE algorithm. Webb and Ramadhyani [33] studied conjugate heat transfer for different fin heights using a control volume technique and the

SIMPLER algorithm. Nonino and Comini [34] studied the problem in the context of several spatially periodic domains of varying geometry using a finite element technique. Cheng and Huang [35] studied the problem for various fin configurations for the case of the two plates at different constant temperatures.

Figure 4-8 shows a comparison of friction factor versus Reynolds number from the various sources and from the current work using the CVFEM. Figure 4-8 shows the spread of data among the various sources. The results in the current work show good agreement for Re up to approximately 200, but show that $(f\,Re)/96$ increases at a higher rate with increasing Reynolds number at Re>200 as compared to the other methods. Since the $(f\,Re)/96$ values closely match at lower Reynolds numbers, it may be assumed that the flow solutions are comparable. At higher Reynolds numbers, the fact that the $(f\,Re)/96$ values do not match indicates that the current method does not match the flow solutions of the other methods.

Figure 4-9 shows a comparison of $\overline{Nu}$ versus Re from various sources and from the current work. $\overline{Nu}$ is a module average Nusselt number. At the lower Re values, the values of $\overline{Nu}$ compare well. However, for the current work, the $\overline{Nu}$ values increase at a faster rate with increasing Re. This is due to differences in the flow solution at these Re values. At lower Re, where the friction factor matches well, the corresponding $\overline{Nu}$ also matches.

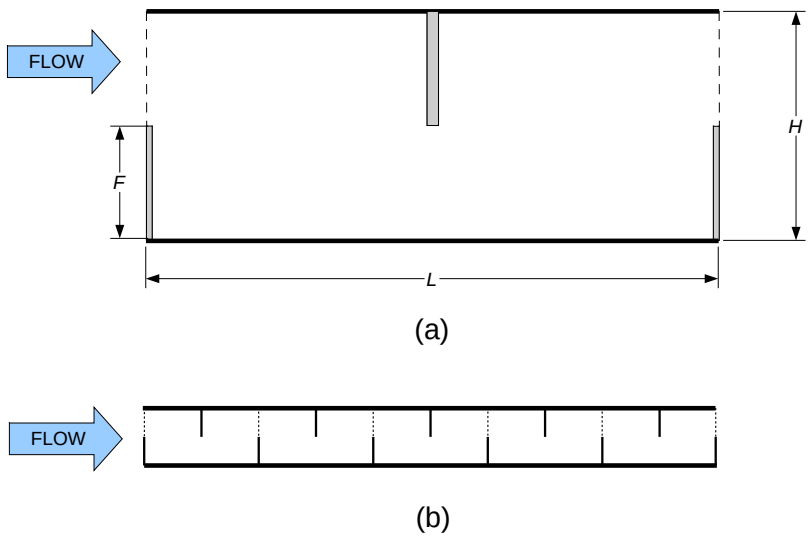

Figure 4-7. Staggered plate domains for Fullerton and Anand [30]: (a) PFD flow domain; (b) DF temperature domain.

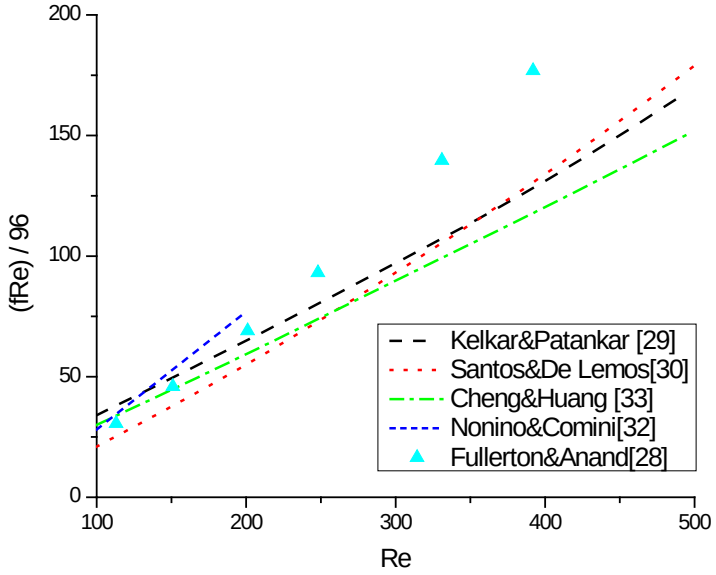

Figure 4-8. Plot of (*fRe*)/96 from various sources [30].

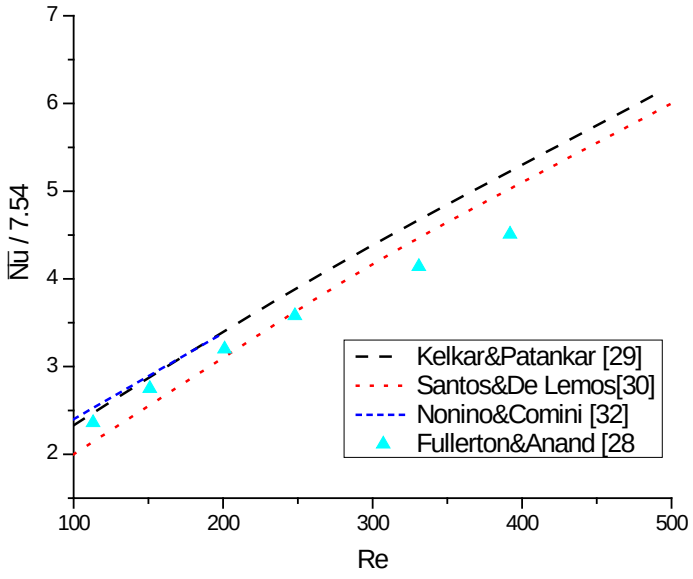

Figure 4-9. Plot of *Nu*/7.54 versus *Re* from various sources [30].

5. RESULTS AND DISCUSSION

As stated in previous sections, the primary interest of the current work is the flow and heat transfer performance of staggered arrays of flat tubes operating in flow regimes exhibiting laminar, self-sustained oscillations. In this section, the geometry of the domains of interest and the CVFEM meshes for those domains are described. Results of grid and time step independence are presented followed by a description of procedures involved in the solution process for both the unsteady and steady solutions obtained. Results are presented in both tabular and graphical form describing characteristics of flow and heat transfer for the cases considered.

5.1 Domain Geometry

Figure 5-1 shows an array of flat tubes in a staggered configuration. As discussed above, there is no interest in entrance or exit effects in the current work, so the analysis domain may be limited to the shaded region shown and DC conditions may be imposed. The choice of domain is not unique, but the domain chosen must include the surfaces of two tubes. The domain shown was chosen for convenience in that the transverse boundaries lie along lines of symmetry. Checking that *y*-velocities along a stream-wise line of symmetry approach zero value is useful as a check for the code.

Figure 5-1 shows the parameters defining the shape of the flat tube. The overall length of the tube is D_{maj} and the height is D_{min}. The shape of the flat tube is such that the end curves are full-radius curves. The tube aspect ratio (AR) is defined as the ratio of major diameter to minor diameter as shown below.

$$AR = D_{maj} / D_{\min} \qquad \text{Eq.(4.4)}$$

For the current work, the tube ratio *AR* was maintained at a constant value of *AR*=6.0 for all domains considered.

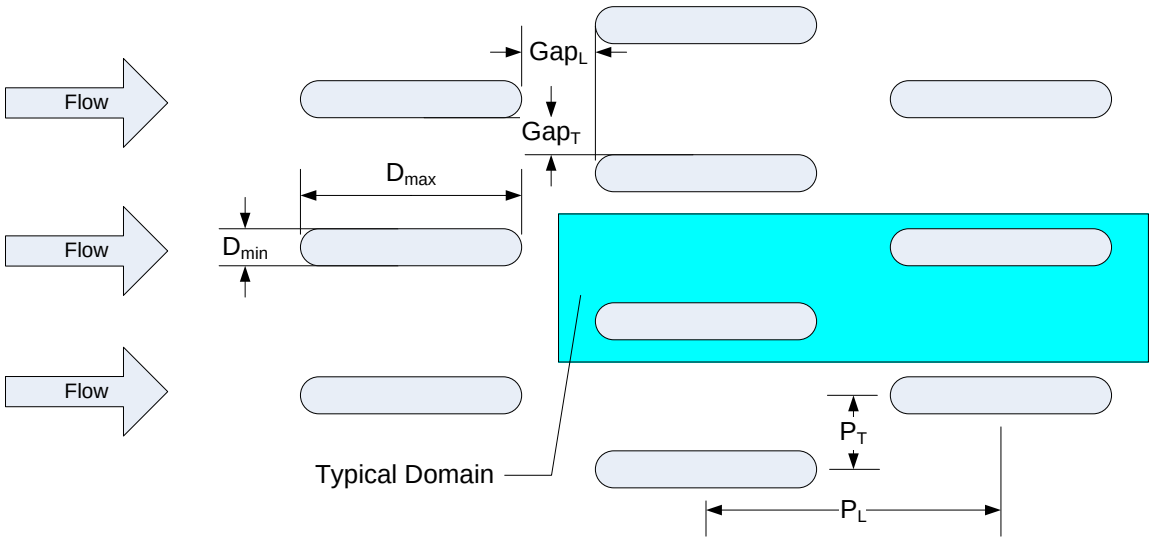

Figure 5-1. Computational domain geometry: staggered array of flat tubes.

Figure 5-1 also shows the definition of the geometric parameters used to define the array geometry. The spacing between tubes is defined by the longitudinal pitch (P_L) and transverse pitch (P_T). The distance between columns of tubes is defined as Gap_L and the distance between rows of tubes is defined as Gap_T. For convenience, the non-dimensional longitudinal and transverse pitches, S_L and S_T, respectively, are defined as shown below.

$$S_L = P_L / D_{\min} \qquad S_T = P_T / D_{\min} \qquad \text{Eq.(4.5)}$$

Nine unique domain geometries were chosen for the current work. The flat tube geometry is fixed for all nine at *AR*=6.0, but the longitudinal and transverse spacing are varied. Table 5-1 presents the definition of each domain geometry in terms of longitudinal and transverse spacing as well as in terms of the gaps between tubes. The variation in S_L and S_T is created by varying the gaps between columns and rows. Both Gap_L and Gap_T vary starting from D_{min} and increasing in increments of D_{min} /2 to a maximum of $2D_{min}$.

Table 5-1. Definition of domain geometries

Domain Name	S_L	S_T	Gap_L	Gap_T
SL7_ST2	7	2	D_{min}	D_{min}
SL7.5_ST2	7.5	2	$3D_{min}/2$	D_{min}
SL8_ST2	8	2	$2D_{min}$	D_{min}
SL7_ST2.5	7	2.5	D_{min}	$3D_{min}/2$
SL7.5_ST2.5	7.5	2.5	$3D_{min}/2$	$3D_{min}/2$
SL8_ST2.5	8	2.5	$2D_{min}$	$3D_{min}/2$
SL7_ST3	7	3	D_{min}	$2D_{min}$
SL7.5_ST3	7.5	3	$3D_{min}/2$	$2D_{min}$
SL8_ST3	8	3	$2D_{min}$	$2D_{min}$

5.2 CVFEM Mesh

A computer code was developed to provide the CVFEM mesh for each of the domains of interest. The term *mesh* here refers to the triangular element mesh required by the CVFEM.

The mesh geometry is fully defined by specification of D_{min}, *AR*, S_L, and S_T. The coarseness/fineness of the mesh is determined by a parameter θ_{arc} specified in degrees. θ_{arc} determines the length of the equal-length chords that approximate the curved end of each tube. The number of chord segments is determined by $180^{\circ}/\theta_{arc}$ such that θ_{arc} is the

included angle for each chord. Once this chord length has been determined, it is used as a base length for the remainder of the mesh. Throughout the domain, except in proximity of the curved tube ends, the base length is used as the element edge length. Near the tube, a region of finer elements with edge length one-half the base length is used to provide better grid resolution for the calculation of spatial derivatives.

Figure 5-2 shows a typical mesh. Each element is a right triangle and the nodes are arranged along lines of constant x and constant y. The mesh definition is communicated from the mesher code to the CVFEM code through a set of text files. The ***NodeFile*** is a listing of {Node Number, x, y} representing the location of the nodes. The ***ElementFile*** is a listing of {Element Number, N1, N2, N3} where N1, N2, and N3 are the node numbers of the element's three nodes. There are also files ***Tube1File*** and ***Tube2File*** that are listings of nodes along the surface of each of the two tubes in the domain. The listing starts with a node at a specific location and lists nodes in order as one travels along the surface in a counterclockwise fashion. These tube node listings are used when performing calculations for Nusselt number, skin friction, and pressure drag along the tube surfaces.

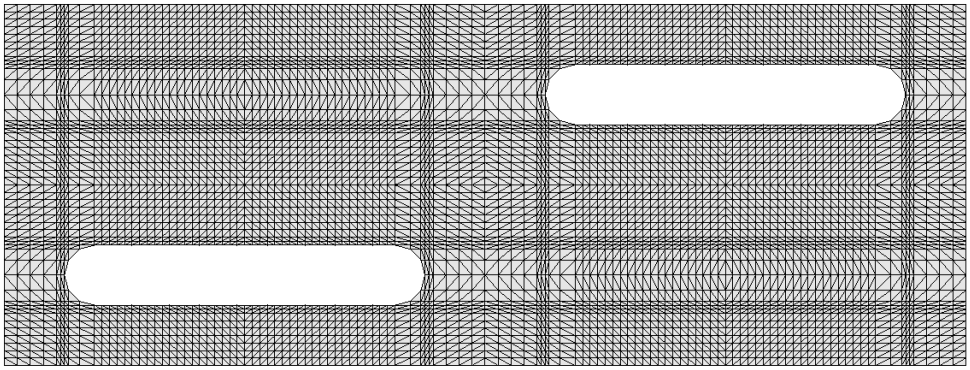

Figure 5-2. Typical CVFEM element mesh.

5.3 Grid Independence Study

For the current work, the cases of interest involve laminar oscillatory flow in the transition regime between steady laminar flow and fully turbulent flow. For the chosen geometry, a maximum Reynolds number of 2000 was chosen to avoid the turbulent regime. To determine grid independence for the current work, two domains were used: SL7_ST2 and SL8_ST3. SL7_ST2 is the domain with minimum S_L and minimum S_T. SL8_ST3 is the domain with maximum S_L and maximum S_T. Figure 5-3 shows these two domains plotted to scale for comparison. For each of these two domains, a solution at $Re \approx 2000$ was obtained with a coarse mesh. Subsequent solutions were then obtained with finer meshes while monitoring the values of certain flow and heat transfer parameters. Once the parameter values had stopped changing within reasonable limits, the grid independence exercise was stopped.

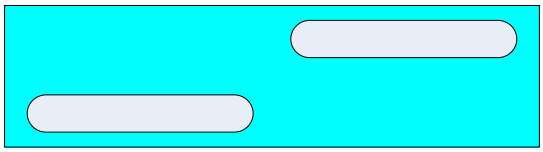

(a)

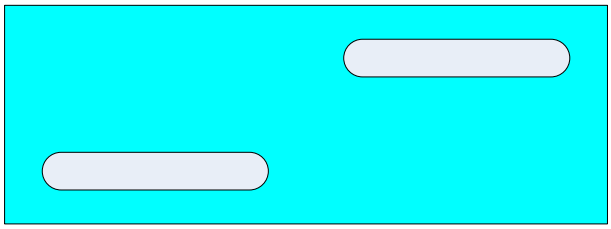

(b)

Figure 5-3. Comparison of domains used for grid independence study: (a) SL7_ST2; (b) SL8_ST3.

Table 5-2 shows the description of the SL7_ST2 meshes used for the grid independence study in terms of the number of elements, nodes, rows, and columns. A different seed value of θ_{arc} was used for each mesh. Using the coarsest mesh, it was determined by a series of solutions that $\beta = 4.0$ produced $Re \approx 2000$. The same β value was used for the solutions with the other meshes.

Table 5-2. Description of SL7_ST2 meshes for grid independence study

Model	#ELEM	#NODE	#Rows	#Cols	#Tube	θ_{arc} (deg)
SL7_ST2_26	21152	11011	65	197	176	15
SL7_ST2_25	44872	23083	93	293	264	10
SL7_ST2_27	84608	43175	129	393	352	7.5
SL7_ST2_28	128664	65423	157	493	444	6

For each solution at $\beta = 4.0$, *Re*, *Nu*, and friction factor (*f*) were determined. Table 5-3 shows the data from all of the SL7_ST2 grid independence solutions. The percent difference for each parameter is calculated with respect to the parameter value for the solution using the finest mesh, assuming that that is closest to the ideal solution. The solution time given in the last column is the number of clock hours of solving time required per one second of solution time. For $Re \approx 2000$, five seconds of solution time were required to obtain repeating oscillations. Table 5-3 shows that the flow parameters, *Re* and *f*, are both within 1.5% of the finest mesh value on the coarsest mesh used. However, the *Nu* for the coarsest mesh was 27% lower than that for the finest mesh. The *Nu* at the third mesh, SL7_ST2_27, is within 4.1% of the finest model. Based on this data, it was decided to use SL7ST2_27 for the study. Note that this choice represents 35% fewer elements and a savings of over one-half the required solution time than for SL7_ST2_28.

Table 5-3. Grid independence results: SL7_ST2 at $\beta = 4.0$

Model	*Re*	%Δ*Re*	*f*	%Δ*f*	*Nu*	%Δ*Nu*	Solution Time (hr/sec)
SL7_ST2_26	2030.9	-0.7%	0.045367	1.4%	40.43	-27.0%	0.392
SL7_ST2_25	2035.8	-0.4%	0.045146	0.9%	47.31	-14.6%	1.22
SL7_ST2_27	2042.4	-0.1%	0.044859	0.2%	53.15	-4.1%	3.32
SL7_ST2_28	2044.7	----------	0.044758	----------	55.41	----------	6.84

The same procedure as described above for SL7_ST2 was used for the grid independence study for SL8_ST3. Table 5-4 shows the mesh description of all the SL8_ST3 meshes used. For this domain geometry, it was determined that $\beta = 1.25$

produced $Re \approx 2000$. Table 5-5 shows the grid independence solution data. Based on the data, SL8_ST_12 was chosen. This choice represents 39% fewer elements and solution time savings of over 50% compared to SL8_ST3_13.

Table 5-4. Description of SL8_ST3 meshes for grid independence study

Model	#ELEM	#NODE	#Rows	#Cols	#Tube	θ_{arc} (deg)
SL8_ST3_10	34336	17643	93	209	176	15
SL8_ST3_11	79624	40531	141	317	264	10
SL8_ST3_12	138816	70363	185	421	352	7.5
SL8_ST3_13	226264	114343	237	533	444	6

Table 5-5. Grid independence results: SL8_ST3 at $\beta = 1.25$

Model	*Re*	%Δ*Re*	*f*	%Δ*f*	*Nu*	%Δ*Nu*	Solution Time (hr/sec)
SL8_ST3_10	1968.5	0.02274	0.050932	0.047165	50.78	-0.09644	0.66
SL8_ST3_11	1981.1	0.01648	0.050282	0.033801	56.53	0.005872	2.2
SL8_ST3_12	1998.3	0.00794	0.04942	0.016078	56.88	0.0121	5.4
SL8_ST3_13	2014.3	----------	0.048638	----------	56.2	----------	11.2

Using the two domain geometries representing the extremes in size, meshes were chosen for each that were built with the seed value of $\theta_{arc} = 7.5^{\circ}$. Therefore, the seed value of $\theta_{arc} = 7.5^{\circ}$ was used for the remaining seven meshes in the nine-mesh set.

Table 5-6 lists the characteristics of the meshes used for all nine domain geometries. From this point forward, the model names will include only the S_L and S_T

values. For example, the chosen meshes from above, SL7_ST2_27 and SL8_ST3_12 will be referred to as SL7_ST2 and SL8_ST3, respectively, from this point forward.

Table 5-6. Description of meshes for all computational domains

Model	#ELEM	#NODE	#Rows	#Cols	#Tube	θ_{arc} (deg)
SL7_ST2	84608	43175	129	393	352	7.5
SL7_ST2.5	106560	54179	157	393	352	7.5
SL7_ST3	128512	65183	185	393	352	7.5
SL7.5_ST2	85440	43603	125	409	352	7.5
SL7.5_ST2.5	111552	56691	157	409	352	7.5
SL7.5_ST3	134400	68143	185	409	352	7.5
SL8_ST2	88416	45103	125	421	352	7.5
SL8_ST2.5	115296	58575	157	421	352	7.5
SL8_ST3	138816	70363	185	421	352	7.5

5.4 Time Step Independence

Based on the experience gained in replicating the Zhang *et al*. [14] results as described above, the geometric dimensions of the domains were chosen such that at the maximum Reynolds number the highest expected frequency was 40 Hz or less. Based on Zhang *et al.* [14] and Mujamdar and Amon [9], among others, the cases were expected to produce only one primary frequency of interest. For the expected 40 Hz maximum frequency, a time step of $t = 0.001s$ provides 25 time steps to resolve one period of oscillation. For lower frequencies, a time step of $t = 0.001s$ provides even more time steps to resolve one period of oscillation. Therefore, $t = 0.001s$ was considered more than sufficient for the current work and a time step of $t = 0.001s$ was used for all cases.

As a check, some cases were solved with smaller time step of $t = 0.0001s$. The resulting parameter values were well within 0.5% of the corresponding values for a $t = 0.001s$ solution at the cost of more than doubling the solution time. This data is not included here.

5.5 Unsteady Solutions

For each of the nine domain geometries of interest, a series of solutions was obtained by varying the global pressure gradient β.

For each geometry, the procedure began with a series of solutions using a coarse mesh to establish a β value to produce $Re \approx 2000$. (For the two grid independence cases, this β value had already been established.) Using a coarse mesh saved solution time as compared to the prospect of using the finer $\theta_{arc} = 7.5^{\circ}$ mesh. Once this value of β was determined, a solution was obtained using a $\theta_{arc} = 7.5^{\circ}$ mesh at this β value. After that, values of β were chosen to produce *Re*<2000. If oscillations were observed, the solution was allowed to continue until the oscillations became repeating and average parameter values stopped changing within reasonable limits. There was no predetermined list of β values for each domain and each domain had its unique list of values. The values used are not listed here. Instead, these values will appear below in the detailed discussion of results.

For oscillating cases, values for *Re*, *f*, and *Nu* were saved for each time step. Time-averaged values of these quantities were obtained post solution. The values for *u*-velocity and *v*-velocity were saved at each time step for one node in the domain. This

node is located along the upper transverse boundary aligned with the center of the flat tube. The node is in the same relative position for each geometric domain. Using the *u*-velocity and *v*-velocity data from this node, the frequency of oscillation and peak-to-peak magnitude of the oscillations could be obtained. These values are listed in the tables below. The frequency value obtained in this way is representative of the flow in the entire domain although there are phase differences between oscillations at different points.

5.5.1 Note on Required Solution Times

Most of the solutions for the current work were obtained using a desktop PC having an Intel Xeon processor chip with eight processors. OpenMP directives were used to take advantage of the multiple processors available for parallel computing. On the PC, test runs were done using two, three, four, five, and six processors and solution times were compared to the non-parallel solution. Solution times decreased for the case of two, three, and four processors, but increased for the case of five and six processors as compared to the non-parallel solution time. This result indicates that for the problem being solved, the overhead required to set up parallel execution directives outweighs the decrease in solution time for the five and six processor case. Similar results were obtained on the Texas A&M Supercomputer. For the case of four processors, solution was approximately 2.5 times faster than the non-parallel solution. OpenMP directives specifying the use of four processors were used for all cases.

SL8_ST3 is the largest mesh used in the current work at 138816 elements. This is relatively small compared to some CFD codes due to use of DC conditions. For a

larger mesh with, say, one million elements, the extra overhead involved in setting up the OpenMP directives for five, six, or more processors may have resulted in an overall decrease in solution time.

The grid independence effort using SL8_ST3, as shown above, required 27 hrs of clock time to obtain 5 seconds worth of solution time. For lower β values, this amount of time increases substantially. For example, at $\beta = 0.375$ the SL8_ST3 geometry required over 80 hours of clock time to obtain 15 seconds worth of solution time. For this case, the oscillations did not become cyclic until t=15 seconds.

In all, the unsteady solutions for the current work required over 2000 hours of clock time for solution.

5.5.2 Tabular Listing of Unsteady Results

Table 5-7, Table 5-8, and Table 5-9 present the unsteady results for the SL7, SL7.5, and SL8 cases respectively. As a set, these three tables present all the unsteady data.

Each table presents values for stream-wise pressure gradient (β), Reynolds number (*Re*), friction factor (*f*), Strouhal number (*Str*), normalized oscillation amplitude ($\overline{PTP}$), tube skin friction coefficient ($C_{D,skin}$), tube pressure drag coefficient ($C_{D,press}$), percent tube skin friction, percent tube pressure drag, non-dimensional pumping power (ψ) and Nusselt number (*Nu*). β was chosen as an input to the solution process. The values for *Re*, ψ and *Nu* are time-averaged values over an integral number of periods of oscillation. For each case, skin friction drag and pressure drag on each tube surface were

calculated at each time step. The time-averages of each were added to produce a total. In addition to the non-dimensional coefficients $C_{D,skin}$ and $C_{D,press}$, the tables present the percentage of that total that skin and pressure drag each represents. $\overline{PTP}$ is the peak-to-peak amplitude of the *u*-velocity normalized by the time-averaged *u*-velocity at the node location described above. The data associated with Re_{crit} is shaded in each table for each domain geometry. Determination of Re_{crit} is discussed below in Section 5.7.

5.5.3 Notes on Unsteady Solution Characteristics

This section provides information on the characteristics of the unsteady solutions obtained. The remarks here say little about the actual physics of the problem and more about the solution method and boundary conditions.

Each unsteady solution was started at t=0 with all fluid velocities set to zero (quiescent fluid). Comparing two oscillatory solutions, one with β_1 and the other with β_2, such that $\beta_1 > \beta_2$, then the β_1 solution will begin oscillating earlier than β_2 solution in solution time. Figure 5-4 shows a plot of *u*-velocity versus time for two such solutions.

Another characteristic of these unsteady solutions is that the Reynolds number approaches a steady value prior to the onset of oscillations. After oscillations begin, the Reynolds number decreases to a new average value. For the cases above, with $\beta_1 > \beta_2$, the percent change in average *Re* is higher for the higher β case as shown in Figure 5-5.

Table 5-7. Unsteady data for SL7 cases

SL7_ST2	β	*Re*	*f*	*Str*	$\overline{PTP}$	$C_{D,skin}$	$C_{D,press}$	*Skin Friction*	*Pressure Drag*	ψ	*Nu*
	1.711	1157.8	0.0604			0.18	0.13	58%	42%	6.83E+08	31.0
	2.000	1273.3	0.0577	0.124	0.13	0.16	0.13	56%	44%	8.69E+08	34.4
	3.000	1673.9	0.0501	0.123	0.21	0.13	0.12	51%	49%	1.71E+09	46.7
	4.000	2042.4	0.0449	0.123	0.24	0.11	0.12	48%	52%	2.79E+09	53.3
SL7_ST2.5	β	*Re*	*f*	*Str*	$\overline{PTP}$	$C_{D,skin}$	$C_{D,press}$	*Skin Friction*	*Pressure Drag*	ψ	*Nu*
	0.589	765.2	0.0966			0.31	0.20	61%	39%	1.62E+08	29.8
	0.875	981.8	0.0829	0.140	0.18	0.25	0.19	57%	43%	2.93E+08	39.3
	1.250	1265.5	0.0713	0.139	0.23	0.21	0.18	54%	46%	5.39E+08	49.2
	1.750	1613.7	0.0614	0.136	0.26	0.17	0.16	51%	49%	9.63E+08	53.6
	2.000	1777.5	0.0578	0.137	0.27	0.15	0.16	50%	50%	1.21E+09	54.1
	2.400	2027.8	0.0533	0.134	0.28	0.14	0.15	48%	52%	1.66E+09	54.6
SL7_ST3	β	*Re*	*f*	*Str*	$\overline{PTP}$	$C_{D,skin}$	$C_{D,press}$	*Skin Friction*	*Pressure Drag*	ψ	*Nu*
	0.350	724.6	0.1091			0.37	0.23	62%	38%	8.97E+07	29.5
	0.500	914.8	0.0943	0.151	0.14	0.31	0.22	59%	41%	1.56E+08	37.2
	0.750	1230.8	0.0782	0.148	0.18	0.24	0.19	55%	45%	3.15E+08	46.9
	1.000	1519.9	0.0683	0.146	0.20	0.20	0.18	53%	47%	5.18E+08	53.7
	1.250	1786.4	0.0618	0.144	0.23	0.17	0.17	51%	49%	7.62E+08	57.7
	1.500	2035.3	0.0572	0.139	0.25	0.15	0.16	49%	51%	1.04E+09	59.4

Table 5-8. Unsteady data for SL7.5 cases

SL7.5_ST2	β	*Re*	*f*	*Str*	$\overline{PTP}$	$C_{D,skin}$	$C_{D,press}$	*Skin Friction*	*Pressure Drag*	ψ	*Nu*
	1.592	1176.9	0.0549			0.17	0.13	57%	43%	7.00E+08	31.5
	2.000	1353.8	0.0511	0.114	0.16	0.16	0.13	55%	45%	9.90E+08	37.1
	2.500	1570.7	0.0474	0.114	0.21	0.14	0.12	53%	47%	1.44E+09	44.1
	3.000	1776.1	0.0445	0.112	0.25	0.12	0.12	51%	49%	1.95E+09	49.2
	3.500	1972.4	0.0421	0.114	0.27	0.11	0.12	49%	51%	2.52E+09	51.5
SL7.5_ST2.5	β	*Re*	*f*	*Str*	$\overline{PTP}$	$C_{D,skin}$	$C_{D,press}$	*Skin Friction*	*Pressure Drag*	ψ	*Nu*
	0.542	770.1	0.0865			0.30	0.20	61%	39%	1.58E+08	30.3
	0.750	944.7	0.0768	0.128	0.18	0.26	0.19	58%	42%	2.59E+08	37.9
	1.000	1155.0	0.0685	0.127	0.23	0.22	0.18	55%	45%	4.22E+08	46.1
	1.500	1541.2	0.0577	0.127	0.29	0.17	0.16	52%	48%	8.45E+08	51.4
	1.800	1755.6	0.0534	0.125	0.31	0.16	0.15	50%	50%	1.15E+09	51.7
	2.200	2025.6	0.0490	0.125	0.33	0.14	0.15	48%	52%	1.63E+09	52.1
SL7.5_ST3	β	*Re*	*f*	*Str*	$\overline{PTP}$	$C_{D,skin}$	$C_{D,press}$	*Skin Friction*	*Pressure Drag*	ψ	*Nu*
	0.309	721.6	0.0994			0.37	0.23	62%	38%	8.64E+07	30.0
	0.500	978.0	0.0825	0.139	0.17	0.29	0.21	58%	42%	1.79E+08	40.5
	0.750	1314.4	0.0685	0.137	0.21	0.22	0.19	54%	46%	3.60E+08	50.1
	1.000	1620.5	0.0601	0.134	0.23	0.19	0.17	52%	48%	5.92E+08	55.5
	1.375	2037.2	0.0523	0.132	0.27	0.15	0.16	49%	51%	1.02E+09	58.6

Table 5-9. Unsteady data for SL8 cases

SL8_ST2	β	*Re*	*f*	*Str*	$\overline{PTP}$	$C_{D,skin}$	$C_{D,press}$	*Skin Friction*	*Pressure Drag*	ψ	*Nu*
	1.524	1191.3	0.0505	0.000		0.17	0.13	57%	43%	7.11E+08	32.0
	1.750	1298.3	0.0486	0.106	0.14	0.16	0.13	55%	45%	8.86E+08	35.3
	2.000	1416.5	0.0466	0.106	0.18	0.15	0.13	54%	46%	1.10E+09	39.1
	2.500	1640.0	0.0435	0.104	0.24	0.13	0.13	51%	49%	1.60E+09	46.1
	2.875	1798.2	0.0416	0.105	0.28	0.12	0.12	50%	50%	2.02E+09	48.9
	3.250	1948.9	0.0400	0.105	0.31	0.12	0.12	49%	51%	2.47E+09	49.6
SL8_ST2.5	β	*Re*	*f*	*Str*	$\overline{PTP}$	$C_{D,skin}$	$C_{D,press}$	*Skin Friction*	*Pressure Drag*	ψ	*Nu*
	0.513	787.5	0.0783	0.000		0.29	0.19	60%	40%	1.63E+08	30.8
	0.750	994.3	0.0693	0.120	0.21	0.25	0.19	57%	43%	2.91E+08	40.4
	1.000	1212.7	0.0621	0.118	0.27	0.21	0.18	55%	45%	4.73E+08	47.4
	1.500	1605.8	0.0532	0.117	0.36	0.17	0.16	51%	49%	9.39E+08	49.1
	2.000	1949.4	0.0481	0.117	0.43	0.15	0.16	49%	51%	1.52E+09	49.7
SL8_ST3	β	*Re*	*f*	*Str*	$\overline{PTP}$	$C_{D,skin}$	$C_{D,press}$	*Skin Friction*	*Pressure Drag*	ψ	*Nu*
	0.282	724.3	0.0903	0.000		0.36	0.23	61%	39%	8.47E+07	30.6
	0.500	1030.8	0.0743	0.128	0.20	0.27	0.21	57%	43%	2.01E+08	43.7
	0.750	1382.9	0.0619	0.126	0.25	0.22	0.18	54%	46%	4.04E+08	52.2
	1.000	1702.9	0.0544	0.124	0.27	0.18	0.17	51%	49%	6.64E+08	55.4
	1.250	1998.4	0.0494	0.123	0.30	0.16	0.16	49%	51%	9.74E+08	57.2

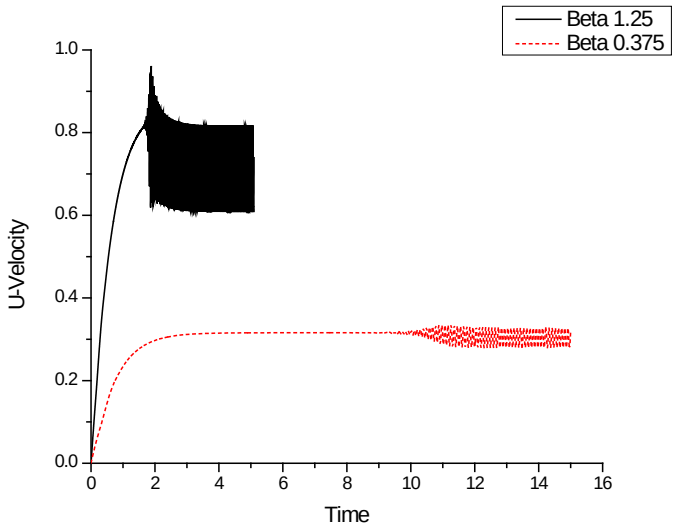

Figure 5-4. Oscillating u-velocity at a point for two values of β.

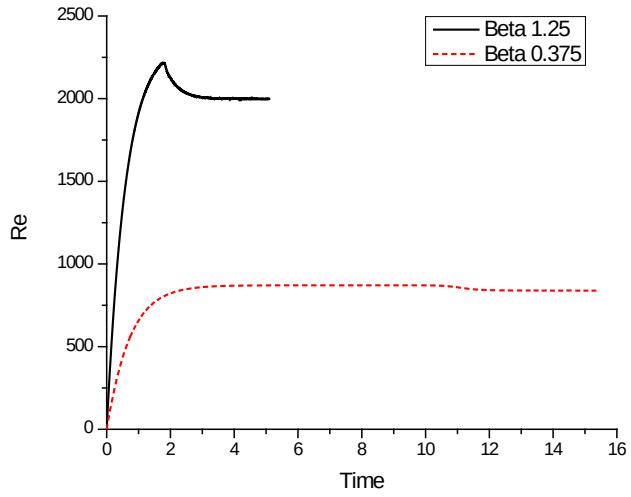

Figure 5-5. Reynolds number versus time for two values of β.

The fact that smaller values of β (and therefore smaller *Re*) lead to much longer solution times presents a problem in determining Re_{crit}. Cases near Re_{crit} are very expensive to run in terms of computer resources. Since Re_{crit} is unknown ahead of time,

at some time in the solution process one cannot be certain whether a particular case demonstrates steady, non-oscillatory behavior or has simply not yet reached the onset of oscillations. For example, in Figure 5-4, if one were to check the solution for the $\beta = 0.375$ case at *t*=8*s*, one may decide that this represents a steady, non-oscillatory case based on the data from *t*=0*s* to *t*=8*s*.

That fact that the *Re* drop decreases as the Re_{crit} is approached was used to set a limit on the number of solutions obtained for each geometry. As smaller and smaller β values were used, once an oscillating solution was found such that the percentage change in the "steady" *Re* and average oscillating *Re* was approximately 5%, no more solutions were obtained.

5.6 Steady Solutions

A version of the CVFEM code was developed which produced pseudo-steady solutions for a range of *Re* starting at $Re<Re_{crit}$ and overlapping the *Re* range producing self-sustained oscillations. The term pseudo-steady here refers to the fact that these solutions were obtained with a modified version of the unsteady code with the main difference being that symmetry was enforced along the stream-wise centerline of the domain. Applying symmetry in this way effectively prevents oscillations from developing [15]. In this way, a "steady" solution may be obtained for a β case that is known to produce an oscillatory flow with the unmodified unsteady code. These solutions are used as a comparison with the oscillatory solutions.

The code used to produce pseudo-steady solutions for $Re>Re_{crit}$ produces true steady solutions for $Re<Re_{crit}$ that match the solutions produced by the steady version of the code. It should be noted that the steady code used in validation is unable to produce a solution for SSOF cases. The solution will diverge. The pseudo-steady solution is based on the unsteady code which parcels out the source term in small increments allowing the solution to continue to convergence.

5.6.1 Tabular Listing of Steady Results

Table 5-10, Table 5-11, and Table 5-12 present the steady results for the SL7, SL7.5, and SL8 cases, respectively. As a set, these three tables present all the steady data.

Each table presents values for stream-wise pressure gradient (β), Reynolds number (*Re*), friction factor (*f*), tube skin friction coefficient ($C_{D,skin}$), tube pressure drag coefficient ($C_{D,press}$), percent tube skin friction, percent tube pressure drag, non-dimensional pumping power (ψ) and Nusselt number (*Nu*). β was chosen as an input to the solution process. For β values producing $Re<Re_{crit}$, these solutions are truly steady solutions. For β values producing $Re \geq Re_{crit}$, these solutions are pseudo-steady as discussed above. As these are not oscillatory solutions, there is no *Str* or $\overline{PTP}$ value listed for each case. The data associated with Re_{crit} is shaded in each table for each domain geometry.

Table 5-10. Steady data for SL7 cases

SL7_ST2	β	*Re*	*f*	$C_{D,skin}$	$C_{D,press}$	*Skin Friction*	*Pressure Drag*	ψ	*Nu*
	1.000	745.0	0.0843	0.26	0.16	62%	38%	2.54E+08	31.0
	1.500	1033.2	0.0657	0.20	0.14	59%	41%	5.29E+08	30.9
	1.711	1157.8	0.0604	0.18	0.13	58%	42%	6.83E+08	31.0
	1.750	1169.6	0.0598	0.18	0.13	58%	42%	6.98E+08	31.0
	2.000	1302.1	0.0552	0.16	0.12	56%	44%	8.88E+08	31.1
	3.000	1802.3	0.0432	0.12	0.10	53%	47%	1.84E+09	31.4
SL7_ST2.5	β	*Re*	*f*	$C_{D,skin}$	$C_{D,press}$	*Skin Friction*	*Pressure Drag*	ψ	*Nu*
	0.500	652.2	0.1074	0.36	0.22	62%	38%	1.11E+08	29.7
	0.589	765.2	0.0966	0.31	0.20	61%	39%	1.62E+08	29.8
	0.750	908.7	0.0830	0.26	0.18	59%	41%	2.32E+08	30.0
	0.875	1030.5	0.0753	0.24	0.17	58%	42%	3.08E+08	30.2
	1.250	1378.0	0.0601	0.18	0.14	56%	44%	5.88E+08	30.7
	1.750	1811.8	0.0487	0.14	0.12	53%	47%	1.08E+09	31.1
	2.000	2019.4	0.0448	0.12	0.12	52%	48%	1.38E+09	31.3
	2.400	2341.4	0.0400	0.11	0.11	50%	50%	1.92E+09	30.5
SL7_ST3	β	*Re*	*f*	$C_{D,skin}$	$C_{D,press}$	*Skin Friction*	*Pressure Drag*	ψ	*Nu*
	0.200	445.8	0.1589	0.57	0.31	65%	35%	3.04E+07	28.9
	0.300	624.1	0.1216	0.42	0.25	63%	37%	6.39E+07	29.3
	0.350	724.6	0.1091	0.37	0.23	62%	38%	8.97E+07	29.5
	0.400	791.8	0.1007	0.34	0.22	61%	39%	1.08E+08	29.7
	0.500	952.0	0.0871	0.29	0.20	60%	40%	1.62E+08	30.0
	0.750	1329.8	0.0670	0.21	0.16	57%	43%	3.40E+08	30.7
	1.000	1684.8	0.0556	0.17	0.14	55%	45%	5.75E+08	31.1
	1.250	2023.2	0.0482	0.14	0.13	53%	47%	8.63E+08	31.4
	1.500	2348.6	0.0429	0.13	0.12	52%	48%	1.20E+09	31.7

Table 5-11. Steady data for SL7.5 cases

SL7.5_ST2	β	*Re*	*f*	$C_{D,skin}$	$C_{D,press}$	*Skin Friction*	*Pressure Drag*	ψ	*Nu*
	1.000	803.0	0.0725	0.25	0.16	61%	39%	2.93E+08	31.3
	1.500	1118.8	0.0568	0.18	0.13	58%	42%	6.21E+08	31.4
	1.592	1176.9	0.0549	0.17	0.13	57%	43%	7.00E+08	31.5
	2.000	1399.8	0.0478	0.15	0.12	56%	44%	1.02E+09	31.7
	2.500	1673.1	0.0418	0.12	0.11	54%	46%	1.53E+09	32.0
	3.000	1935.4	0.0375	0.11	0.10	52%	48%	2.12E+09	32.3
	3.500	2188.8	0.0342	0.10	0.09	51%	49%	2.80E+09	32.5
SL7.5_ST2.5	β	*Re*	*f*	$C_{D,skin}$	$C_{D,press}$	*Skin Friction*	*Pressure Drag*	ψ	*Nu*
	0.250	403.0	0.1406	0.53	0.29	65%	35%	3.68E+07	29.9
	0.500	708.4	0.0910	0.33	0.20	62%	38%	1.29E+08	30.2
	0.542	770.1	0.0865	0.30	0.20	61%	39%	1.58E+08	30.3
	0.750	984.8	0.0707	0.24	0.17	59%	41%	2.70E+08	30.7
	1.000	1243.4	0.0591	0.20	0.15	57%	43%	4.54E+08	31.1
	1.500	1727.0	0.0459	0.14	0.12	53%	47%	9.46E+08	31.8
	1.800	2001.8	0.0410	0.12	0.12	52%	48%	1.32E+09	32.1
	2.200	2355.0	0.0362	0.11	0.11	50%	50%	1.89E+09	32.4
SL7.5_ST3	β	*Re*	*f*	$C_{D,skin}$	$C_{D,press}$	*Skin Friction*	*Pressure Drag*	ψ	*Nu*
	0.100	274.8	0.2090	0.84	0.41	67%	33%	1.00E+07	29.0
	0.200	486.0	0.1337	0.52	0.29	64%	36%	3.55E+07	29.4
	0.300	678.3	0.1029	0.39	0.23	62%	38%	7.43E+07	29.9
	0.309	721.6	0.0994	0.37	0.23	62%	38%	8.64E+07	30.0
	0.500	1031.2	0.0742	0.26	0.18	59%	41%	1.88E+08	30.8
	0.750	1437.4	0.0573	0.19	0.15	56%	44%	3.94E+08	31.5
	1.000	1819.0	0.0477	0.16	0.13	54%	46%	6.65E+08	32.0
	1.375	2359.6	0.0390	0.12	0.11	52%	48%	1.19E+09	32.6

Table 5-12. Steady data for SL8 cases

SL8_ST2	β	*Re*	*f*	$C_{D,skin}$	$C_{D,press}$	*Skin Friction*	*Pressure Drag*	ψ	*Nu*
	1.000	848.4	0.0650	0.23	0.16	60%	40%	3.31E+08	31.7
	1.500	1172.6	0.0510	0.17	0.13	57%	43%	6.85E+08	32.0
	1.524	1191.3	0.0505	0.17	0.13	57%	43%	7.11E+08	32.0
	1.750	1325.9	0.0466	0.16	0.12	56%	44%	9.05E+08	32.2
	2.000	1474.6	0.0430	0.14	0.12	54%	46%	1.15E+09	32.4
	2.500	1761.3	0.0377	0.12	0.11	53%	47%	1.72E+09	32.8
	2.875	1968.5	0.0347	0.11	0.10	51%	49%	2.21E+09	33.0
	3.250	2170.2	0.0323	0.10	0.10	50%	50%	2.75E+09	33.2
SL8_ST2.5	β	*Re*	*f*	$C_{D,skin}$	$C_{D,press}$	*Skin Friction*	*Pressure Drag*	ψ	*Nu*
	0.250	430.5	0.1232	0.50	0.28	64%	36%	4.19E+07	30.1
	0.500	754.1	0.0803	0.31	0.20	61%	39%	1.47E+08	30.7
	0.513	787.5	0.0783	0.29	0.19	60%	40%	1.63E+08	30.8
	0.750	1046.2	0.0626	0.23	0.17	58%	42%	3.06E+08	31.3
	1.000	1319.4	0.0525	0.18	0.15	56%	44%	5.14E+08	31.9
	1.500	1829.8	0.0409	0.14	0.12	53%	47%	1.07E+09	32.7
	2.000	2308.2	0.0343	0.11	0.11	50%	50%	1.80E+09	33.2
SL8_ST3	β	*Re*	*f*	$C_{D,skin}$	$C_{D,press}$	*Skin Friction*	*Pressure Drag*	ψ	*Nu*
	0.100	295.5	0.1808	0.78	0.39	67%	33%	1.15E+07	29.1
	0.282	724.3	0.0903	0.36	0.23	61%	39%	8.47E+07	30.6
	0.300	724.7	0.0902	0.36	0.23	61%	39%	8.48E+07	30.6
	0.500	1098.7	0.0654	0.25	0.18	58%	42%	2.14E+08	31.6
	0.750	1528.8	0.0507	0.18	0.15	55%	45%	4.47E+08	32.4
	1.000	1932.8	0.0423	0.15	0.13	53%	47%	7.54E+08	32.9
	1.250	2318.2	0.0367	0.12	0.12	51%	49%	1.13E+09	33.4

5.7 Estimation of Re_{crit}

There are at least two ways to approach the problem of determining Re_{crit} for these cases. One would be to perform linear or nonlinear stability analysis. The other would be a more empirical approach where cases were run to bracket the value of Re_{crit} and then as many cases as necessary could be run to determine the value of Re_{crit} to whatever precision is desired.

Performing linear or nonlinear stability analysis is beyond the scope of the current work. This was used on the grooved channel problem and communicating channel problem where the stability analysis was actually performed on plane channel flow, a more straightforward problem than the current one. It is not clear how applicable the plane channel stability results would be to double cyclic staggered configuration of flat tubes.

The empirical approach of bracketing the value is also untenable. As discussed above, as one approaches Re_{crit} from above, that is from cases with oscillations to lower *Re*, the time to reach the onset of oscillations increases exponentially. Performing several solutions with small negative increments of β is out of the question. Coming the other direction from known steady solutions with increasing β values, one has no way of knowing at a particular time in the solution process whether a specific case is steady or simply has not run long enough to exhibit oscillations.

At the critical point, the solution bifurcates from a steady, laminar solution to an unsteady, oscillatory solution as Reynolds number is increased from a known steady solution. The critical point should therefore be a solution to both the steady problem and

the unsteady problem. The approach here is to predict the intersection point of the *Re* versus β curves from both the unsteady and steady data to estimate a value of Re_{crit} for a given case. More specifically, the pseudo-steady *Re* versus β data were used along with the unsteady data. The pseudo-steady and steady data form continuous curves, so either set of data could be used. However, the pseudo-steady data were used because the Reynolds number range closely matches that of the unsteady data.

Figure 5-6 shows the pseudo-steady and unsteady *Re* versus β curves for a typical case. The relationship between *Re* and β is not linear as seen in the figure. One option would be to curve fit each curve and then determine from the curve fit equations the predicted intersection of the curves. However, with so few data points, the curve fits are not likely to be very accurate. Instead, for the current work, the two points from each data set for lowest *Re* and β were used to create a linear curve fit for each curve and then the intersection point is determined. This is akin to assuming that the slope of the curve at low *Re* is equal to the slope of the line formed by these two points.

After the determination of Re_{crit} for each geometric domain, a pseudo data point was created whereby values for *Nu*, *f*, ψ, and other parameters were determined using linear regression with the existing steady data set. This new pseudo data point is then included as the first point in the unsteady data for that domain. (See Table 5-7, Table 5-8, and Table 5-9 above.) Using this pseudo point data helps to illustrate some of the characteristics of the data in that it represents the intersection of steady, laminar plot and unsteady, oscillatory plot.

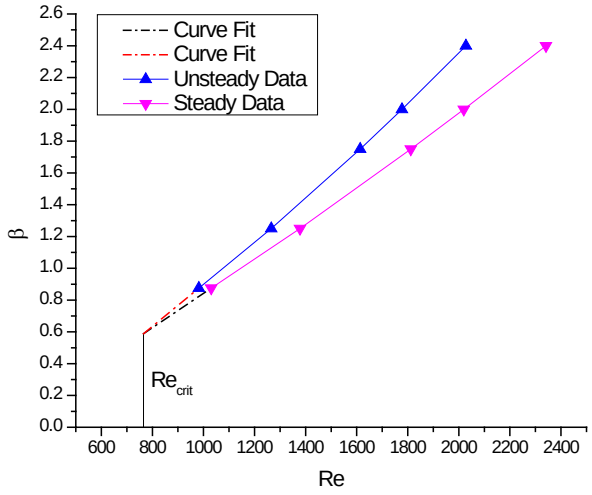

Figure 5-6. Estimation of Re_{crit} from steady and unsteady β v. Re curves.

Table 5-13 lists the estimated Re_{crit} for each domain considered. The value shown is rounded to tens-place accuracy. The value shown in parentheses is the calculated value using the curve fit method. Note that along constant S_T with increasing S_L the values of Re_{crit} show a slight increase (less than 3%) for ST2 and ST2.5. For ST3, the value of Re_{crit} is constant within the uncertainty of the values. However, along constant S_L with increasing S_T, the values of Re_{crit} show a substantial decrease. From ST2 to ST3 along SL8, there is a 40% decrease in Re_{crit}. Even considering the uncertainty involved in determining these values, this trend is clear. As the transverse spacing of tubes increases, the flow becomes destabilized at a lower Re_{crit}.

Table 5-13. Estimated values of Re_{crit}

	SL7	SL7.5	SL8
ST2	1160 (*1157.8*)	1180 (*1176.9*)	1190 (*1191.3*)
ST2.5	770 (*765.2*)	770 (*770.1*)	790 (*787.5*)
ST3	720 (*724.6*)	720 (*721.6*)	720 (*724.3*)

5.8 Discussion of Flow Results

5.8.1 General Characterization of the Flow Oscillations

There were several cases for each geometry that demonstrated self-sustained oscillations. Table 5-7, Table 5-8, and Table 5-9 above list the data for each of these cases. While the main emphasis of the current work is the effect of oscillatory flow on heat transfer and pumping power, it is worth noting some characteristic trends shown in the Strouhal number and in the $\overline{PTP}$ data.

In general, for a given geometry, the frequency of oscillation increases with increasing *Re* while the Strouhal number decreases with increasing *Re*. For the ST2 cases, the Strouhal number remains relatively constant for each domain with increasing *Re* showing a decrease of less than 2% from Re_{crit} to $Re \approx 2000$. However, for the ST2.5 and ST3 cases, the Strouhal number decreases approximately 4% and 8%, respectively, from Re_{crit} to $Re \approx 2000$. For the set of domain geometries, for constant S_L, the Strouhal number increases with increasing S_T. For constant S_T, the Strouhal number decreases with increasing S_L.

In general, the $\overline{PTP}$ *u*-velocity increases with increasing *Re* for each domain geometry. As the $\overline{PTP}$ is associated with an isolated point in each domain, these results cannot be compared across the different domain geometries.

The overall trend for any particular geometry is for frequency of oscillation to increase, Strouhal number to decrease, and $\overline{PTP}$ to increase with increasing *Re*.

5.8.2 Skin Friction and Pressure Drag

Skin friction and pressure drag on the flat tubes were calculated for each steady and unsteady case. Tables 5.7 through 5.12 list the percentage of the total that may be attributed to each for all unsteady and steady cases.

For all cases, the steady data show approximately 60% skin friction and 40% pressure drag. After the onset of oscillations, both skin friction and pressure drag increase, but the percentage of skin friction decreases while the percentage of pressure drag increases. In general, for all cases, at approximately $Re \approx 2000$, the skin friction is approximately equal to the pressure drag. This is an indication that these cases lie well within laminar range at $Re_{max} = 2000$. In the turbulent regime, the pressure drag is expected to dominate the skin friction.

While both skin friction and pressure drag show increases with increasing Reynolds number, the reported non-dimensional coefficients $C_{D,skin}$ and $C_{D,press}$ show decreases. This is due to the definitions of these parameters as given in Section 3.6.6. With increasing Reynolds number, the average inlet velocity ($\overline{u}_{inlet}$) also increases. But, the square of $\overline{u}_{inlet}$ appears in the denominator for each coefficient definition and the

value of $\overline{u}_{inlet}^2$ rises faster than the force value. This leads to a decrease in coefficient values even though the drag force values are rising.

As described in Section 3.6.6, the integrated values for skin friction and for pressure drag on the flat tubes were obtained at each time step. The Strouhal number reported in Table 5-7, Table 5-8, and Table 5-9 is the non-dimensional frequency associated with *u*- and *v*-velocity. The oscillation frequency of both the integrated skin friction and pressure drag is twice the oscillation frequency of velocity. This is due to the fact that even though the velocity components at every node in the domain oscillate at the same frequency, there are phase shifts between the *u*- and *v*-velocity at each point and between the u-velocity at all points and the v-velocity at all points. At a given time step, the sum of the skin friction and pressure drag also oscillates at a frequency twice that of the primary variables.

5.8.3 Stream Function Plots

Figure 5-7 shows a series of six plots of the stream function during one period (τ) of oscillation for SL7.5_ST2.5 at Re=2025.6. These plots are typical of the cases studied for the current work.

In Figure 5-7, dark blue represents negative values of the stream function while dark red represents positive values of the stream function. Therefore, blue and red represent opposite-hand rotation in the figures. The series of figures shows the shedding of pairs of opposite-hand rotating vortices from the tubes.

5.8.4 Pumping Power

Figure 5-8 shows non-dimensional pumping power (ψ) versus Reynolds number for all cases grouped by constant transverse spacing. In Figure 5-8, parts (a), (b), and (c) represent constant transverse spacing ST2, ST2.5, and ST3, respectively. Note that even though S_L varies for a given S_T, there is very little variation in pumping power. The curves are virtually indistinguishable in the plot.

Figure 5-9 shows non-dimensional pumping power (ψ) versus Reynolds number for all cases grouped by constant longitudinal spacing. In Figure 5-9, parts (a), (b), and (c) represent constant longitudinal spacing SL7, SL7.5, and SL3, respectively. For these plots, the steady and unsteady data are plotted with different symbols. Here, there is a clear difference in pumping power with changing S_T for constant S_L. The more compact geometry ST2 requires more pumping power to produce a given Reynolds number than for ST2.5 or ST3. As an example, for the SL7 cases at $Re \approx 2000$, the ST2 configuration ψ is 68% higher than for ST2.5 and 168% higher than for ST3. If ψ is used as a cost indicator, then it is clearly more costly to operate the more compact geometry at a given Reynolds number.

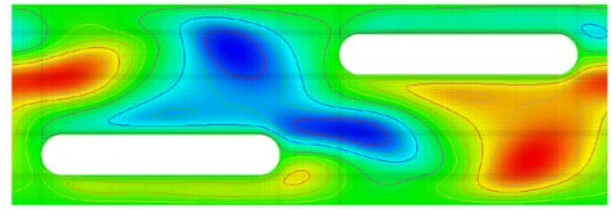

(a) t=0

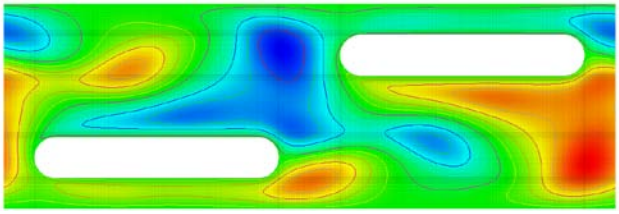

(b) $t=\tau$ /5

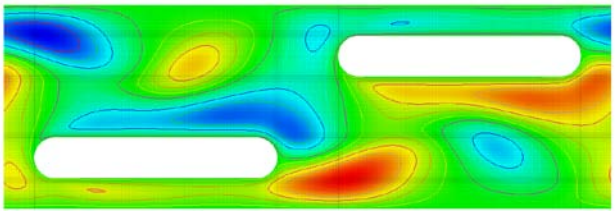

(c) t=2 τ /5

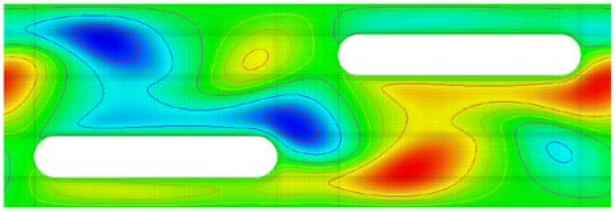

(d) t=3 τ /5

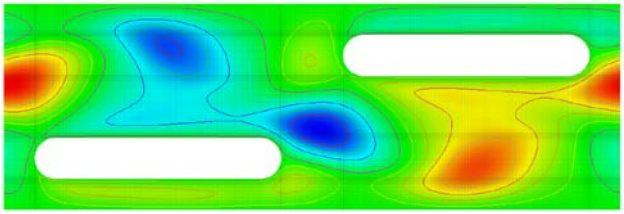

(e) t=4 τ /5

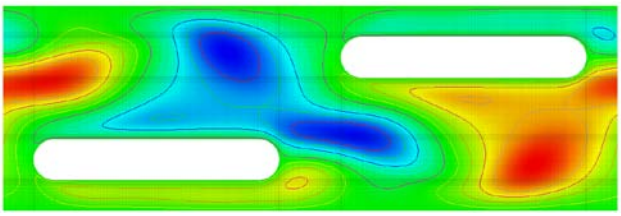

(f) $t=\tau$

Figure 5-7. Stream function plots for one period of oscillation (τ) for SL7.5_ST2.5 at Re=2025.6.

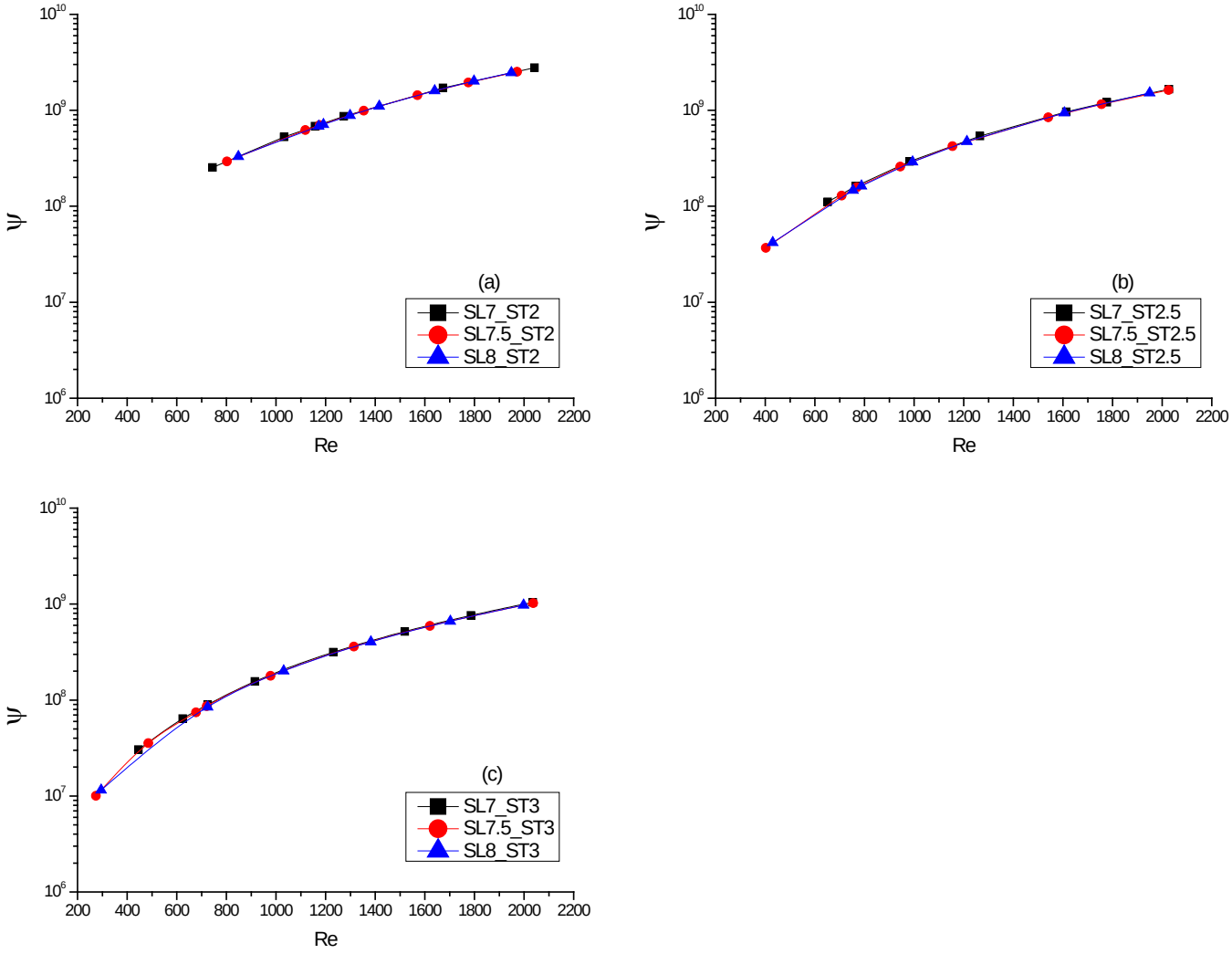

Figure 5-8. Non-dimensional pumping power (ψ) versus Reynolds number: constant S_T plots.

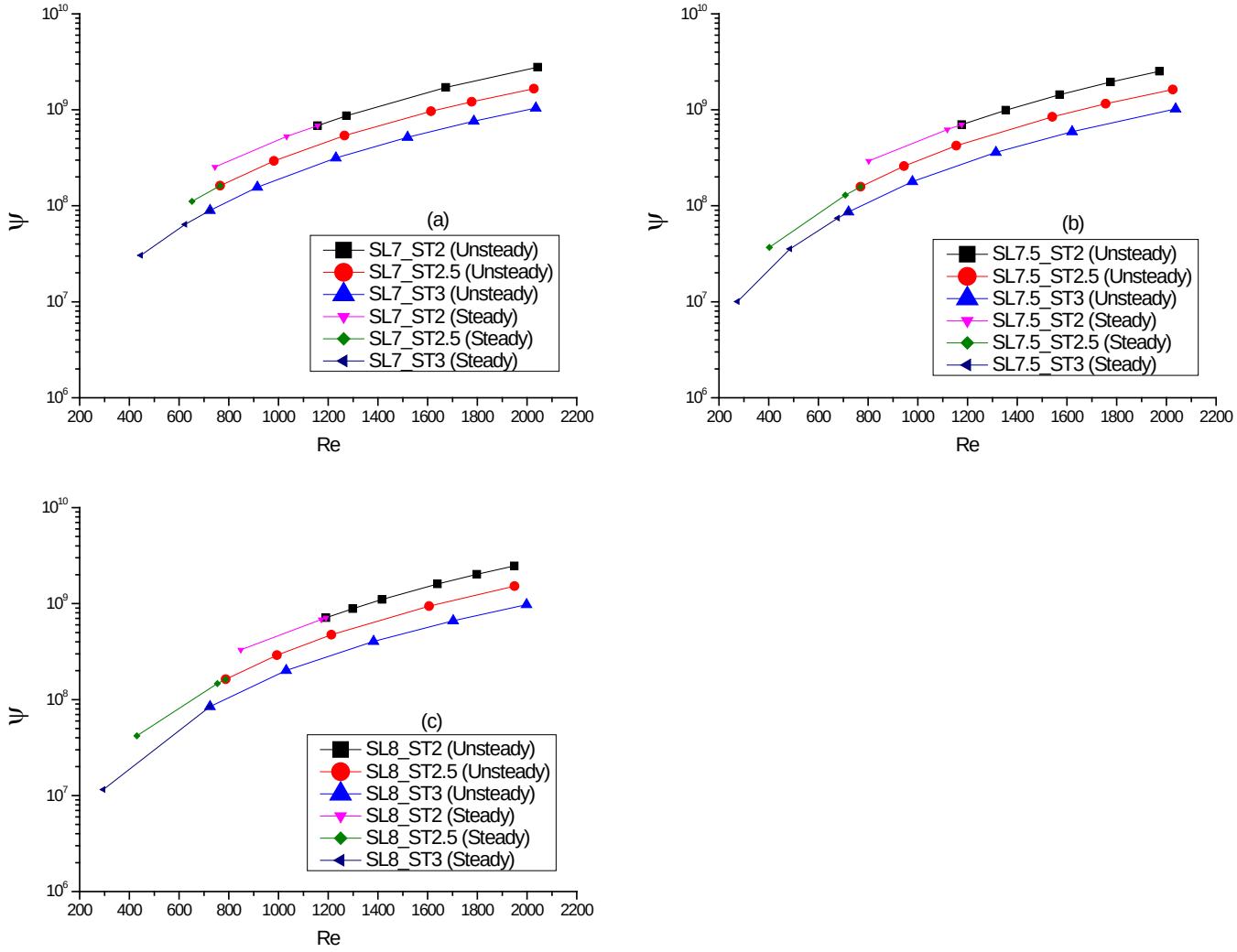

Figure 5-9. Non-dimensional pumping power (ψ) versus Reynolds number: constant S_L plots.

5.9 Discussion of Heat Transfer Results

The Nusselt number data appear in the tables above for both steady and unsteady cases. The general trend is for constant S_T , the *Nu* decreases slightly (on the order of 3%) with increasing S_L. However, for constant S_L, there is significant increase in *Nu* as S_T as increases. Figure 5-10 shows *Nu* versus *Re* for the unsteady SL7.5 cases. The plot is representative of the other two S_L values, as well. Comparing ST2 to ST3, a significant increase in *Nu* at all *Re* is observed. The ST2.5 case shows different behavior. It closely tracks the curve for ST3 data until $Re \approx 1200$, then is almost flat showing little increase in *Nu* with increasing *Re*.

Figure 5-11 shows *Nu* versus *Re* for unsteady, steady, and pseudo-steady cases for SL7.5_ST2.5 geometry. Re_{crit} lies at the intersection of the three plots. The steady data for $Re > Re_{crit}$ are pseudo-steady solutions. For $Re < Re_{crit}$, the solutions are true steady solutions and the curve is flat indicating very little rise in *Nu* with increasing *Re*. For $Re = Re_{crit}$ to $Re \approx 1500$, there is an approximate 65% increase in *Nu* with respect to pseudo-steady solutions. Recall that the pseudo-steady solutions are obtained with a modified unsteady code for which flow oscillations are prevented from occurring. The 65% difference in *Nu* for the unsteady and pseudo-steady curves therefore represents the effect of flow oscillations on Nusselt number. For $Re > 1500$, the *Nu* shows little change with increasing *Re*. Figure 5-11 is typical of the other domains as well except that for the SL7.5_ST2.5 geometry, the unsteady curve flattens out more quickly than for the other geometries.

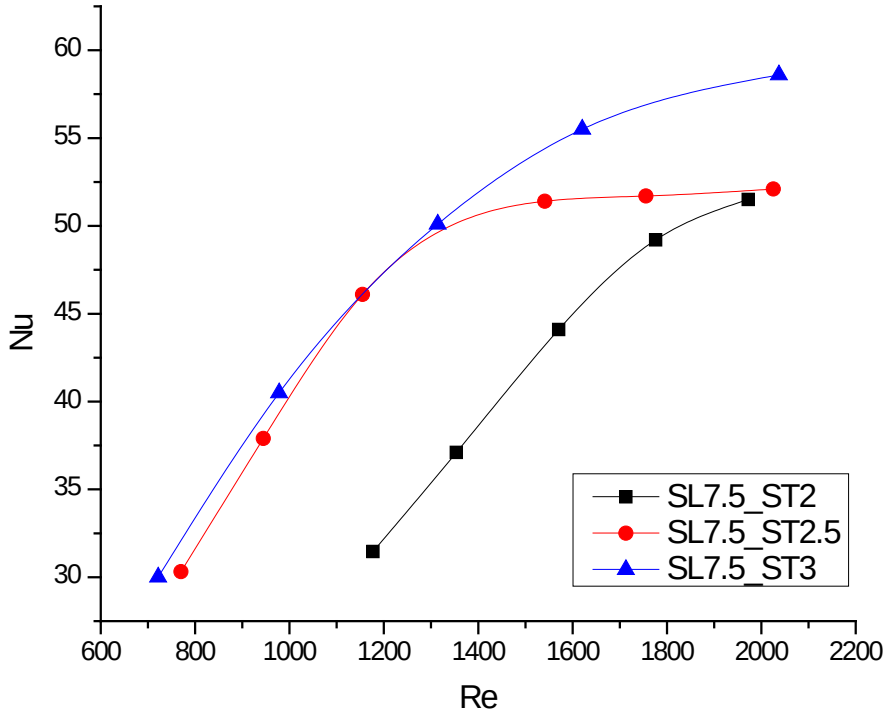

Figure 5-10. Nusselt number versus Reynolds number for unsteady SL7.5 cases.

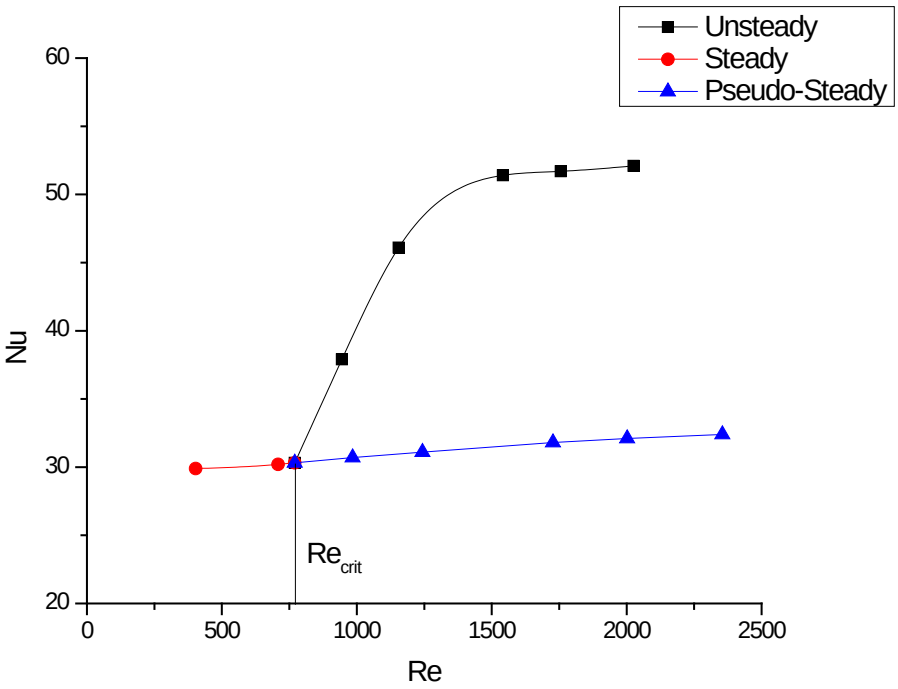

Figure 5-11. Nusselt number versus Reynolds number for SL7.5_ST2.5: unsteady and steady data.

5.10 Discussion of Combined Flow and Heat Transfer

As discussed above, non-dimensional pumping power (ψ) is used in the current work as an indication of cost of operation. The intended use of the flat tube heat exchanger devices considered in the current work is to transfer energy from one fluid to another. The purpose of the current work is to shed light upon which combination of geometry and operating conditions can produce the highest rate of heat transfer at the lowest cost. With these considerations in mind, a plot of ψ versus Nusselt number is a plot of cost versus benefit.

Figure 5-12 shows ψ versus Nusselt number on semi-log scales for all cases grouped by constant transverse spacing. In Figure 5-12, parts (a), (b), and (c) represent constant transverse spacing ST2, ST2.5, and ST3, respectively. The three plots for Figure 5-12 are very similar. Each shows a near-vertical section at low Reynolds numbers that corresponds to true steady flow. A vertical line on these plots indicates that an increase in pumping power is not accompanied by an increase in *Nu*. Essentially, there is no benefit for the added cost. This is followed by a section corresponding to unsteady, oscillatory flow which shows steady increase in *Nu* for the added cost of higher ψ. For the ST2.5 and ST3 plots, the plot indicates the beginning of another near-vertical section at the higher *Nu* values shown. This is more pronounced for the ST2.5 plot. This indicates that there is a *Re* range between Re_{crit} and another higher *Re* that the oscillatory flow demonstrates benefits by producing higher *Nu* for relatively modest increases in ψ. This will then be followed by a *Re* range where pumping power will

increase with little increase in *Nu*. Presumably, this region of the curve is a precursor to the turbulent flow regime.

Figure 5-13 shows ψ versus Nusselt number on semi-log scales for all cases grouped by constant longitudinal spacing. In Figure 5-13, parts (a), (b), and (c) represent constant longitudinal spacing SL7, SL7.5, and SL8, respectively. These plots show that for the geometries tested, the more compact ST2 geometries require more pumping power to deliver the same *Nu* as compared to the ST2.5 and ST3 geometries. As an example, for the SL7 cases at $Nu \approx 53$, the ST2 configuration ψ is 189% higher than for ST2.5 and 437% higher than for ST3. Similar ψ requirements are indicated for the SL2.5 and SL8 cases as well.

For one case, SL7.5_ST2.5, additional data were collected to show the shape of the ψ versus *Nu* curve at higher and at lower *Re* values. Figure 5-14 shows the plot of this data on semi-log scales similar to Figure 5-12 and Figure 5-13. The oscillatory unsteady data was extended to $Re = 2822$. Higher *Re* solutions were attempted, but the solutions diverged. Some steady *Re* data was also added at lower Reynolds numbers. The curve in Figure 5-14 shows four distinct regions. Region 1 shows that for very low Reynolds number flows, the flow is steady laminar flow and there is a positive slope on the curve indicating that as pumping power is increased, there is a corresponding increase in *Nu*. Region 2 is a near-vertical section that is steady flow at $Re < Re_{crit}$. In Region 2, there is little change in the *Nu* for the increase in ψ. Region 3 begins at the critical point and shows a steady increase in *Nu* for increased ψ as Reynolds number

increases. Region 4 shows an increase in the slope of the curve indicating more pumping power required for modest *Nu* gains. It is expected that with similar extensions of the data sets, the curves for the other eight domains would look similar to that of Figure 5-14.

Two additional figures show the steady and unsteady regions of Figure 5-14 separately on linear-linear scales. Figure 5-15 shows the two steady regions, while Figure 5-16 shows the two unsteady regions.

Figure 5-15 shows the near-vertical Region 2 clearly. In this steady-flow region, the Nusselt number shows an increase from 29.8 to 30.3 (1.7% increase) for a ten-fold increase in the required pumping power. Based on this data, operation in this steady-flow region should be avoided.

Figure 5-16 shows that in the first section of unsteady Region 3, the Nusselt number increases from 30.3 to 46.1 (52% increase) for 2.6 times increase in required pumping power. Operation in this region is desired because the flow oscillations produce higher Reynolds numbers for moderate increases in required pumping power.

Figure 5-16 also shows the near-vertical unsteady Region 4. In Region 4, the Nusselt number increases from 51.2 to 54.9 (7% increase) for a 4.5 times increase in required pumping power. Operating in this region, one sees an increase in Nusselt number, but at higher cost than seen in Region 3.

Based on the extended data for SL7.5_ST2.5, operation in Region 3 shown in Figure 5-14 or Figure 5-16 is most effective on a cost/benefit basis. This region begins at the critical point where oscillatory flow begins and extends to beginning of Region 4.

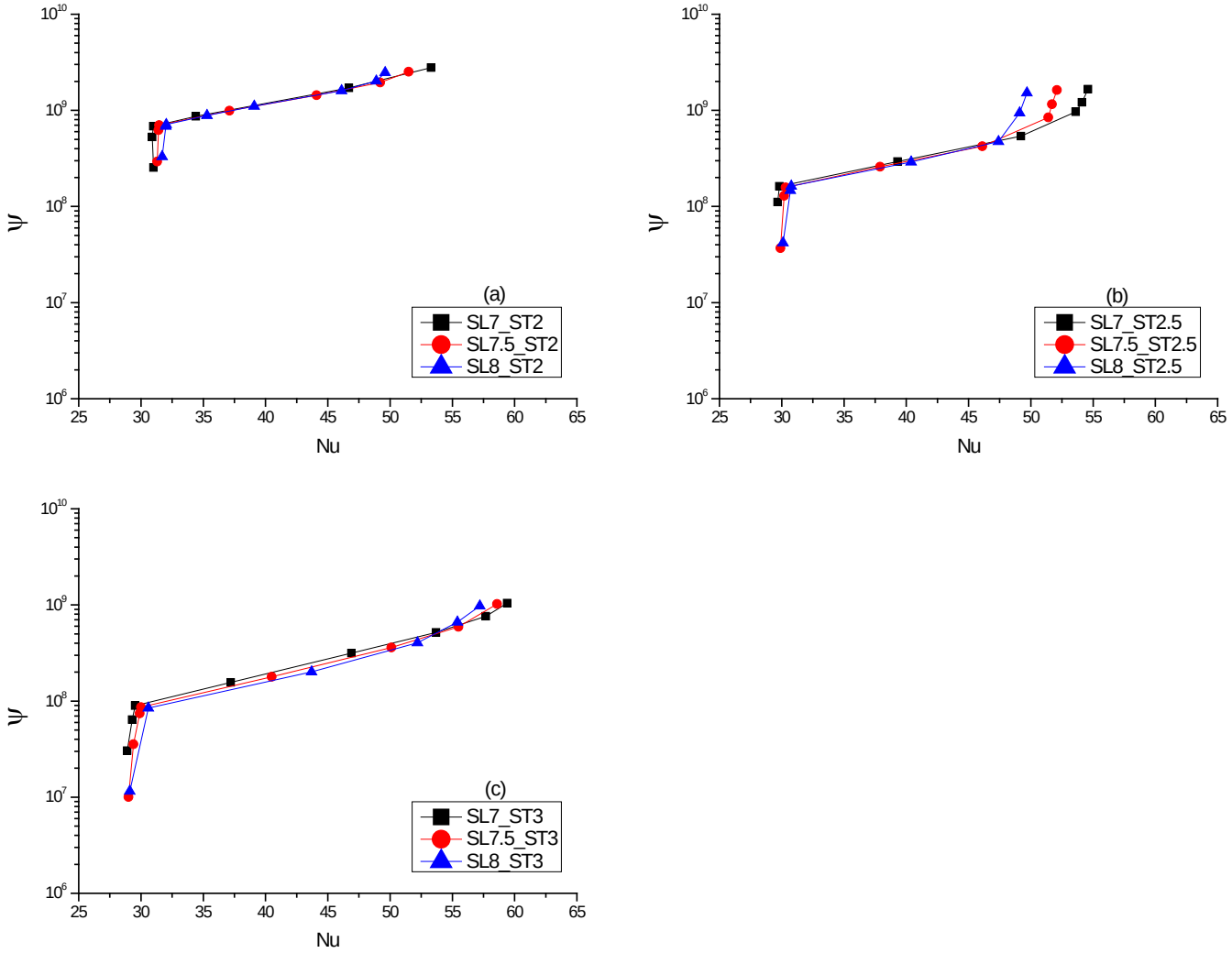

Figure 5-12. Non-dimensional pumping power (ψ) versus Nusselt number: constant S_T plots.

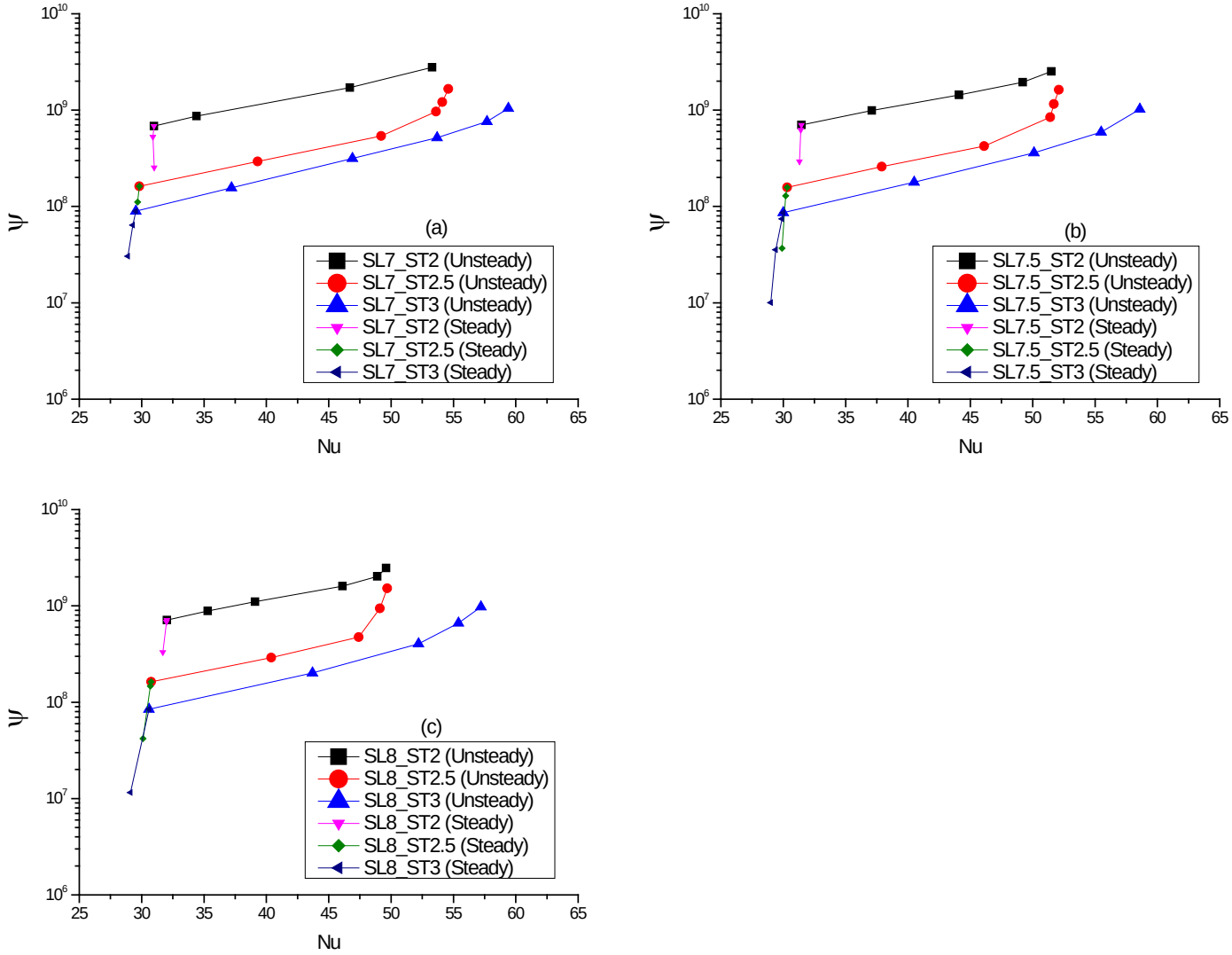

Figure 5-13. Non-dimensional pumping power (ψ) versus Nusselt number: constant S_L plots.

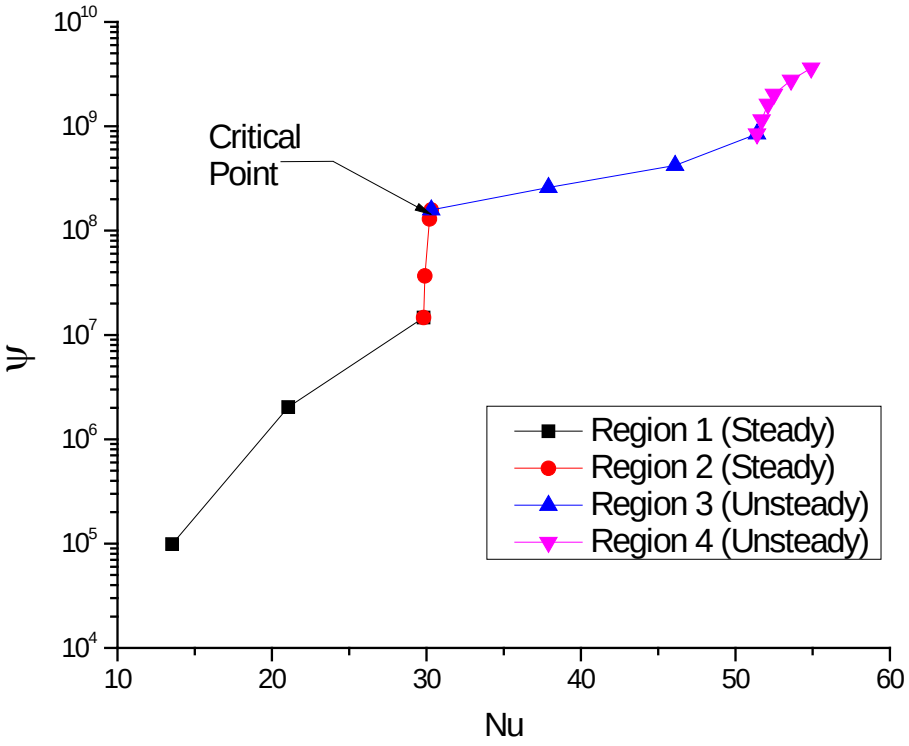

Figure 5-14. Non-dimensional pumping power (ψ) versus Nusselt number: SL7.5_ST2.5 (Extended).

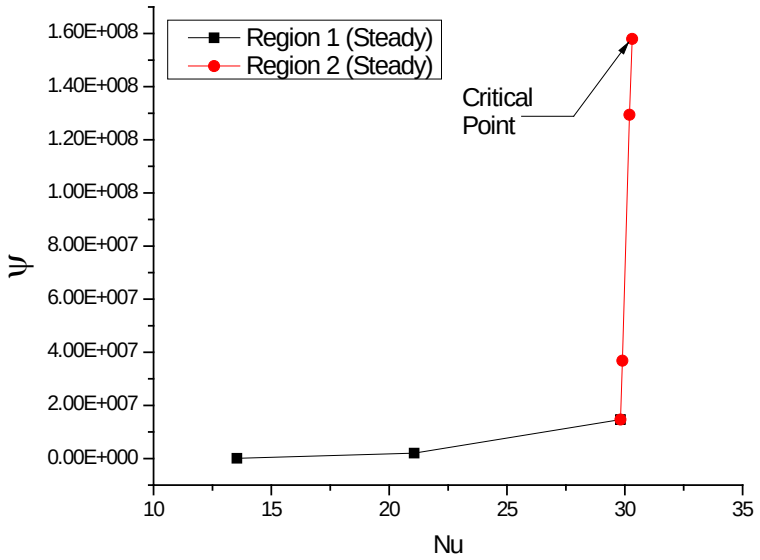

Figure 5-15. Non-dimensional pumping power (ψ) versus Nusselt Number: SL7.5_ST2.5 (steady only).

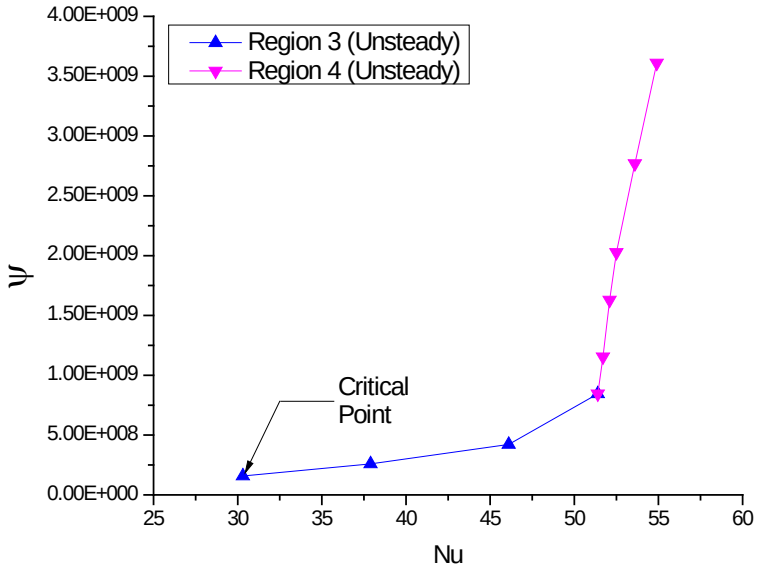

Figure 5-16. Non-dimensional pumping power (ψ) versus Nusselt Number: SL7.5_ST2.5 (unsteady only).

6. SUMMARY

Numerical simulations of flat tube heat exchanger devices operating in flow regimes in which self-sustained oscillations occur were performed. These unsteady flow regimes represent transition flow regimes between steady, laminar flow and fully turbulent flow for the domains studied. The oscillations observed were cyclic in that the values of flow parameters such as stream-wise or cross-stream velocity at a point varied with time in a repeating manner.

A computer code was developed to perform the numerical simulations. Spatial discretization was based upon a Control Volume Finite Element Method (CVFEM). Temporal discretization was based upon an ESDIRK, a semi-implicit Runge-Kutta method. Double Cyclic conditions were used to limit the numerical domains to one module.

Nine geometric domains representing flat tube heat exchanger devices were defined and tested over a range of Reynolds numbers. Three values of longitudinal tube spacing (S_L) and three values of transverse tube spacing (S_T) were used to define the nine domain geometries. A maximum Reynolds number (Re) of 2000 was established to keep the study well within the transition range. For each unique domain a critical Reynolds number (Re_{crit}) was found such that for $Re < Re_{crit}$ the flow was steady, laminar flow and for $Re > Re_{crit}$ the flow exhibited cyclic oscillations.

For each domain, numerical solutions for several cases of unsteady flow, steady flow, and pseudo-steady flow were obtained. The global pressure gradient (β) was chosen for each solution. For each unsteady solution, data were collected corresponding

to Reynolds number (*Re*), friction factor (*f*), Strouhal number (*Str*), normalized oscillation amplitude ($\overline{PTP}$), tube skin friction coefficient ($C_{D,skin}$), tube pressure drag coefficient ($C_{D,press}$), percent tube skin friction, percent tube pressure drag, non-dimensional pumping power (ψ) and Nusselt number (*Nu*). For each steady or pseudo-steady solution, data were collected for the same parameters except for Strouhal number (*Str*) and normalized oscillation amplitude ($\overline{PTP}$) as these two pertain only to unsteady flows.

There were several general trends in the data that were identified. First, the results showed little variation with changing longitudinal spacing (S_L), but significant variation with changes in the transverse spacing (S_T) for the cases studied. For oscillating cases for the same domain geometry, both the frequency of oscillation and the peak-to-peak magnitude of oscillation for primary variables *u*, *v*, $\hat{T}$, and $\hat{P}$ increased with increasing Reynolds number.

The frequency of oscillation for integrated skin friction and pressure drag was twice the frequency for the primary parameters. This is due to the fact that even though primary variables oscillate at the same frequency for all nodes in the domain, there are phase shifts in the oscillations from one location to another. Also, the sum of the integrated skin friction and pressure drag representing the time varying force on the tube also oscillates at a frequency twice that of the primary variables.

A method of estimating Re_{crit} was presented. The underlying assumption to this method is that Re_{crit} lies on both the unsteady and pseudo-steady *Re* versus β curves.

The critical Reynolds number was lower for larger values of the transverse spacing (S_T) meaning that the least compact geometry leads to destabilization of the flow at a lower Reynolds number for the cases studied.

The data indicate that flow oscillations are responsible for significant increases in Nusselt number compared to pseudo-steady solutions for the same Reynolds number. The results underscore the importance of identifying Re_{crit} prior to performing numerical analysis for domains such as these. For cases of interest where $Re<Re_{crit}$, steady analysis may be used and symmetry may be applied along the stream-wise centerline of the domain. However, for $Re>Re_{crit}$, unsteady analysis must be performed without imposing symmetry and the solution must be carried past the onset of oscillations to the point where the oscillations are cyclic in order to achieve accurate results. Large errors in predicted Nusselt number would occur if one used steady analysis for one of these unsteady cases.

The data for pumping power versus Nusselt number show four operating regions with differing characteristics. The results indicate that operation in Region 3 coinciding with self-sustained oscillations provides the highest Nusselt number for the smallest required pumping power. This data would provide good guidance for the design of a heat exchanger device based on the geometry studied.

6.1 Recommendations for Future Work

Recommendations for future work include extending the range of S_T for the current data set. In the current data, the greatest changes in parameter values followed changes in the transverse spacing. It is likely that at very high S_T, the flow may not

exhibit oscillations at all. It would be interesting to increase the range of S_T for one of the S_L values used in the current study.

The changes in the longitudinal spacing in the current work were too small to have much impact on the parameter values of interest. The gap between columns of tubes was varied from D_{min} to $2D_{min}$ but the length of the tube is $6D_{min}$. It would be interesting to check S_L values on the order of $2D_{min}$ to $6D_{min}$.

It would also be interesting to use a 3D turbulent code to extent the ψ versus Nu curves into turbulent region.

REFERENCES

[1] R. L. Webb and K. Ermis, Effect of Hydraulic Diameter on Condensation of R-134A in Flat, Extruded Aluminum Tubes, *Enhanced Heat Transfer*, vol. 8, pp. 77-90, 2001.

[2] A. Achaichia and T. A. Cowell, Heat Transfer and Pressure Drop Characteristics of Flat Tube and Louvered Plate Fin Surfaces, *Experimental Thermal and Fluid Science*, vol. 1, pp. 147-157, 1988.

[3] H. M. S. Bahaidarah, N. K. Anand, and H. C. Chen, A Numerical Study of Fluid Flow and Heat Transfer Over A Bank Of Flat Tubes, *Numer. Heat Transfer A*, vol. 48, pp. 359-385, 2005.

[4] H. M. S. Bahaidarah, M. Ijaz, and N. K. Anand, Numerical Study of Fluid Flow and Heat Transfer Over a Series of In-Line Noncircular Tubes Confined in a Parallel-Plate Channel, *Numer. Heat Transfer B*, vol. 50, pp. 97-119, 2006.

[5] T. L. Fullerton and N. K. Anand, Periodically Fully-Developed Flow and Heat Transfer Over Flat and Oval Tubes Using A Control Volume Finite-Element Method, *Numer. Heat Transfer A*, vol. 57, pp. 642-665, 2010.

[6] N. Benarji, C. Balaki, and S. P. Venkateshan, Unsteady Fluid Flow and Heat Transfer Over a Bank of Flat Tubes, *Heat Mass Transfer*, vol. 44, pp. 445-461, 2008.

[7] T. Adachi and H. Uehara, Linearstability Analysis of Flow in a Periodically Grooved Channel, *Int. J. Numer. Methods Fluids*, vol. 41, pp. 601-613, 2003.

[8] N. K. Ghaddar, K. Z. Korczak, B. B. Mikic, and A. T. Patera, Numerical Investigation of Incompressible Flow in Grooved Channels. Part 1. Stability and Self-Sustained Oscillations, *J. Fluid Mech.*, vol. 163, pp. 99-127, 1986.

[9] D. Majumdar and C. H. Amon, Heat and Momentum Transport in Self-Sustained Oscillatory Viscous Flows, *J. Heat Transfer*, vol. 114, pp. 866-873, 1992.

[10] C. H. Amon and B. B. Mikic, Spectral Element Simulations of Unsteady Forced Convective Heat Transfer: Application to Compact Heat Exchanger Geometries, *Numer. Heat Transfer*, vol. 19, pp. 1-19, 1991.

[11] D. Majumdar and C. H. Amon, Oscillatory Momentum Transport Mechanisms in Transitional Complex Geometry Flows, *J. Fluids Engineering*, vol. 119, pp. 29-35, 1997.

[12] C. H. Amon, D. Majumdar, C. V. Herman, F. Mayinger, B. B. Mikic, and D. P. Sekulic, Numerical and Experimental Studies of Self-Sustained Oscillatory Flows in Communicating Channels, *Intl J. Heat Mass Transfer*, vol. 35, no. 11, pp. 3115-3129, 1992.

[13] A. M. Guzman, M. P. Beiza, and P. F. Fischer, Transition Scenario of Periodic and Quasiperiodic Flow Bifuractions in Symmetric Communicating Channels, in *Proceedings of 5th Joint ASME/JSME Fluids Engineering Conference*, San Diego, California, 2007, pp. 1265-1272.

[14] L. W. Zhang, S. Balachandra, D. K. Tafti, and F. M. Najjar, Heat Transfer Enhancement Mechanisms in Inline and Staggered Parallel-Plate Fin Heat Exchangers, *Int. J. Heat Mass Transfer*, vol. 40, pp. 2307-2325, 1997.

[15] L. W. Zhang, D. K. Tafti, F. M. Najjar, and S. Balachandar, Computation of Flow and Heat Transfer in Parallel-Plate Fin Heat Exchangers on the CM-5: Effects of Flow Unsteadiness and Three-Dimensionality, *Int. J. Heat Mass Transfer*, vol. 40, no. 6, pp. 1325-1341, 1997.

[16] L. W. Zhang, S. Balachandar, and D. K. Tafti, Effects of Intrinsic Three Dimensionality on Heat Transfer and Friction Loss In a Periodic Array of Parallel Plates, *Numer. Heat Transfer A*, vol. 31, pp. 327-353, 1997.

[17] S. Balachandar and S. J. Parker, Onset of Vortex Shedding in an Inline and Staggered Array of Rectangular Cylinders, *Physics of Fluids*, vol. 14, no. 10, pp. 3714-3732, 2002.

[18] C. Prakash, A Finite Element Method for Predicting Flow Through Ducts With Arbitrary Cross Sections, Ph.D. thesis, University of Minnesota, Minneapolis, 1981.

[19] C. Prakash and S. V. Patankar, A Control Volume-Based Finite-Element Method for Solving the Navier-Stokes Equations Using Equal-Order Velocity-Pressure Interpolation, *Numer. Heat Transfer*, vol. 8, pp. 259-280, 1985.

[20] H. J. Saabas, A Control Volume Finite Element Method for Three-Dimensional, Incompressible, Viscous Fluid Flow, Ph.D. thesis, McGill University, Montreal, Canada, 1991.

[21] H. J. Saabas and B. R. Baliga, Colocated Equal-Order Control-Volume Finite-Element Method for Multidimensional, Incompressible, Fluid Flow-Part I: Formulation, *Numer. Heat Transfer B*, vol. 26, pp. 381-407, 1994.

[22] H. J. Saabas and B. R. Baliga, Colocated Equal-Order Control-Volume Finite-Element Method for Multidimensional, Incompressible, Fluid Flow-PartII: Verification, *Numer. Heat Transfer B*, vol. 26, pp. 409-424, 1994.

[23] S. R. Husain, Extensions of the Control Volume Based Finite Element Method for Fluid Flow Problems, Ph.D. dissertation, Texas A&M University, College Station, 1987.

[24] S. V. Patankar, *Numerical Heat Transfer and Fluid Flow*, McGraw Hill, New York, 1980.

[25] M. Ijaz, Implicit Runge-Kutta Methods to Simulate Unsteady Incompressible Flows, Ph.D. dissertation, Texas A&M University, College Station, 2007.

[26] S. V. Patankar, C. H. Liu, and E. M. Sparrow, Fully Developed Flow and Heat Transfer in Ducts Having Streamwise-Periodic Variations of Cross-Sectional Area, *ASME J. Heat Transfer*, vol. 99, pp. 180-186, 1977.

[27] S. H. Kim and N. K. Anand, Periodically Fully Developed Flow in Channels with Conducting Blockages, *J. Thermophysics*, vol. 6, no. 1, pp. 91-97, 1992.

[28] G. E. Karniadakis, B. B. Mikic, and A. T. Patera, Minimum-Dissipation Transport Enhancement by Flow Destabilization: Reynolds' Analogy Revisited, *J. Fluid Mech.*, vol. 192, pp. 365-391, 1988.

[29] D. Kundu, A. Haji-Sheikh, and D. Y. S. Lou, Pressure and Heat Transfer in Cross Flow over Cylinders between Two Parallel Plates, *Numer. Heat Transfer A*, vol. 19, pp. 343-360, 1991.

[30] T. L. Fullerton and N. K. Anand, An Alternative Approach to Study Periodically Fully-Developed Flow and Heat Transfer Problems Subject to Isothermal Heating Conditions, *Int. J. Engineering Science*, vol. 48, pp. 1253-1262, 2010.

[31] K. M. Kelkar and S. V. Patankar, Numerical Prediction of Flow and Heat Transfer in a Parallel Plate Channel with Staggered Fins, *ASME J. Heat Transfer*, vol. 109, pp. 25-30, 1987.

[32] N. B. Santos and M. J. S. De Lemos, Flow and Heat Transfer in a Parallel-Plate Channel with Porous and Solid Baffles, *Numer. Heat Transfer A*, vol. 49, pp. 471-494, 2006.

[33] B. W. Webb and S. Ramadhyani, Conjugate Heat Transfer in a Channel with Staggered Ribs, *Int. J. Heat Mass Transfer*, vol. 28, no. 9, pp. 1679-1687, 1985.

[34] C. Nonino and G. Comini, Finite-Element Analysis of Convection Problems in Spatially Periodic Domains, *Numer. Heat Transfer B*, vol. 34, pp. 361-378, 1998.

[35] C. H. Cheng and W. H. Huang, Numerical Prediction for Laminar Forced Convection in Parallel-Plate Channels with Transverse Fin Arrays, *Int. J. Heat Mass Transfer*, vol. 34, no. 11, pp. 2739-2749, 1991.

APPENDIX A*

APPENDIX A presents the entire text of Fullerton and Anand [5].

*Reprinted with permission from "Periodically Fully-Developed Flow and Heat Transfer over Flat and Oval Tubes Using a Control Volume Finite-Element Method" by T.L. Fullerton and N.K. Anand, 2010. *Numerical Heat Transfer, Part A*, vol. 57, pp. 642-665, Copyright 2010 by Taylor & Francis Group, LLC.

Numerical Heat Transfer, Part A, 57: 642–665, 2010

ISSN: 1040-7782 print/1521-0634 online
DOI: 10.1080/10407781003744888

Taylor & Francis
Taylor & Francis Group

PERIODICALLY FULLY-DEVELOPED FLOW AND HEAT TRANSFER OVER FLAT AND OVAL TUBES USING A CONTROL VOLUME FINITE-ELEMENT METHOD

T. L. Fullerton and N. K. Anand
Department of Mechanical Engineering, Texas A&M University, College Station, Texas, USA

A Control Volume Finite-Element Method in conjunction with imposed periodically fully-developed flow conditions was used to perform a two-dimensional, laminar, steady-flow numerical study comparing the performance of a flat tube and an oval tube to that of a round tube in a simulated heat exchanger device for the case of specified heat flux along the tube walls. The Reynolds number range for the study was 50 to 350. Fluids of Prandtl number 0.7 and 7.0 were considered. For the cases studied, the heat transfer enhancement ratio was less than one indicating that the round tube outperformed both the flat tube and the oval tube based on heat transfer considerations alone. However, for all cases studied, the heat transfer performance ratio was greater than one indicating that if both heat transfer performance and required pumping power are considered, both the flat tube and oval tube outperformed the round tube.

1. INTRODUCTION

Tube-in-cross-flow heat exchangers have applications for a myriad of products and engineering processes. The effects of tube shape and geometric arrangement on the flow field and heat transfer performance of these devices have been studied using various experimental, numerical, and analytical techniques. Studies have been performed with various tube shapes such as rectangular, triangular, oval, and flat with performance usually compared to the performance of round tubes under similar conditions. These studies present as results the flow field and temperature field, as well as quantities such as friction factor and Nusselt number. Commonly, such heat exchanger devices exhibit regular geometric spacing of tubes leading to the development of periodically fully-developed flow (PFD) conditions at some distance from the inlet. For such devices, the majority of tubes lie in flow modules exhibiting PFD conditions. Therefore, the performance of a given tube-shape and geometric spacing combination is usually characterized by the performance in a flow module exhibiting PFD conditions. The main objective of the current work is to demonstrate that a control volume finite-element method (CVFEM) together with specified PFD

Received 4 January 2010; accepted 17 February 2010.
This research was supported by the *James and Ada Forsyth Professorship* endowment funds.
Address correspondence to N. K. Anand, Department of Mechanical Engineering, Texas A&M University, College Station, TX 77843, USA. E-mail: nkanand@tamu.edu

NOMENCLATURE

a	coefficients in discretization equations	Re	Reynolds number
A, B, C	coefficients in interpolation function	T	temperature, °K
b	generalized source term	$\hat{T}$	local temperature variation, °K
c_p	specific heat, J/kg°K	u	streamwise velocity, m/s
CV	control volume	v	cross-stream velocity, m/s
D	diameter of the round tube, m	w	streamwise length of the flat tube
D_h	hydraulic diameter, m	x,y	global coordinates
f	friction factor	X,Y	local coordinates
H	channel height, m	β	global pressure drop per module
k	thermal conductivity, W/m°K	γ	global temperature rise per module
l	height of the flat tube, m	Γ	diffusion coefficient
L	length of the periodically fully-developed module, m	ΔP	pressure drop per module, N/m^2
		λ	coefficient in integrated flux expression
$\dot{m}$	mass flow rate through the PFD module, Kg/s	μ	dynamic viscosity, $N{\cdot}s/m^2$
		ρ	density, Kg/m^3
Nu	Nusselt number	ϕ	general transported scalar variable
$\overline{\text{Nu}}$	average Nusselt number (change in enthalpy)	Φ	integrated flux
		χ	general field variable
Nu^+	heat transfer enhancement ratio		
Nu^*	heat transfer performance ratio	**Subscripts**	
P	pressure, N/m^2	p	typical node
Pe	element Peclet number	nb	neighborhood nodes
Pr	Prandtl number	min	minimum
$\hat{P}$	local pressure variation	max	maximum
q''	heat flux, W/m^2	s	surface
Q	total heat flux added per module, J	b	bulk

conditions may be used to study fluid flow and heat transfer in heat exchanger devices with geometrically repeated modules. Imposing PFD conditions allows the computational domain of interest to be limited to one module exhibiting periodically fully-developed flow; thus, drastically decreasing mesh size and solution time. In addition, heat transfer and flow field data for a PFD module establish the lower bounds for heat transfer coefficient and friction factor, thus providing useful design information.

For the current work, each two-dimensional computational domain example consists of a single tube confined between two insulated parallel plates. Constant heat flux is specified on the surface of the tube. Three tube shapes are considered: round, flat, and oval. Figure 1 shows the geometry of the computational domains considered in this study. Once the diameter of the round tube was established, the shapes of the flat and oval tubes were chosen such that the perimeter, and therefore the heat transfer area, would be equal to that of the round tube. Steady, laminar, two-dimensional solutions were obtained for a Reynolds number (Re) range of 50–350 for each of the three computational domains for two different fluids of Prandtl number (Pr), 0.7 and 7.0. The friction factor and local Nusselt number (Nu) distribution along the tube surfaces were used as bases for comparison between the three configurations. Two additional parameters, the heat transfer enhancement ratio and the heat transfer performance ratio, were also used as bases for comparison.

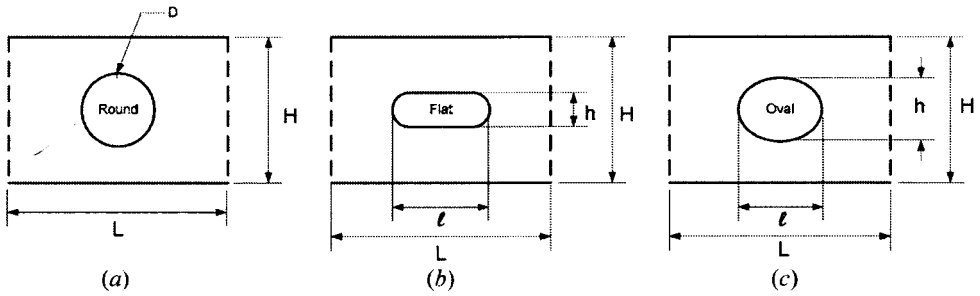

Figure 1. Computational domain geometries: (*a*) round tube; (*b*) flat tube; and (*c*) oval tube. Flow direction is left to right for each domain geometry.

We will present the general characteristics of the CVFEM used in this work followed by a discussion of PFD conditions. Code validation data will be presented along with grid independence results. Finally, we will compare the flow and heat transfer characteristics for the flat and oval tubes versus the round tube for the Re range described above.

2. CONTROL VOLUME FINITE-ELEMENT METHOD

For numerical solution of flow and heat transfer problems in general, the goal is to first solve for streamwise velocity (u), cross-stream velocity (v), pressure (P), and temperature (T) at discrete locations in the domain of interest. Once the u, v, P, and T fields have been determined, quantities of interest such as friction factor and Nusselt number may be calculated. For the current work, a CVFEM was used to solve the Navier-Stokes equations for two-dimensional (2-D), laminar, constant property, incompressible, steady-flow cases.

CVFEMs combine features of both finite element (FE) methods and finite volume (FV) methods. Like FE methods, the domain is discretized into regions called elements to which material properties are assigned and within which interpolation functions are defined which describe the variation of velocity, pressure, and temperature within an element. Like FV methods, control volumes, (CVs) are defined to which conservation equations in integral form are applied, resulting in sets of algebraic equations for the domain which may be solved for the u, v, P, and T fields.

There are several 2-D CVFEMs described in the literature. References [1–11] describe various formulations for 2-D CVFEMs using both triangular- and quadrilateral-shaped elements. Comparing and contrasting the various versions is beyond the scope of the current work. The basic method for the particular CVFEM employed in the current work is the colocated, equal-order, triangular-element method described by Prakash [1, 2]. Additional material directly influencing the current work may be found in Sabaas [3–5] and Husain [6]. No originality is claimed here with respect to the CVFEM method.

For 2-D CVFEMs in general, the computational domain is first discretized as a set of triangular elements which completely fill the domain without overlap. The vertices of these triangles are called nodes and are the locations at which u, v, P,

and T are calculated. For the specific method used, each element is divided into three equal-area sub-regions by defining links from the element centroid to the midpoint of each of the three sides, as shown in Figure 2*a*. Each sub-region is associated with one of the element's three nodes. The fact that the domain is meshed with triangles makes this method a good candidate for the solution of tube-in-cross-flow problems in that the irregular domain geometry associated with various tube shapes may be meshed to desired accuracy using triangles. Also, the variables u, v, P, and T may remain in their native (x, y) coordinates without coordinate transformation. Other methods require the transformation of the domain geometry to generalized coordinates to solve problems with irregular geometry. One description of this method may be found in Bahaidarah et al. [12].

The domain is further discretized as a set of polygonal CVs such that each node in the domain has an associated CV. The set of CVs defined in this manner completely fills the domain without overlap. The CV associated with a given node is formed from sub-regions of the elements that share that particular node. The element links of contributing elements form the boundary of the CV for internal CVs, as shown in Figure 2*b*. For boundary CVs, the boundary is formed from a combination of element links and segments of the domain boundary, as shown in Figure 2*c*. Integral forms of the various conservation equations are applied to the CVs resulting in four sets of algebraic equations, one set for each of the unknown field variables of interest: u, v, P, and T. If the general variable χ represents u, v, P, or T, then the various conservation equations for the CV associated with Node P may be written in the following form:

$$a_P \chi_P + \sum_{nb} a_{nb} \chi_{nb} = b_P \tag{1}$$

The set of all such equations for all CVs in the domain are solved simultaneously using an iterative solution technique based on the SIMPLER algorithm [13].

Applying integral forms of the conservation equations to a given CV involves determining expressions for the integrated flux of x-momentum, y-momentum, energy, and mass across the element links that form the CV boundary. Boundary CVs are special cases involving integrated flux across segments of the domain

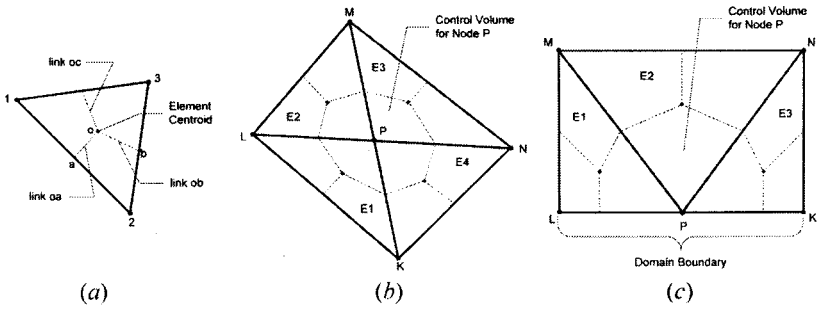

Figure 2. Element and control volume geometry: (*a*) typical element; (*b*) internal CV formed from four elements; and (*c*) boundary CV.

boundary itself. The integration along the boundary of a particular CV is performed piece-wise by first calculating the integrated flux across each element link for the entire set of elements and then assembling the appropriate expressions for the set of links that form the boundary of a particular CV.

To perform the integrated flux calculations across an element link, expressions for u- and v-velocity, temperature, and the spatial gradients of pressure are required at points along the link. Once these expressions are known, Simpson's Rule or some other integration technique may be applied to derive an expression for the integrated flux. Interpolation functions are defined to provide the distribution of velocity, pressure, and temperature within each element. For the general transported scalar variable ϕ representing streamwise velocity (u), cross-stream velocity (v), or temperature (T) (but not pressure (P)), the interpolation function takes the following exponential form:

$$\begin{aligned}
&\phi(X, Y) = AZ(X) + BY + C \\
&\text{where } Z(X) = \frac{\Gamma}{\rho U_{\text{avg}}}\left\{\exp\left[\text{Pe}\frac{(X - X_{\max})}{(X_{\max} - X_{\min})}\right] - 1\right\} \\
&\text{Pe} = \frac{\rho U_{\text{avg}}(X_{\max} - X_{\min})}{\Gamma} \\
&X_{\max} = \max(X_1, X_2, X_3) \\
&X_{\min} = \min(X_1, X_2, X_3)
\end{aligned} \tag{2}$$

In Eq. (2), ρ and Γ are the density and diffusion coefficient of the fluid, respectively. Pe is the element Peclet number. The interpolation function is defined in an element-local coordinate system (X, Y) such that the X-axis is aligned with the average flow direction within the element, the Y-axis direction is determined by the right-hand rule, and the origin is located at the element centroid. The interpolation function is exponential along the X direction and linear along the Y direction. In this way, the method takes into account the local flow direction within the element during flux calculations, thus minimizing false diffusion. $X_{\max}$ and $X_{\min}$ are the maximum and minimum, respectively, of the X coordinate values at the element's three nodes as specified in the element-local coordinate system.

The coefficients A, B, and C in Eq. (2) are not numerical constants. Rather, they are expressions in terms of the unknown values of ϕ at the element's three nodes. The expressions for A, B, and C are determined by assuming that Eq. (2) is valid at each of the element's three nodes. Eq. (2) therefore provides an expression for ϕ at a point (X, Y) within the element in terms of the unknown values of ϕ at the element's nodes. If one chooses to use Simpson's One-Third Rule for the integration of flux along a link, the expressions for ϕ at the two endpoints and at the midpoint of each link may be used to determine the final expression for the integrated flux of ϕ across the link in terms of the unknown values of ϕ at the element's three nodes. The integrated flux across an element link (Φ_{link}) may be represented as follows:

$$\Phi_{\text{link}} = \lambda_i \phi_i \qquad i = 1, 2, 3 \tag{3}$$

where ϕ_i represents the unknown value of ϕ at node i, and λ_i represents a numerical coefficient.

After the expressions for integrated flux in the form of Eq. (3) are obtained for the element links, an assembly process is used to combine the expressions for all links forming the boundary of a given CV. The result is an expression of the form of Eq. (1), representing conservation of x- or y-momentum or conservation of energy.

Pressure is not a transported scalar, so the method described above is not directly applicable. A linear interpolation function is used for pressure within an element along with the conservation of mass equation. Once again, the flux integrations are performed on an element basis and the resulting expressions assembled for a CV. The result is an equation of the form of Eq. (1) representing conservation of mass for CV_P in terms of the unknown pressure values at Node P and at each of the neighbor nodes.

Typical boundary conditions for flow problems are specified u- and v-velocity at the domain inlet, and zero u- and v-velocity at solid boundaries. For heat transfer problems, either temperature (T) or heat flux (q'') is specified along specified boundaries. For boundary CVs, the integrated flux of a variable across the domain boundary is added to the expression in the form of Eq. (1). The boundary conditions are known numerically, so this process modifies the general source term b_P in Eq. (1).

As stated earlier, conservation equations are assembled for each CV for each field variable of interest (u, v, P, and T). The resulting sets of equations are solved iteratively using a combination of the line-by-line procedure and the tridiagonal matrix algorithm (TDMA). The order of solution is determined by the SIMPLER algorithm.

The above summarizes the characteristics and procedures associated with the basic CVFEM used in the current work. We will now discuss periodically fully-developed flow conditions and how to implement these conditions using a CVFEM.

3. PERIODICALLY FULLY-DEVELOPED FLOW (PFD)

Mathematical formulation of PFD and heat transfer is well established and can be found in Patankar et al. [14] and Kim and Anand [15]. In the discussion to follow, x represents the streamwise direction, y represents the cross-stream direction, and L represents the length of the module.

In a periodically fully-developed flow domain, velocity profiles in the streamwise direction repeat themselves periodically ($u(x,\ y) = u(x+L,\ y) = u(x+2L,\ y)\ldots$ and $v(x,\ y) = v(x+L,\ y) = v(x+2L,\ y)\ldots$), and pressure drop per module length ($\beta \equiv \frac{P(x,y)-P(x+L,y)}{L}$) remains constant. Pressure in a PFD module can be represented as a combination of global pressure drop per module and local pressure variation ($P(x,y) = -\beta x + \widehat{P}(x,y)$). While pressure does not repeat with periodicity, the local pressure variation does ($\widehat{P}(x,y) = \widehat{P}(x+L,y) = \widehat{P}(x+2L,y)\ldots$). Representing pressure in terms of global pressure drop per module and local pressure variation in the Navier-Stokes equations, we get the following expressions for conservation of x- and y-momentum:

X - momentum

$$\rho\left(u\frac{\partial u}{\partial x} + v\frac{\partial v}{\partial y}\right) = \beta - \frac{\partial \widehat{P}}{\partial x} + \frac{\partial}{\partial x}\left(\mu\frac{\partial u}{\partial x}\right) + \frac{\partial}{\partial y}\left(\mu\frac{\partial u}{\partial y}\right) \tag{4}$$

Y-momentum

$$\rho\left(u\frac{\partial v}{\partial x}+v\frac{\partial u}{\partial y}\right)=-\frac{\partial \widehat{P}}{\partial y}+\frac{\partial}{\partial x}\left(\mu\frac{\partial v}{\partial x}\right)+\frac{\partial}{\partial y}\left(\mu\frac{\partial v}{\partial y}\right) \tag{5}$$

Both the x-momentum and y-momentum equations, Eqs. (4) and (5), respectively, are written in terms of the spatial derivatives of the locally-varying pressure component $\widehat{P}$. The spatial derivatives of pressure P do not appear explicitly in the equations. The x-momentum equation, Eq. (4), includes a β term representing the global pressure gradient in the streamwise direction for the module.

For the case of specified wall heat flux, the temperature values do not repeat module-to-module for neighboring PFD modules. Rather, the temperature differences repeat from module to module ($[T(x+L,\ y)-T(x,\ y)]=[T(x+2L,\ y)-T(x+L,\ y)]\ldots$). Thus, we may define a global temperature gradient γ in the streamwise direction for a PFD module as $\gamma\equiv\frac{T(x+L,y)-T(x,y)}{L}$. The global temperature gradient γ for a PFD module of length L may be calculated by performing a global energy balance on a PFD module as

$$\gamma=\frac{Q}{\dot{m}c_pL} \tag{6}$$

We can express the temperature at any point $(x,\ y)$ in the domain in terms of a global component involving γ and a locally varying component $\widehat{T}$ as $T(x,y)=\gamma x+\widehat{T}(x,y)$. The locally varying component $\widehat{T}$ is periodic in the streamwise direction ($\widehat{T}(x,y)=\widehat{T}(x+L,y)=\widehat{T}(x+2L,y)\ldots$). Substituting for $\widehat{T}(x,y)$ in terms of the global temperature rise and local variation components into the differential form of the conservation of energy equation for 2-D, steady, laminar flows, we arrive at a form involving γ and $\widehat{T}$.

Energy equation

$$\rho c_p\left(u\frac{\partial \widehat{T}}{\partial x}+v\frac{\partial \widehat{T}}{\partial y}\right)=\frac{\partial}{\partial x}\left(k\frac{\partial \widehat{T}}{\partial x}\right)+\frac{\partial}{\partial y}\left(k\frac{\partial \widehat{T}}{\partial y}\right)-\rho c_p\gamma u+\frac{\partial}{\partial x}(k\gamma) \tag{7}$$

The term $-\rho c_p\gamma u$ is an added source term involving the global temperature gradient for the PFD module. The second added source term $\frac{\partial}{\partial x}(k\gamma)$ is identically zero if the thermal conductivity k is constant throughout the domain. This second source term is important for domains including conducting solids such that the thermal conductivity for the solid differs from the thermal conductivity for the fluid [15]. For the current work, the second source term may be ignored. It should be noted that temperature T does not appear explicitly in Eq. (7).

A CVFEM code to implement the above conditions was developed. Rather than solving for $u,\ v,\ P$, and T, the PFD version of the code provides the solution for $u,\ v,\ \widehat{P}$, and $\widehat{T}$ for a single PFD module. The PFD code is based on an existing code which implements the standard CVFEM algorithms described above. The required code modifications include the addition of the source terms for the momentum and energy equations as explained above, and the implementation of PFD boundary conditions in the streamwise direction and no-slip conditions in the

transverse direction. The cyclic tridiagonal matrix algorithm (CTDMA) is used in the iterative solver when operating on rows of nodes aligned in the streamwise direction. TDMA is used on columns of nodes aligned in the cross-stream direction as for the standard CVFEM code.

Solution for a PFD module involves first specifying a value of β and solving the flow problem for u, v, and $\widehat{P}$. Next, the flow solution is used to calculate $\dot{m}$ for the domain and the specified heat flux is used to calculate Q. Eq. (6) may then be used to calculate γ. The solution process concludes with the solution for the $\widehat{T}$ field. Note that for the PFD solution, β is specified rather than velocity. Because of this, Reynolds numbers cannot be explicitly specified.

Friction Factor for PFD Solution

We are interested in calculating the friction factor and Nusselt number for the resulting flow and temperature fields. However, with the PFD code, we do not actually solve for pressure or temperature. Rather, we solve for the locally varying components $\widehat{P}$ and $\widehat{T}$ subject to a specified value of β. We must therefore define these quantities in terms of β and $\widehat{T}$.

The friction factor (f) may be defined as follows:

$$f \equiv \frac{\Delta P}{\rho \bar{u}_{\text{inlet}}^2} \tag{8}$$

The inlet average velocity $\bar{u}_{\text{inlet}}$ may be calculated by standard methods. The module pressure drop ΔP may be calculated in terms of the specified value of β and the module length L as $\Delta P = \beta L$. The friction factor for a PFD module may thus be calculated in terms of β as follows:

$$f = \frac{\beta L}{\rho \bar{u}_{\text{inlet}}^2} \tag{9}$$

It should be noted that f is often defined with a factor of $1/2$ in the denominator. The definition of f in Eq. (9) is for compatibility with Kundu et al. [16] and Bahaidarah et al. [12].

Bulk Temperature and Nusselt Number for PFD Solution

Calculating the Nusselt number requires calculating the bulk temperature at cross-stream sections of the domain. Because these flows may exhibit recirculation, the definition of bulk temperature is modified to include the absolute value of velocity rather than simply the velocity itself. For the case of PFD flow with specified surface heat flux, the solution process yields the $\widehat{T}$ field rather than the T field. Therefore, the fluctuating component of the bulk temperature $\widehat{T}_b$ is defined in terms of $\widehat{T}$ rather than in terms of T.

$$\widehat{T}_b(x) \equiv \frac{\int_y \widehat{T}(x,y)|u(x,y)|dy}{\int_y |u(x,y)|dy} \tag{10}$$

The Nusselt number is defined as follows.

$$\mathrm{Nu}(x) \equiv \frac{q'' D_h}{\left[\widehat{T}_s(x) - \widehat{T}_b(x)\right] k} \tag{11}$$

For the current work, the hydraulic diameter D_h is taken to be the channel height H. It can be shown that Nu defined in Eq. (11) in terms of fluctuating temperatures $\widehat{T}_s$ and $\widehat{T}_b$, is directly comparable to the standard definition in terms of actual temperatures T_s and T_b.

4. CODE VALIDATION

A developing flow (non-PFD) CVFEM code was used to solve standard validation problems such as the driven cavity, backward-facing step, and Poiseuille flow. Results for the flow field and for heat transfer performance compared well with published numerical or analytical data. However, these problems do not involve irregular geometry such as the tube-in-cross-flow problem.

For validation with tubes in cross flow, the developing flow (DF) CVFEM code was used to solve the problem posed by Kundu et al. [16] and referenced by Bahaidarah et al. [12]. Figure 3 shows the domain of interest consisting of five regularly-spaced round tubes of diameter D confined between parallel plates separated by a distance H. Each tube and its surrounding fluid comprise a heat exchange module (HEM) of length L. An entry section of length L and an exit section of length $3L$ are included as part of the domain. Values for D, H, and L were chosen such that $L/D = 3$ and $H/D = 2$. The surface of the tubes and the confining walls were subject to the same specified wall temperature. For Re between 50 and 200, both the flow field and temperature field approach PFD flow in HEM #4. The Reynolds number is defined using the channel height H as the hydraulic diameter as $\mathrm{Re} = \frac{\rho \bar{u}_{\mathrm{inlet}} H}{\mu}$. Developing flow and heat transfer were studied for $\mathrm{Re} = 50$ and $\mathrm{Re} = 200$ and the average Nusselt number ($\overline{\mathrm{Nu}}$) for each HEM that was calculated. For this problem, $\overline{\mathrm{Nu}}$ is the normalized change of enthalpy from the inlet to the exit of each HEM. As the flow and temperature approach PFD flow conditions, $\overline{\mathrm{Nu}}$ converges toward a constant value for a given Reynolds number.

Table 1 shows the results from Kundu et al. [16], Bahaidarah et al. [12], and from the current work. Table 1 shows good agreement with the previously published $\overline{\mathrm{Nu}}$ results for this particular tube-in-cross-flow problem.

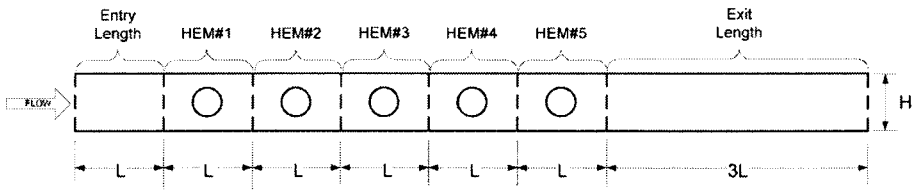

Figure 3. Computational domain for developing flow test case.

Table 1. Average nusselt numbers

	HEM #2	HEM #3	HEM #3
Re = 50			
Kundu et al. [16]	9.4	9.4	9.8
Bahaidarah et al. [12]	9.23	9.23	9.23
Current work	9.24	9.24	9.24
Re = 200			
Kundu et al. [16]	12.5	12.6	12.8
Bahaidarah et al. [12]	12.44	12.43	12.42
Current work	12.50	12.46	12.45

A separate version of the CVFEM code was developed to implement PFD boundary conditions. The first validation effort for this code was to solve fully-developed Poiseiulle flow. A computational domain was defined consisting of parallel plates separated by a distance H subjected to specified heat flux. Several meshes of increasing node density for the domain were used to solve the flow field and temperature field and compute the local Nusselt number along the plate using Eq. (11). As the mesh density increased, the Nusselt number approached the theoretical value of $140/17 \approx 2.235$ [17]. The finest mesh of 81×33 nodes produced a constant Nu value along the length of the top and bottom walls of 2.234. This represents an error of -0.04% with respect to theoretical. The cross-stream velocity profile also showed excellent agreement with theory [17].

Further validation of the PFD code was performed using the developing flow results described above. The pressure field solution for HEM #4 for $\mathrm{Re} = 50$ was used to extract the value of β. The mesh for HEM #4 was isolated for use in the PFD code. The value of β was used as input to the PFD code and the flow field was solved. Excellent agreement with the flow fields was obtained. Figure 4*a* shows a comparison of inlet u-velocity profiles for both PFD and DF solutions. The two profiles are indistinguishable in the plot. The maximum percent error in u-velocity over all 4,572 nodes was 0.4% and the average percent error was 0.006% over all nodes. The heat transfer problem with specified wall temperature could not be solved with the current version of the PFD code for comparison with Kundu et al. [16] or Bahaidarah et al. [12].

The PFD code was also tested for a specified heat flux problem. Again, the DF results from above were used. Using the solved flow field for $\mathrm{Re} = 50$ from the DF solution, the temperature field was solved with the DF code using a specified heat flux on the tube surface and with the channel walls insulated. The same problem was solved using the PFD code. Figure 4*b* shows the comparison of local Nu along the top half of the tube wall. As the DF solution moves downstream from HEM #2 to HEM #3 to HEM #4, the Nusselt number approaches that of the PFD solution. The DF HEM #4 the plot indicates that the flow is thermally fully-developed for the DF case within 2%.

For completeness, the DF problem from above was solved with a flat tube replacing the round tube and the results compared to the PFD code. Similar to the round tube results, the inlet u-velocity profiles are indistinguishable with the maximum percent error in u-velocity over all 4,580 nodes at 0.2% and the average

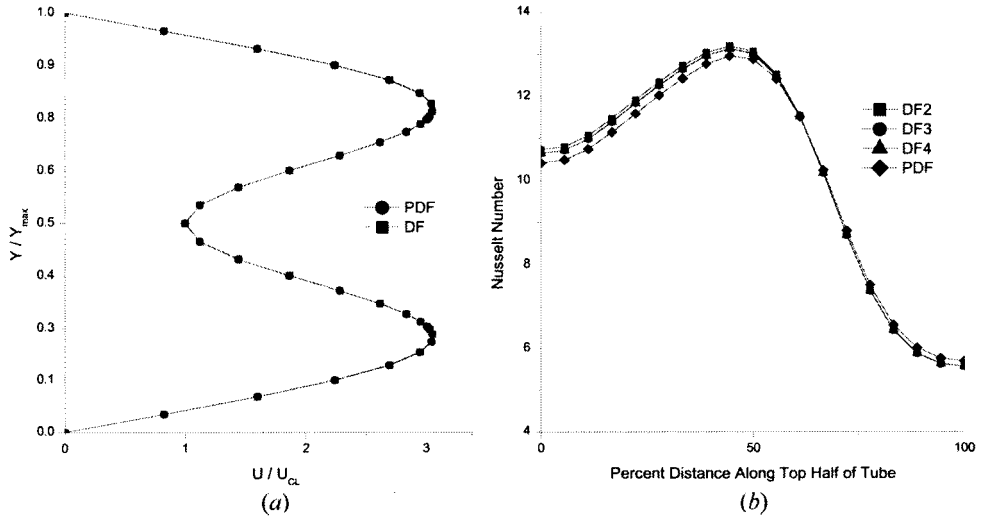

Figure 4. Comparison of PFD and DF solutions at Re = 50: (*a*) velocity profiles; and (*b*) local nusselt number.

percent error at 0.03% over all nodes. The same exercise was performed with the oval tube replacing the round tube. Once again, the inlet velocity profiles are indistinguishable with the maximum percent error over all 4,546 nodes at 0.48% and the average percent error at 0.07% over all nodes.

5. GRID INDEPENDENCE STUDY

For the current work, we are interested in comparing the performance of flat and oval tubes to that of a round tube with the same perimeter. Figure 1 shows geometry of the three associated computational domains. To establish grid independence, several meshes of increasing node density were constructed for each domain geometry and solved with the PFD code for β values corresponding to the maximum Re of interest of approximately 350. The grid independence study was performed for both $Pr = 0.7$ and $Pr = 7.0$.

Figure 5 shows the element mesh for a round-tube domain. The construction of this mesh is typical of all the meshes used in the current work. The tube surface was divided into equal-length straight sections. This established node locations representing the tube surface. Additional nodes were created along lines of constant x and constant y using the values of x and y associated with the previously established tube-surface nodes. This leads to elements and CVs of varying sizes. For regions of the mesh not influenced directly by the location of the tube-surface nodes, nodes were created along lines of constant x and y such that the element sides were approximately the same length as the straight sections representing the tube surface.

Table 2 shows a comparison of Reynolds numbers, friction factors, and average Nusselt numbers for these meshes at Re = 350 for both values of Prandtl number considered. Based on these results, it was decided to use Mesh-R #5 for the

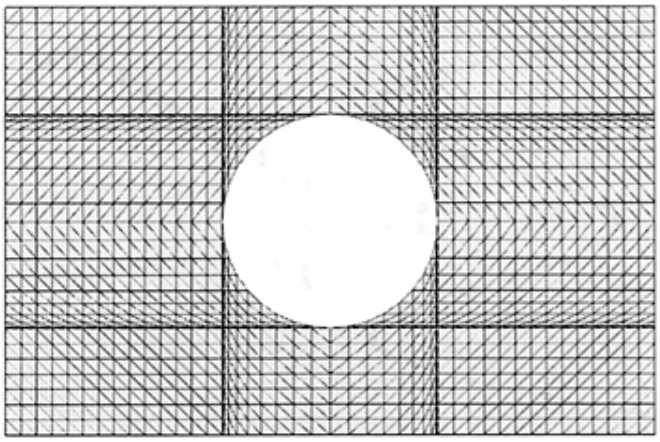

Figure 5. Typical element mesh for a round tube domain.

round-tube cases, Mesh-F #3 for the flat-tube cases, and Mesh-O #4 for the oval-tube cases. It should be noted that the same meshes were used for both $Pr = 0.7$ and $Pr = 7.0$. Only the material properties and β values were changed.

As part of the grid independence study, a parallel study of the effect of convergence limit on the results was also performed. Based on the data, it was decided to use a convergence limit of 10^{-6} for u, v, and $\widehat{T}$.

6. PROBLEM DESCRIPTION

To compare the performance of flat tubes and oval tubes to that of round tubes under similar flow conditions, the example problem described below was conceived. The domain geometries for round, flat, and oval tubes are shown in Figure 1. In each case, the size of the domain is $L \times H$ with the tube centered in the domain. The perimeters of the flat and oval tubes are equal to that of the round tube. Constant specified heat flux is assigned to the tube walls and the channel walls are insulated. Since the perimeters of the tubes are equal for all computational domains, equal amounts of energy are imparted to the fluid for all cases.

Calculations were made using the PFD code for seven different mean flow velocities for each domain for a Reynolds number range of 50–350. These calculations were performed for fluids of $Pr = 0.7$ and $Pr = 7.0$. For these cases, Reynolds number is based on the channel height. The Nusselt number is defined by Eq. (11) above.

For the PFD code, β, not velocity, is the input parameter. Therefore, the Reynolds numbers for the cases of interest cannot be chosen explicitly. For the $Pr = 0.7$ cases, an iterative process of choosing β and calculating Re was performed. The process was stopped when the calculated Re was within 0.5% of the target value for each of the seven target values.

For the $Pr = 7.0$ cases, we took advantage of the fact that for steady, laminar flows in the Re range of interest, the flows for $Pr = 0.7$ and $Pr = 7.0$ are dynamically similar if the Reynolds numbers are equal. This being the case, for a given domain

Table 2. Results of grid independence study

Mesh	Number of nodes	Re	Re % diff.	Friction factor	Friction % diff.	Average Nusselt number	Avg_Nu % diff.
Round tubes (Pr = 0.7)							
R #1	1406	330.123		1.221		12.37	
R #2	4572	349.729	5.94	1.088	−10.89	12.59	1.71
R #3	7506	353.316	1.03	1.066	−2.02	12.65	0.47
R #4	11822	355.37	0.58	1.054	−1.13	12.68	0.27
R #5	**13744**	**355.944**	**0.16**	**1.050**	**−0.38**	**12.69**	**0.06**
R #6	17114	356.629	0.19	1.046	−0.38	12.70	0.09
Flat tubes (Pr = 0.7)							
F #1	998	343.575		0.381		10.04	
F #2	4580	352.347	2.55	0.362	−4.99	10.13	0.83
F #3	**7972**	**353.405**	**0.30**	**0.36**	**−0.55**	**10.14**	**0.12**
F #4	12436	353.873	0.13	0.359	−0.28	10.15	0.06
Oval tubes (Pr = 0.7)							
O #1	1220	337.418		0.563		10.58	
O #2	4546	349.064	3.45	0.526	−6.57	10.65	0.71
O #3	7884	351.019	0.56	0.52	−1.14	10.66	0.12
O #4	**12356**	**351.998**	**0.28**	**0.517**	**−0.58**	**10.67**	**0.06**
O #5	17828	352.619	0.18	0.515	−0.39	10.68	0.05
Round tubes (Pr = 7.0)							
R #1	1406	324.069		1.239		15.22	
R #2	4572	343.197	5.90	1.104	−10.90	15.22	−0.01
R #3	7506	346.68	1.01	1.082	−1.99	15.30	0.53
R #4	11822	348.683	0.58	1.07	−1.11	15.36	0.41
R #5	**13744**	**349.243**	**0.16**	**1.067**	**−0.28**	**15.38**	**0.12**
R #6	17114	349.787	0.16	1.063	−0.37	15.40	0.11
Flat tubes (Pr = 7.0)							
F #1	998	340.279		0.384		10.94	
F #2	4580	348.963	2.55	0.365	−4.95	10.93	−0.09
F #3	**7972**	**350.01**	**0.30**	**0.363**	**−0.55**	**10.96**	**0.32**
F #4	12436	350.475	0.13	0.362	−0.28	10.98	0.17
Oval tubes (Pr = 7.0)							
O #1	1220	335.535		0.565		12.25	
O #2	4546	347.082	3.44	0.528	−6.55	12.22	−0.23
O #3	7884	348.937	0.53	0.523	−0.95	12.25	0.28
O #4	**12356**	**350.138**	**0.34**	**0.519**	**−0.76**	**12.28**	**0.22**
O #5	17828	350.376	0.07	0.518	−0.19	12.29	0.08

geometry at a chosen Re value of interest, we expect the friction factors to be equal no matter which fluid we choose. Combining equations for the friction factor and for the Reynolds number, the following relationship for $\beta_{7.0}$ may be developed.

$$\beta_{7.0} = \beta_{0.7} \frac{\rho_{0.7}}{\rho_{7.0}} \left[\frac{\mu_{7.0}}{\mu_{0.7}}\right]^2 \tag{12}$$

Eq. (12) gives the required value of β for the Pr = 7.0 fluid to match the Reynolds number of the Pr = 0.7 fluid for the same domain geometry. This concept was confirmed by the fact that using β values calculated in this way, the calculated

Table 3. Nominal and calculated Reynolds numbers

Nominal values	Round (calculated)	Flat (calculated)	Oval (calculated)
50	50.051	50.306	49.808
100	100.087	100.474	99.914
150	150.103	150.558	149.927
200	199.797	200.228	199.791
250	249.467	249.999	249.06
300	299.569	298.972	300.114
350	349.992	349.793	350.043

Re and friction factor values for $Pr = 7.0$ did indeed match the values from the $Pr = 0.7$ cases.

Use of Eq. (12) allows the Reynolds number values for a particular domain geometry to match for both fluids considered. However, the Reynolds number values for different geometries are not equal. They are, however, well within 0.5% of the nominal target value. Table 3 lists the nominal target Re values along with the calculated values for the three different computational domain geometries. From this point forward, we will compare results from different geometries using the nominal Re values and the nominal Re values will appear on the various data plots of results.

Since all three domains are symmetric about a longitudinal centerline, the results should be symmetric about this centerline. This raises the possibility of imposing symmetric boundary conditions along the longitudinal centerline and solving only one-half of the domains. However, symmetric boundary conditions were not used for the cases below. Rather, the entire domain was solved and the results examined for symmetry. With the solution domain limited to a single PFD module, the additional solution time associated with solving the entire domain rather than solving half of the domain was not an issue. In all cases, the expected symmetry was demonstrated in the resulting u, v, $\widehat{P}$, and $\widehat{T}$ fields.

7. FLOW RESULTS

Figure 6 presents streamline plots for all cases considered. The streamline plots for each different domain geometry represent results for both $Pr = 0.7$ and $Pr = 7.0$ at a given Reynolds number. From the streamline plots it is evident that the steady 2-D flow field is symmetric about the longitudinal centerline for each domain at each Reynolds number tested.

Figure 6*a* for the round tube cases shows that the character of the flow field changes from $Re = 50$ to $Re = 150$ as the vortices downstream of the tube increase in size and move downstream from the tube. However, for $Re = 200$ through $Re = 350$, only minor changes in the streamline plots are observed, mainly in the separation bubbles near the domain's upper and lower boundaries.

Figure 6*b* for the flat tube cases shows changes in the flow pattern throughout the Reynolds number range of the cases considered in this study. The last two cases, $Re = 300$ and $Re = 350$, look very similar to each other, but minor changes are observed in the size and position of the tube trailing vortices. There appears to be

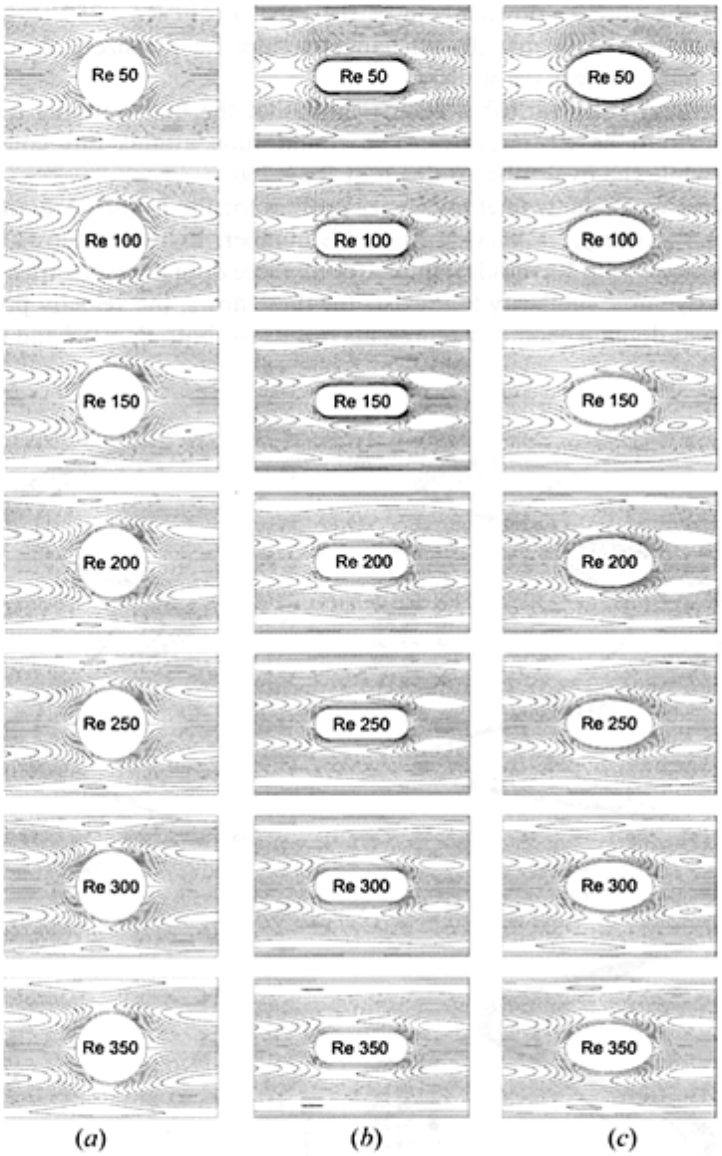

Figure 6. Streamline plots for Pr = 0.7 and Pr = 7.0: (*a*) round tube cases; (*b*) flat tube cases; and (*c*) oval tube cases.

a trend toward commonality of the flow pattern as Reynolds number increases, but this commonality is not reached in the Reynolds number range considered in this study. Perhaps if higher Reynolds numbers were tested, we would see the same degree of commonality reached as demonstrated by the round and oval tube cases.

Figure 6*c* for the oval-tube cases shows characteristics similar to those of the round tube cases. From Re = 50 to Re = 200, we again see changes in the size and

position of the vortices downstream of the tube. From Re = 250 to Re = 350, the streamline plots remain virtually unchanged except for the size and position of the separation bubbles near the walls.

The round and oval tubes results show that the flow patterns tend toward a common pattern as Re increases. The round tube attains this commonality at Re = 200, while the oval tube attains it at Re = 250.

Figures 7*a*–7*c* show inlet *u*-velocity profiles for the round, flat, and oval tubes domains, respectively, for varying Reynolds number. Figure 7*d* shows the variation of friction factor with Reynolds number for all three domain geometries. Once again, due to the dynamic similarity that exists for these flows, the velocity profile plot for each different domain geometry represents results for both Pr = 0.7 and Pr = 7.0. The

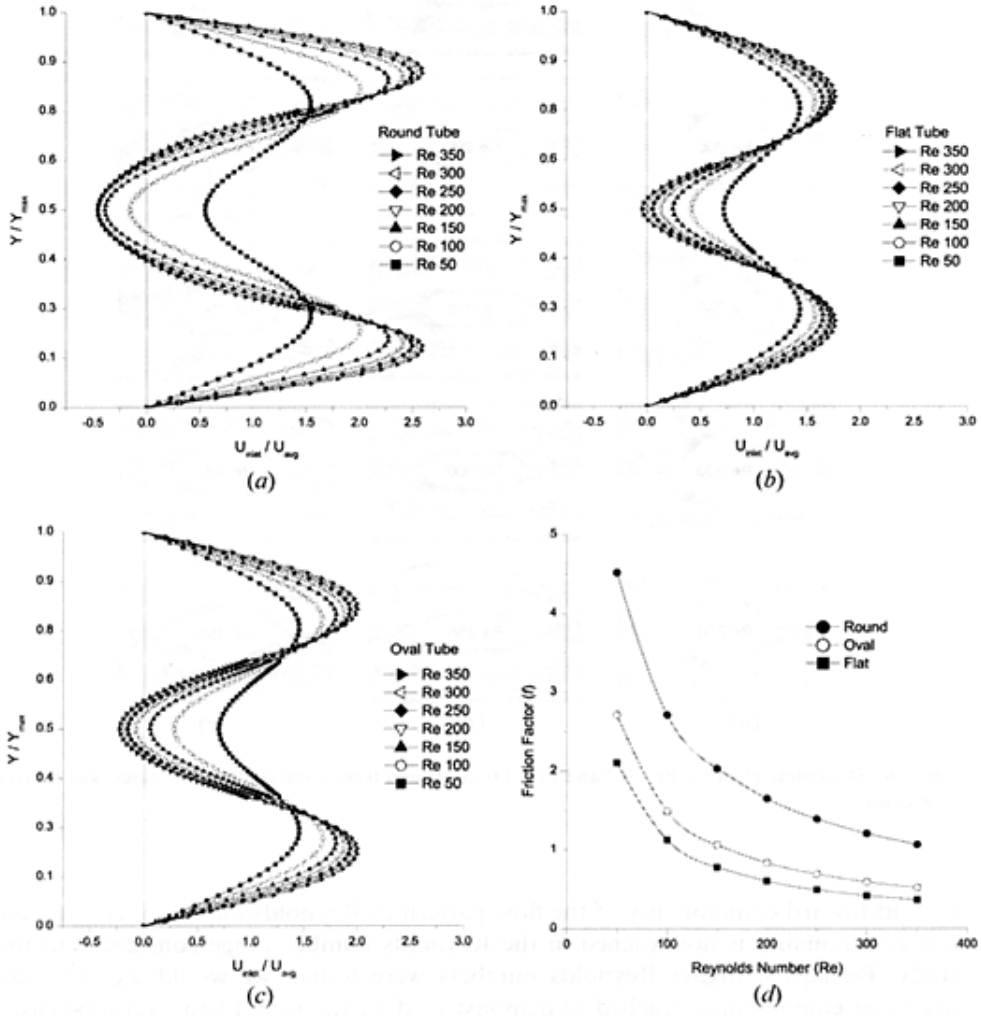

Figure 7. Flow results for Pr = 0.7 and Pr = 7.0: (*a*) round tube velocity profiles; (*b*) flat tube velocity profiles; (*c*) oval tube velocity profiles; and (*d*) friction factor for all tube shapes.

u-velocity at the domain inlet is normalized with respect to the average inlet velocity for each Re value considered so that while the velocity magnitudes differ from $Pr = 0.7$ to $Pr = 7.0$, the normalized velocity values at the same points for the same Reynolds number are the same.

The velocity profile plots demonstrate the symmetry in the flow solution about the longitudinal centerline for each domain. For the round tube at $Re = 100$ and higher, the normalized inlet velocity near the centerline of the domain takes negative values. This is an indication of the impact of the wake from the upstream module. This effect is also seen for the flat tube cases, but only for the highest Re in the range considered in this study ($Re = 350$). For the oval tube, as Re is increased, negative normalized velocities exist for $Re = 200$ and higher.

For each of the three domain geometries, as Re increases, the normalized inlet velocity profiles tend toward a common profile, as suggested by the streamline plots in Figure 6. For the round tube, Figure 7*a* shows that the velocity profiles for $Re = 200$ and higher are virtually identical. For the oval tube, Figure 7*c* shows the same effect for $Re = 250$ and higher. This effect is less prevalent for the flat tube for the Reynolds number range tested, as seen in Figure 7*b*. As explained earlier, velocity is minimum along the centerline for all three geometries of tubes considered in this study. Flow accelerates in the passage between the tube surface and channel wall giving rise to a maximum value in this region. Thus, one can find one maximum velocity point above the centerline and one below the centerline for all cases. At higher Re values, the wake effect of upstream module is more significant giving rise to a larger negative velocity along the centerline.

Friction factor (f) was calculated for all cases using Eq. (9) above. Figure 7*d* shows plots of f versus Re for all three domain geometries considered. Once again, the plot represents results for both $Pr = 0.7$ and $Pr = 7.0$. Figure 7*d* shows that for a chosen tube shape, the friction factor decreases with increasing Reynolds number as expected for laminar flows because as the Re value increases, the inertial force dominates the viscous force. Figure 7*d* also shows that for a given Reynolds number in the range tested, the round-tube friction factor is highest, followed by the oval tube friction factor and then the flat tube friction factor. The size of recirculation bubble downstream of each tube is impacted by, flow separation and reattachment. It is evident from Figure 6 that for a given value of Re, the recirculation bubble is largest for the round tube case and smallest for the flat tube case. This is the reason for the circular tube case to have the highest value of friction factor, and the flat tube case to have the lowest value of friction factor for a fixed Re value. As expected, for a fixed Re value the friction factor value for the oval tube case lies between those for round and flat tube cases. While the three tubes have equal perimeters, they have different blockage ratios. The blockage ratios for the round, oval, and flat tubes are 0.5, 0.35, and 0.22, respectively. The difference in blockage ratios along with the difference in the general shape of the tubes leads to the higher friction factor for the round tube.

8. HEAT TRANSFER RESULTS

While the flow results exhibit dynamic similarity for $Pr = 0.7$ and $Pr = 7.0$, the heat transfer results do not. These results will therefore be presented separately.

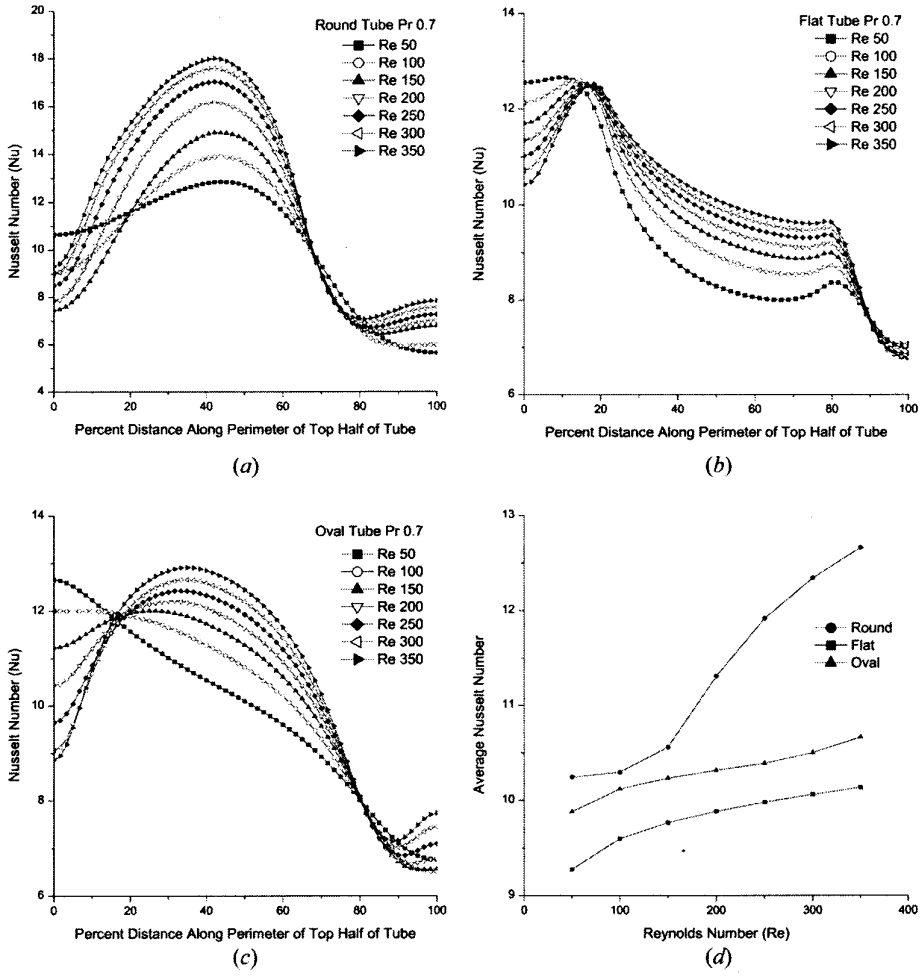

Figure 8. Heat transfer results for Pr-0.7: (*a*) round tube cases; (*b*) flat tube cases; (c) oval tube cases; and (*d*) average nusselt number.

Figure 8 shows the heat transfer results for Pr = 0.7. Figures 8*a–c* show the local Nusselt number distribution along the top half of the tube for each of the three geometries considered in this study for different Reynolds numbers. Due to symmetry, the distribution along the bottom half of the tube is identical. In these plots, 0% along the perimeter corresponds to the leading edge of the tube and 100% along the perimeter corresponds to the trailing edge. Figure 8*d* shows a comparison of average Nusselt number as a function of Reynolds number for all three geometries considered in this study.

The Nusselt number plots display markedly different characteristics. Figure 8*a* for the round tube cases shows that the Nusselt number increases from the leading

edge of the tube reaching a maximum value at a location approximately 42%–45% along the perimeter. This maximum is followed by decreasing values as the trailing edge is approached at approximately 80% along the perimeter. A slight increase of Nu along the final 20% of the perimeter is observed. At the leading edge, Nu decreases with increasing Re. The peak Nu increases with increasing Re from 12.5 at Re = 50 to 18.0 at Re = 350. At the trailing edge, Nu increases with increasing Re.

Figure 8*b* for the flat tube cases shows an increase in Nu from the leading edge of the tube to a maximum value at approximately 22% along the perimeter. This is the location where the straight section of the tube begins. Following the peak, the plot shows decreasing Nu values as the end of the straight section is approached. Along the trailing curved section, we observe a steeper decrease in Nu as the trailing edge is approached. At the leading edge, Nu decreases with increasing Re. However, for all Re values, a common peak value of approximately 12.5 is reached. Along the straight section of the tube, Nu increases with increasing Re. A common minimum value of Nu is reached at the trailing edge for all Re.

Figure 8*c* for the oval tube cases shows that the lower two Re value curves show characteristics unlike those for the higher Re. At Re = 50, the Nu plot shows a maximum at the leading edge followed by an almost linear decrease along the entire perimeter toward the trailing edge. At Re = 100, the maximum Nu once again occurs at the leading edge followed by a gradual decrease all along the perimeter. For Re = 150 through Re = 350, the curves show an increase in Nu from the leading edge to a peak between 22% along the perimeter for Re = 150, to a peak at 38% along the perimeter for Re = 350. Unlike the round tube results which showed the peaks in a tight grouping between 42% and 45% along the perimeter, the peaks for the oval tube cases are spread out. At the leading edge, Nu decreases for increasing Re. The peak value increases with increasing Re. A slight increase in Nu is observed at the trailing edge as Re increases.

Figure 8*d* shows that the average Nusselt number for a given tube shape increases with increasing Reynolds number. The flat and oval tubes show an almost linear increase in Nu with increasing Re. However, the round tube plot shows a sharp increase in the rate of change starting at Re = 150. For a given Reynolds number, the round tube average Nusselt number is highest, followed by the oval tube and then the flat tube values. In general, Nu increases with Re. As stated before, the case of the round tube has the highest blockage ratio and the case of flat tube is the lowest blockage ratio. Thus, flow velocity in passages between the tube and the channel is highest for the round tube case and lowest for the flat tube case. Higher velocities lead to thinner momentum and thermal boundary layers for a constant property fluid flow case. Thinner thermal boundary layers lead to higher heat transfer coefficients. This is the reason for the round tube case to have the highest average Nusselt number, and the flat tube case to have the lowest for a fixed value of Re.

From Figures 8*a*–8*c*, we see that even though the amount of energy imparted to the fluid is equal for all tube shapes, the Nusselt number and therefore the local heat transfer coefficient vary in distinctly different ways for the three tube shapes. From the definition of Nu given in Eq. (11) above, if q'', D_h, and k are constant for all cases, the variation of Nu along the tube surface must be due to variation

in the temperature difference $(\hat{T}_s - \hat{T}_b)$. Furthermore, for these cases, the bulk temperature increases steadily but gradually in the streamwise direction. Therefore, the variations of $(\hat{T}_s - \hat{T}_b)$ are due mainly to variations in the surface temperature. Because $(\hat{T}_s - \hat{T}_b)$ is in the denominator of Eq. (11), we can conclude that at a location where Nu reaches a local maximum, that the surface temperature is at a local minimum. Conversely, at a location where Nu is at a local minimum, surface temperature is at a local maximum.

Figure 9 shows the heat transfer results for Pr = 7.0. These results are presented in the same format as for the Pr = 0.7 results described above. Figures 9*a*–9*c* showing the local Nusselt number distribution for Pr = 7.0 are similar in shape to their

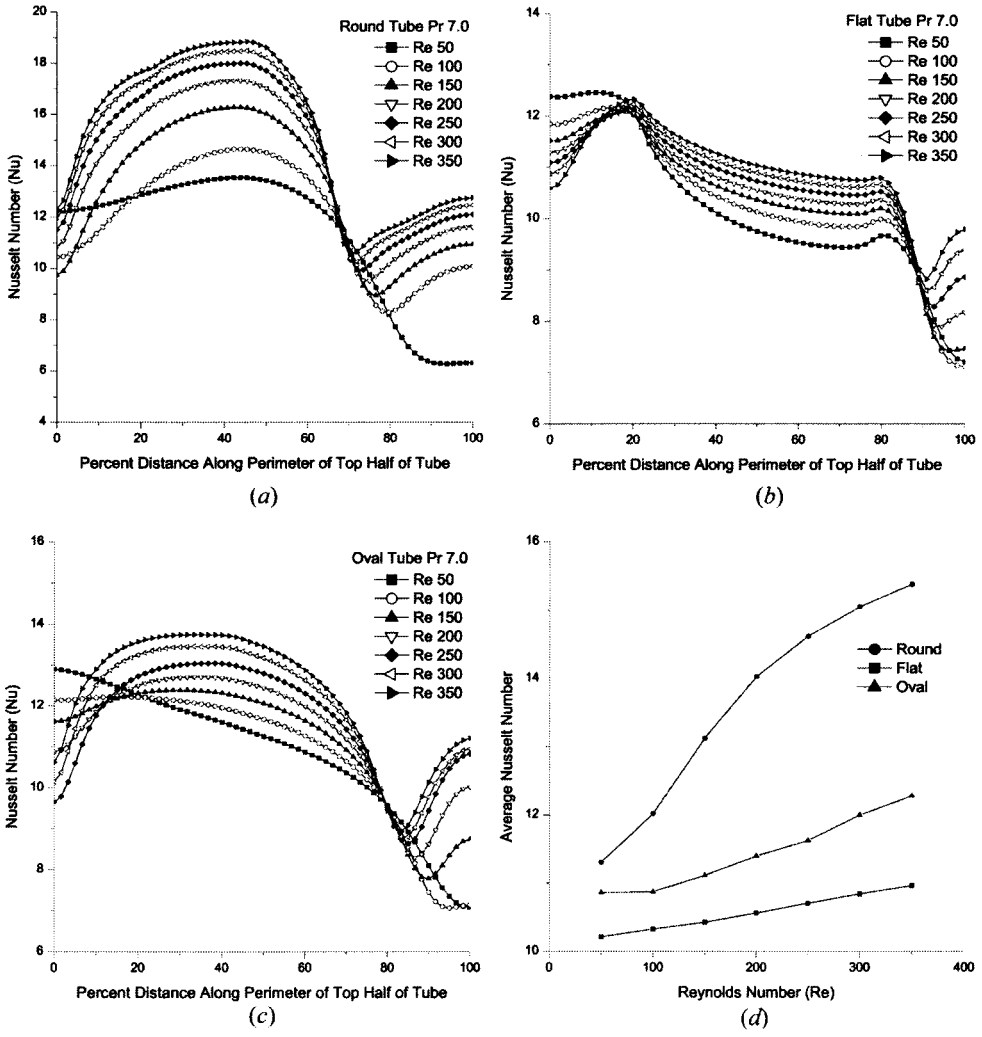

Figure 9. Heat transfer results for Pr-7.0: (*a*) round tube cases; (*b*) flat tube cases; (*c*) oval tube cases; and (*d*) average nusselt number.

$Pr = 0.7$ counterparts, but the peaks have shifted position slightly and the magnitudes are different. One distinguishing feature of the $Pr = 7.0$ plots compared to the $Pr = 0.7$ plots is the sharp increase of Nu at the trailing edge of the tube for all three tube geometries. This is due to the effect of the Prandtl number on the relative thicknesses of the momentum and thermal boundary layers. The thermal boundary layer thickness for $Pr = 7.0$ is much thinner compared to that for $Pr = 0.7$. This leads to increased heat transfer performance at the trailing edge of the tube for the $Pr = 7.0$ cases as compared to the $Pr = 0.7$ cases, leading to a higher Nusselt number value. Figure 9*d* shows that for $Pr = 7.0$, as for $Pr = 0.7$, the average Nusselt number for the round tube is higher than that for either the flat or the oval tubes for a given Reynolds number. Also, comparing Figures 8*d* and 9*d*, the average Nusselt number for a given tube shape at a given Reynolds number is higher for $Pr = 7.0$ compared to $Pr = 0.7$.

9. PERFORMANCE COMPARISON OF FLAT AND OVAL TUBES TO THE ROUND TUBE

To compare flat and oval tubes performance to that for the round tube for a given Reynolds number based only on heat transfer performance, we define the heat transfer enhancement ratio (Nu^+) as follows:

$$Nu^+ \equiv \frac{Nu_{avg,noncircular}}{Nu_{avg,round}} \tag{13}$$

In Eq. (13), Nu_{avg} represents the average Nu along the perimeter of the top half of the tube for any of the three tube shapes at the same Reynolds number. Figures 10*a*

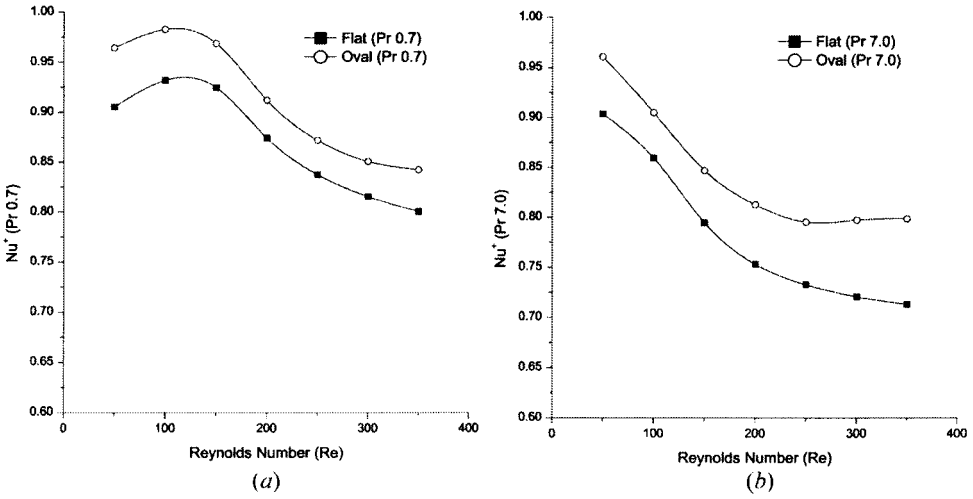

Figure 10. Heat transfer enhancement ratio versus Reynolds number: (*a*) $Pr = 0.7$ and (*b*) $Pr = 7.0$.

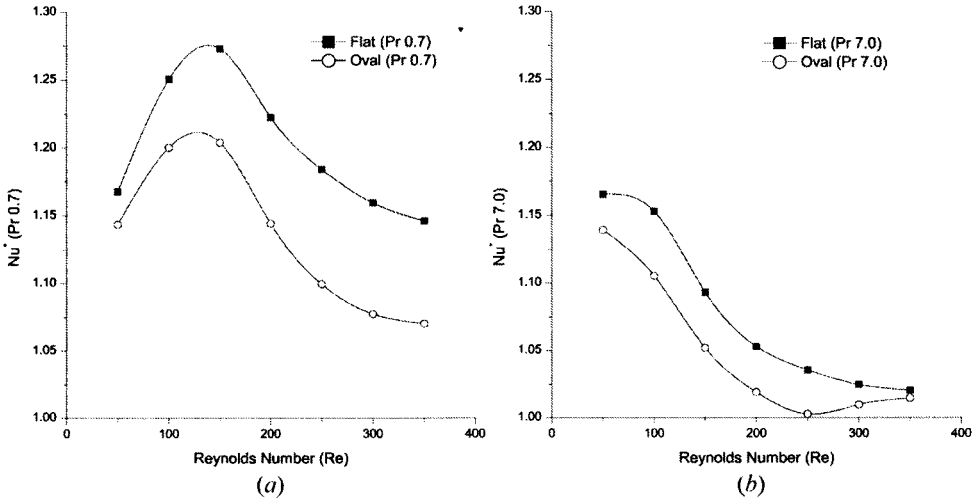

Figure 11. Heat transfer performance ratio versus Reynolds number: (*a*) Pr = 0.7 and (*b*) Pr = 7.0.

and 10*b* show plots of Nu^+ versus Re for Pr = 0.7 and Pr = 7.0, respectively. In all cases studied, Nu^+ was less than one indicating that for a given Reynolds number the average heat transfer coefficient for the round tube is greater than that for the flat tube or the oval tube. If one only considers heat transfer performance, the round tube outperforms both the flat and the oval tubes.

To compare the performance of the three tube shapes based on both heat transfer and overall flow considerations, we define the heat transfer performance ratio (Nu^*) for a given Reynolds number:

$$Nu^* \equiv \frac{Nu^+}{[f_{\text{flat or oval}}/f_{\text{round}}]^{1/3}} \tag{14}$$

In Eq. (14), Nu^+ is the heat transfer enhancement ratio, $f_{\text{flat or oval}}$ is the friction factor for either the flat or oval tube, and f_{round} is the round tube friction factor, all at the same Reynolds number. The denominator is proportional to the ratio of pumping power required to maintain the flow in either the flat or oval tubes domain for a given Reynolds number to that required for the round tube domain. Figures 11*a* and 11*b* show plots of Nu^* versus Re for the cases studied at Pr = 0.7 and Pr = 7.0, respectively. In all cases studied, Nu^* is greater than one indicating that if pumping power is considered along with heat transfer to compare performance, then either the flat or oval tubes outperforms the round tube.

10. CONCLUSION

The current work demonstrates the viability of using a CVFEM along with PFD conditions to study tube-in-cross-flow problems. One of the advantages to

using a single-module domain with imposed PFD conditions is that the domain is limited to the domain of interest—entry and exit lengths are not required and multiple modules are not required. This results in shorter solution times and more efficient use of available computing resources. Another advantage is that the resulting solution truly exhibits PFD conditions rather than approximate PFD conditions.

For the example, problems studied comparing the performance of flat and oval tubes to that of round tubes, the round tube performed better from a heat transfer standpoint based on the heat transfer enhancement ratio. However, the heat transfer performance ratio was greater than one for all cases indicating that if both heat transfer and pumping power are to be considered, then the flat or oval tube may be a better choice.

REFERENCES

1. C. Prakash, A Finite Element Method for Predicting Flow through Ducts with Arbitrary Cross Sections, Ph.D. Thesis, University of Minnesota, 1982.
2. C. Prakash, and S. V. Patankar, A Control Volume-Bases Finite-Element Method for Solving the Navier-Stokes Equations Using Equal-Order Velocity-Pressure Interpolation, *Numer. Heat Transfer*, vol. 8, pp. 259–280, 1985.
3. H. J. Saabas, A Control Volume Finite Element Method for Three-Dimensional, Incompressible, Viscous Fluid Flow, Ph.D. Thesis, McGill University, Montreal, Canada, 1991.
4. H. J. Saabas and B. R. Baliga, Colocated Equal-Order Control-Volume Finite-Element Method for Multidimensional, Incompressible, Fluid Flow—Part I: Formulation, *Numer. Heat Transfer B*, vol. 26, pp. 381–407, 1994.
5. H. J. Saabas and B. R. Baliga, Colocated Equal-Order Control-Volume Finite-Element Method for Multidimensional, Incompressible, Fluid Flow—Part II: Verification, *Numer. Heat Transfer B*, vol. 26, pp. 409–424, 1994.
6. S. R. Husain, Extensions of the Control Volume Based Finite Element Method for Fluid Flow Problems, Ph.D. Thesis, Texas A&M University, College Station, TX, USA, 1987.
7. B. R. Baliga and S. V. Patankar, A New Finite-Element Formulation for Convection-Diffusion Problems, *Numer. Heat Transfer*, vol. 3, pp. 393–409, 1980.
8. B. R. Baliga and S. V. Patankar, A Control Volume Finite-Element Method for Two-Dimensional Fluid Flow and Heat Transfer, *Numer. Heat Transfer*, vol. 6, pp. 245–261, 1983.
9. C. Prakash, An Improved Control Volume Finite-Element Method for Heat, and Mass Transfer, and for Fluid Flow Using Equal-Order Velocity–Pressure Interpolation, *Numer. Heat Transfer*, vol. 9, pp. 253–276, 1986.
10. G. E. Schneider and M. J. Raw, A Skewed, Positive Influence Coefficient Upwinding Procedure for Control-Volume-Based Finite-Element Convection-Diffusion Computation, *Numer. Heat Transfer*, vol. 9, pp. 1–26, 1986.
11. N. A. Hookey, B. R. Baliga, and C. Prakash, Evaluation, and Enhancements of Some Control Volume Finite-Element Methods—Part 1, Convection-Diffusion Problems, *Numer. Heat Transfer*, vol. 14, pp. 255–272, 1988.
12. H. M. S. Bahaidarah, N. K. Anand, and M. Ijaz, Numerical Study of Fluid Flow and Heat Transfer Over A Series of In-Line Noncircular Tubes Confined in a Parallel-Plate Channel, *Numer. Heat Transfer B*, vol. 50, pp. 97–119, 2006.

13. S. V. Patankar, *Numerical Heat Transfer and Fluid Flow*, McGraw Hill, New York, 1980.
14. S. V. Patankar, C. H. Liu, and E. M. Sparrow, Fully Developed Flow and Heat Transfer in Ducts Having Streamwise-Periodic Variations of Cross-Sectional Area, *ASME J. Heat Transfer*, vol. 99, pp. 180–186, 1977.
15. S. H. Kim and N. K. Anand, Periodically Fully Developed Flow in Channels with Conducting Blockages, *J. Thermophysics*, vol. 6, no. 1, pp. 91–97, 1992.
16. D. Kundu, A. Haji-Sheikh, and D. Y. S. Lou, Pressure and Heat Transfer in Cross Flow over Cylinders between Two Parallel Plates, *Numer. Heat Transfer A*, vol. 19, pp. 345–360, 1991.
17. A. F. Mills, *Heat Transfer*, Prentice Hall, New Jersey, 1999.

APPENDIX B – INTERPOLATION FUNCTION FOR ϕ WITHIN AN ELEMENT

To evaluate the link flux integrals on the LHS of Eq.(3.6), the distributions of ϕ, $\partial\phi/\partial X$ and $\partial\phi/\partial Y$ along the element links are required. To this end, a nonlinear interpolation function for ϕ is introduced. The equations in Eq.(3.8) are repeated here for convenience as Eq.(B.1) through Eq.(B.4). Eq.(B.1) is an expression for the value of the general transported variable ϕ at an (*X*,*Y*) location within an element.

$$\phi(X,Y) = AZ(X) + BY + C \qquad \text{Eq.(B.1)}$$

$$Z(X) = \frac{\Gamma}{\rho\tilde{U}_{avg}}\left\{\exp\left[Pe\frac{(X - X_{\max})}{(X_{\max} - X_{\min})}\right] - 1\right\} \qquad \text{Eq.(B.2)}$$

$$Pe = \frac{\rho\tilde{U}_{avg}(X_{\max} - X_{\min})}{\Gamma} \qquad \text{Eq.(B.3)}$$

$$\begin{aligned} X_{\max} &= \max(X_1, X_2, X_3) \\ X_{\min} &= \min(X_1, X_2, X_3) \end{aligned} \qquad \text{Eq.(B.4)}$$

Eq.(B.1) is known as the *interpolation function* for ϕ within the element. Eq.(B.2) defines *Z(X)* within Eq.(B.1). Note that *Z* is a function of *X*. Eq.(B.3) defines the element Peclet number. $\tilde{U}_{avg}$ in Eq.(B.2) and Eq.(B.3) is the average magnitude of the element velocity vector for the element's three nodes. Eq.(B.4) defines $X_{\max}$ and $X_{\min}$ as the maximum and minimum, respectively, of the *X*-coordinates of the element's nodes in the local element coordinate system. Eq.(B.1) through Eq.(B.4) show that the value of ϕ at a location (*X*,*Y*) within the element is dependent upon the element geometry, the average velocity within the element, and specified material properties.

Before Eq.(B.1) can be used in the evaluation of link fluxes, the coefficients *A*, *B*, and *C* must be determined. The coefficients are determined by applying the constraint that Eq.(B.1) is valid at each of the element's three nodes. This produces a set of three equations which may be solved for the coefficients *A*, *B*, and *C*.

$$\begin{aligned} \phi_1 &= AZ_1 + BY_1 + C \\ \phi_2 &= AZ_2 + BY_2 + C \\ \phi_3 &= AZ_3 + BY_3 + C \\ &\text{where } Z_i = Z(X_i) \end{aligned} \qquad \text{Eq.(B.5)}$$

While neither the values of ϕ at the nodes nor the values of coefficients *A*, *B*, or *C* are known, the ϕ values will be treated as knowns in Eq.(B.5). Rewriting Eq.(B.5) in matrix form yields Eq.(B.6).

$$\begin{bmatrix} Z_1 & Y_1 & 1 \\ Z_2 & Y_2 & 1 \\ Z_3 & Y_3 & 1 \end{bmatrix} \begin{bmatrix} A \\ B \\ C \end{bmatrix} = \begin{bmatrix} \phi_1 \\ \phi_2 \\ \phi_3 \end{bmatrix} \qquad \text{Eq.(B.6)}$$

Solving the three-equation system in Eq.(B.6) for *A*, *B*, and *C* yields the following expressions.

$$\begin{aligned} A &= L_1\phi_1 + L_2\phi_2 + L_3\phi_3 \\ B &= M_1\phi_1 + M_2\phi_2 + M_3\phi_3 \\ C &= N_1\phi_1 + N_2\phi_2 + N_3\phi_3 \end{aligned} \qquad \text{Eq.(B.7)}$$

$$\begin{aligned} L_1 &= (Y_2 - Y_3)/DET_\phi \\ L_2 &= (Y_3 - Y_1)/DET_\phi \\ L_3 &= (Y_1 - Y_2)/DET_\phi \end{aligned} \qquad \text{Eq.(B.8)}$$

$$\begin{aligned} M_1 &= (Z_3 - Z_2)/DET_\phi \\ M_2 &= (Z_1 - Z_3)/DET_\phi \\ M_3 &= (Z_2 - Z_1)/DET_\phi \end{aligned} \qquad \text{Eq.(B.9)}$$

$$N_1 = (Z_2 Y_3 - Z_3 Y_2)/DET_\phi$$
$$N_2 = (Z_3 Y_1 - Z_1 Y_3)/DET_\phi \qquad \text{Eq.(B.10)}$$
$$N_3 = (Z_1 Y_2 - Z_2 Y_1)/DET_\phi$$

$$DET_\phi = Z_1(Y_2 - Y_3) + Z_2(Y_3 - Y_1) + Z_3(Y_1 - Y_2) \qquad \text{Eq.(B.11)}$$

The coefficients *A*, *B*, and *C* are not numerical. Rather, they are expressions in terms of the unknown ϕ values at the element's nodes. Use of Eq.(B.1) in conjunction with Eq.(B.7) through Eq.(B.11) specifies the value of ϕ at an (*X*, *Y*) location within the element in terms of the unknown values of ϕ at the nodes. Specifically, expressions for ϕ may be determined at the element's integration points.

Expressions for $\partial\phi/\partial X$ and $\partial\phi/\partial Y$ along the links are also required. Differentiating Eq.(B.1) with respect to *X* yields the following expression for $\partial\phi/\partial X$.

$$\frac{\partial\phi}{\partial X} = A\left[\frac{\rho U_{avg}}{\Gamma} Z(X) + 1\right] \qquad \text{Eq.(B.12)}$$

Differentiating Eq.(B.1) with respect to *Y* yields the following expression for $\partial\phi/\partial Y$.

$$\frac{\partial\phi}{\partial Y} = B \qquad \text{Eq.(B.13)}$$

In Eq.(B.12) and Eq.(B.13), *A* and *B* are defined by Eq.(B.7) through Eq.(B.11).

APPENDIX C – FLUX INTEGRATION FOR ELEMENT LINKS

This appendix discusses the integration of the flux of the general transported scalar ϕ across element links. The general transported scalar ϕ may represent velocity components *u* or *v* or it may represent temperature (*T*), but not pressure (*P*).

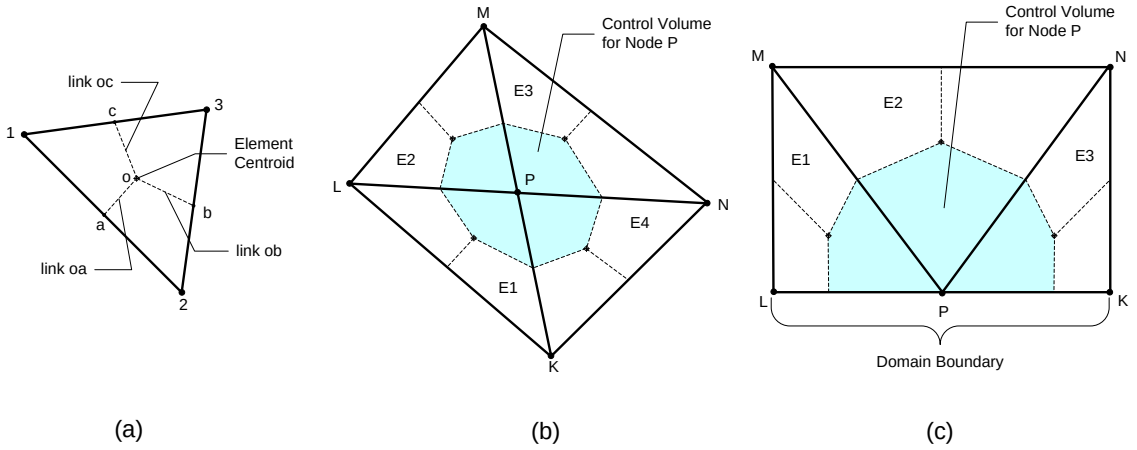

Figure C-1. CVFEM domain discretization: (a) typical element; (b) internal CV; (c) boundary CV.

Figure C-1 shows a typical element, an internal control volume (CV) and a boundary CV. Each element is defined by an ordered set of three nodes. Each node has both a global node number (GNN) and an element local node number (LNN) associated with it. GNN's are unique within the domain. The possible values for LNN are 1, 2, and 3. For example, E_1{K, P, L} represents the definition of Element 1 (E_1) shown in Figure C-1(b) in terms of the GNN's K, P, and L. In the definition, the GNN's are ordered such that as the perimeter of the triangle is traversed from K to P to L, one travels in a counter-clockwise direction. The LNN's are assigned based on the order of

the GNN's in the definition of the element. For example, LNN_1 corresponds with GNN_K, LNN_2 corresponds with GNN_P, and LNN_3 corresponds with GNN_L.

Each element is divided into three equal-area sub-regions by constructing element links from the element centroid to the midpoints of each of the three sides as shown in Figure C-1(a). A control volume for a given node is formed from sub-regions of elements that share that node. Figure C-1(b) shows that the element links form the outer boundary of an internal CV. Figure C-1(c) shows that for a boundary CV, a combination of element links and domain boundary segments form the outer CV boundary.

For a given element link, Simpson's One-Third Rule is applied to evaluate the flux integrals. Simpson's One-Third Rule assumes a parabolic distribution of flux along the link. To apply Simpson's One-Third Rule to an element link, the values of the integrand at the two endpoints of the link and at the midpoint of the link are needed. It should be noted that since the element links lie within elements and since constant material properties are assigned to elements in this method, the values of ρ and Γ may be treated as constants in the following expressions. The harmonic mean is not required.

The result of the integration process is an expression for the integrated flux across each link in terms of numerical coefficients λ's and unknown values of ϕ at the element's nodes. These expressions take the form of

$$\int_{\text{link oa}} (\bar{J}^{EV} \cdot \hat{N}_a) dl = \sum_{i=1}^{3} \lambda_i^{oa} \phi_i$$
$$\int_{\text{link ob}} (\bar{J}^{EV} \cdot \hat{N}_b) dl = \sum_{i=1}^{3} \lambda_i^{ob} \phi_i \qquad \text{Eq.(C.1)}$$
$$\int_{\text{link oc}} (\bar{J}^{EV} \cdot \hat{N}_c) dl = \sum_{i=1}^{3} \lambda_i^{oc} \phi_i$$

In Eq.(C.1), the subscript *i* corresponds to the element local node numbers.

The values for the coefficients are given by the equations below.

$$\lambda_i^{oa} = \dot{m}_{avg,oa}(L_i \bar{Z}_{oa} + M_i \bar{Y}_{oa} + N_i) - (\rho V_{avg} \bar{Z}_{oa} - \Gamma) L_i Y_a + \Gamma M_i X_a$$
$$\lambda_i^{ob} = \dot{m}_{avg,ob}(L_i \bar{Z}_{ob} + M_i \bar{Y}_{ob} + N_i) - (\rho V_{avg} \bar{Z}_{ob} - \Gamma) L_i Y_b + \Gamma M_i X_b \qquad \text{Eq.(C.2)}$$
$$\lambda_i^{oc} = \dot{m}_{avg,oc}(L_i \bar{Z}_{oc} + M_i \bar{Y}_{oc} + N_i) - (\rho V_{avg} \bar{Z}_{oc} - \Gamma) L_i Y_c + \Gamma M_i X_c$$

$$\dot{m}_{avg,oa} = \rho\left[\tilde{U}_r Y_a - \tilde{V}_r X_a\right]$$
$$\dot{m}_{avg,ob} = \rho\left[\tilde{U}_s Y_b - \tilde{V}_s X_b\right] \qquad \text{Eq.(C.3)}$$
$$\dot{m}_{avg,oc} = \rho\left[\tilde{U}_t Y_c - \tilde{V}_t X_c\right]$$

$$\bar{Z}_{oa} = \frac{Z_o + 4Z_r + Z_a}{6} \qquad \bar{Y}_{oa} = \frac{Y_o + 4Y_r + Y_a}{6}$$
$$\bar{Z}_{ob} = \frac{Z_o + 4Z_s + Z_b}{6} \qquad \bar{Y}_{ob} = \frac{Y_o + 4Y_s + Y_b}{6} \qquad \text{Eq.(C.4)}$$
$$\bar{Z}_{oc} = \frac{Z_o + 4Z_t + Z_c}{6} \qquad \bar{Y}_{oc} = \frac{Y_o + 4Y_t + Y_c}{6}$$

The $\dot{m}$ expressions in Eq.(C.3) result from an assumption that the average element velocity across the link applies at all point locations along the link. Due to the linear interpolation of element velocity within the element, the average velocity is represented by the velocity at the midpoint of the link – Point ***r*** for link $\overline{oa}$, Point ***s*** for link $\overline{ob}$, or Point ***t*** for link $\overline{oc}$. This is why values of $\tilde{U}$ and $\tilde{V}$ were needed only at the Points ***r***, ***s***, and ***t*** on the element links and not at all integration points.

The expressions for $\bar{Z}$ and $\bar{Y}$ in Eq.(C.4) are the result of applying Simpson's Rule. The value of the integrand at the midpoint of the link is more heavily weighted in the integration than the endpoints leading to the factor of 4 on the ***r***, ***s***, and ***t*** terms.

The above expressions allow calculation of integrated fluxes across all links of all elements in the domain without regard to which links form the boundary of which CV. The results of these calculations are the stored λ's which are multipliers for the unknown ϕ values. Assembling an equation of the form Eq.(3.13) for a CV is a matter of recognizing which pair of links from contributing elements forms the boundary of the CV.

However, another step is required in preparation for this assembly process. Looking again at Figure C-1, it is seen that for each element that contributes to a given CV, there are two element links that form part of the CV boundary. The method for assigning the direction of link normals guarantees that one link will have an outward normal and the other will have an inward normal with respect to the CV. The LHS of Eq.(3.6) represents the net *efflux* through the CV boundary. That the net efflux is of interest is significant in that it implies that the link normal for each link forming the boundary of the CV should be outward.

If the CV under consideration is associated with the element's LNN_1, then links $\overline{oc}$ and $\overline{oa}$ form part of the boundary of the CV. With respect to the CV, the normal of $\overline{oc}$ is outward and the normal of $\overline{oa}$ is inward. It can therefore be said that the net efflux through the CV boundary contributed by the element in question is

{flux through $\overline{oc}$}−{flux through $\overline{oa}$}. Similarly, for the CV associated with LNN_2, the total efflux contributed by the element is {flux through $\overline{oa}$}−{flux through $\overline{ob}$}. For the CV associated with LNN_3, the total efflux contributed by the element is {flux through $\overline{ob}$}−{flux through $\overline{oc}$}. These conditions may be expressed in the following equations.

$$\begin{aligned}\Phi_1 &= (\lambda_i^{oc} - \lambda_i^{oa})\phi_i \\ \Phi_2 &= (\lambda_i^{oa} - \lambda_i^{ob})\phi_i \\ \Phi_3 &= (\lambda_i^{ob} - \lambda_i^{oc})\phi_i\end{aligned} \qquad \text{Eq.(C.5)}$$

In Eq.(C.5), Φ_i represents the total efflux contribution from an element to the CV associated with element local node *i*.

If coefficients are defined as

$$\begin{aligned}A'_{1i} &= \lambda_i^{oc} - \lambda_i^{oa} \\ A'_{2i} &= \lambda_i^{oa} - \lambda_i^{ob} \\ A'_{3i} &= \lambda_i^{ob} - \lambda_i^{oc}\end{aligned} \qquad \text{Eq.(C.6)}$$

then an element's contribution to the three CV's associated with it can be represented as

$$\begin{Bmatrix}\Phi_1 \\ \Phi_2 \\ \Phi_3\end{Bmatrix} = \begin{bmatrix}A'_{11} & A'_{12} & A'_{13} \\ A'_{21} & A'_{22} & A'_{23} \\ A'_{31} & A'_{32} & A'_{33}\end{bmatrix}\begin{Bmatrix}\phi_1 \\ \phi_2 \\ \phi_3\end{Bmatrix} \qquad \text{Eq.(C.7)}$$

Eq.(C.7) represents the total efflux contribution of this element to the three CV's associated with it in terms of numerical coefficients and the unknown ϕ values at the element's three nodes.

When the equation for a CV is assembled, it will be of the form

$$a_p\phi_p + \sum_{nb} a_{nb}\phi_{nb} = \iint_A SdA \qquad \text{Eq.(C.8)}$$

For numerical stability, the Scarborough criterion specifies that

$$\frac{\sum|a_{nb}|}{|a_p|} \le 1 \text{ for all equations and } < 1 \text{ for at least one equation} \qquad \text{Eq.(C.9)}$$

If Eq.(C.7) is used to evaluate element contributions to CV's, when the contributions from all contributing elements are added to form the a_i coefficients, in general, the Scarborough criterion will not be met. However, with an adjustment to the original conservation equation, the Scarborough criterion can be met. Rather than subjecting each CV to Eq.(C.8), we will use the modified form of Eq.(C.10).

$$\sum_{i=1}^{m}\left[\int_{link}(\bar{J}^{EV}\cdot\hat{N})dl\right] - \phi_P\int_s \bar{\dot{m}}\cdot\hat{n}ds = \iint_A SdA \qquad \text{Eq.(C.10)}$$

This is the conservation of ϕ_P equation for CV_P in modified form. The second term on the LHS represents the product of ϕ_P and the continuity equation for CV_P. Since the value of $\int_s \bar{\dot{m}}\cdot\hat{n}ds$ is identically zero, the value of the second term is zero and the conservation equation is virtually unchanged from the form in Eq.(C.8). However, Prakash [18] showed that this transforms the resulting Eq.(C.8) into a form such that the coefficients meet the Scarborough criterion for stability.

Rather than assembling the CV equation and then performing the adjustment, the adjustment can be performed at the element level by redefining the diagonal terms in the

A' matrix above. If Π_i is defined as the mass flow rate out of the pair of links associated with local node *i*, and define the product $\Pi_i\phi_i$ as shown in Eq.(C.11),

$$\Pi_i\phi_i = (A'_{i1} + A'_{i2} + A'_{i3})\phi_i \qquad \text{Eq.(C.11)}$$

then subtracting Eq.(C.11) from Eq.(C.7) above results in the following equation.

$$\begin{Bmatrix} \Phi_1 - \Pi_1\phi_1 \\ \Phi_2 - \Pi_2\phi_2 \\ \Phi_3 - \Pi_3\phi_3 \end{Bmatrix} = \begin{bmatrix} A_{11} & A_{12} & A_{13} \\ A_{21} & A_{22} & A_{23} \\ A_{31} & A_{32} & A_{33} \end{bmatrix} \begin{Bmatrix} \phi_1 \\ \phi_2 \\ \phi_3 \end{Bmatrix} \qquad \text{Eq.(C.12)}$$

$$\begin{aligned} A_{11} &= -(A'_{12} + A'_{13}) & A_{12} &= A'_{12} & A_{13} &= A'_{13} \\ A_{22} &= -(A'_{21} + A'_{23}) & A_{21} &= A'_{21} & A_{23} &= A'_{23} \\ A_{33} &= -(A'_{31} + A'_{32}) & A_{31} &= A'_{31} & A_{32} &= A'_{32} \end{aligned} \qquad \text{Eq.(C.13)}$$

Eq.(C.12) represents expressions for the modified efflux of ϕ from the links of a given element to the CV's associated with it. If used consistently for all elements, then upon assembling the CV conservation equations in the form of Eq.(3.13), each equation will meet the Scarborough criteria.

APPENDIX D - CV COEFFICIENT ASSEMBLY PROCESS

A value of ϕ_p is associated with every CV. Its value is influenced directly by the values of ϕ at neighboring nodes. The neighbor nodes for any CV are the nodes forming the elements that contribute to the CV. The ultimate goal is to form an algebraic equation of the form of Eq.(D.1) for each CV.

$$a_P\phi_P + \sum_{nb} a_{nb}\phi_{nb} = b_P \qquad \text{Eq.(D.1)}$$

To form Eq.(D.1) for a CV, the sum of the integrals of flux through the element links forming the boundary is needed. In proceeding, it is assumed that these integrated fluxes have been calculated for all element links in the domain and they are available in the form of Eq.(C.12) for each element. The assembly process is a matter of determining which elements contribute to the CV and which pair of element links from each of these elements form a part of the CV boundary and adding the contributing integrated fluxes.

An element is defined as an ordered set of three global node numbers. Locally, for each element, these are known as 1, 2, and 3. A list of contributing elements for a CV may be assembled by searching the list of all element definitions for the global node number associated with that CV. If the CV number appears in an element's node list, that element contributes to the CV. The position of the CV number in a contributing

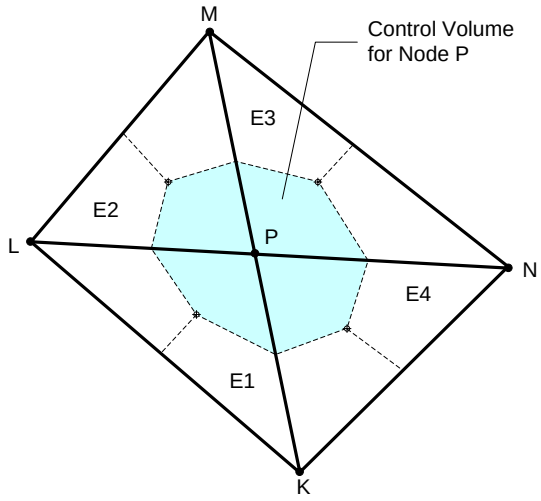

Figure D-1. Typical internal CV formed from four elements.

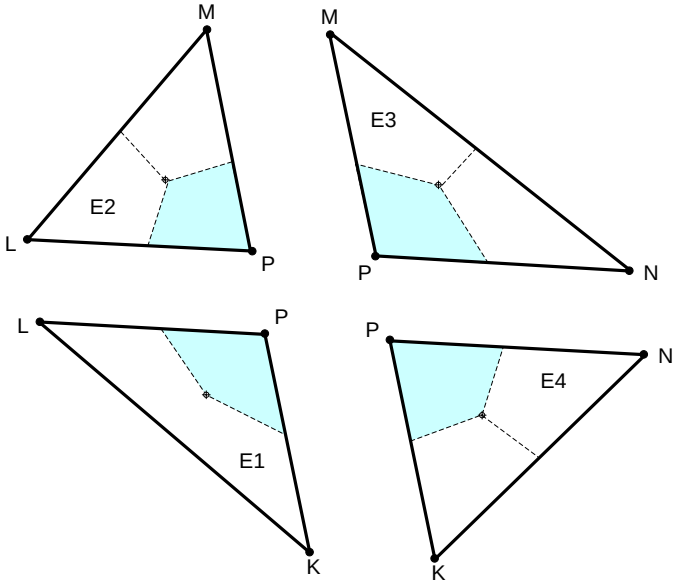

Figure D-2. Exploded view of Figure D-1 showing individual elements.

element's node list determines which expression for flux from Eq.(C.12) is used in the assembly process. This is best illustrated with an example.

Figure D-1 shows an interior CV formed by contributions from four elements. The global node numbers are shown as K, L, M, N, and P with the CV number being P. The neighbors of P are K, L, M, and N and therefore expression for the total efflux is expected to be in terms of ϕ at these nodes.

Figure D-2 shows the four elements in detail. The ordered sets of nodes defining the elements are

$$E_1\{L,\ K,\ P\} \quad E_2\{M,\ L,\ P\} \quad E_3\{P,\ N,\ M\} \quad E_4\{N,\ P,\ K\} \qquad \text{Eq.(D.2)}$$

The element local node numbers come from the placement in the list. For example, for E_1, local node number LNN_1 corresponds to global node number GNN_L, LNN_2 corresponds to GNN_K, and LNN_3 corresponds to GNN_P. So, in the above derivation of Eq.(C.12), the local node numbers are used, but they correspond to GNN's from the element definition.

The assembly process will be illustrated for the internal CV shown in Figure D-1 and Figure D-2. The same process applies for boundary CV's, but additional terms must be added to account for flux through the domain boundary.

For E_1, GNN_P corresponds to LNN_3 . Therefore, the flux contribution from E_1 is given by Eq.(C.12) with $i = 3$.

$$\text{Flux Contribution from } E_1 \text{ to } CV_P = A_{31}^{E_1}\phi_1 + A_{32}^{E_1}\phi_2 + A_{33}^{E_1}\phi_3 \qquad \text{Eq.(D.3)}$$

Eq.(D.3) can be rewritten in terms of GNN's by replacing the subscripts on ϕ's with the corresponding global node number.

$$\text{Flux Contribution from } E_1 \text{ to } CV_P = A_{31}^{E_1}\phi_L + A_{32}^{E_1}\phi_K + A_{33}^{E_1}\phi_P \qquad \text{Eq.(D.4)}$$

Similar expressions can be obtained for the flux contributions from E_2 through E_4 using i=3 for E_2, i=1 for E_3, and i=2 for E_4.

$$\text{Flux Contribution from } E_2 \text{ to } CV_P = A_{31}^{E_2}\phi_M + A_{32}^{E_2}\phi_L + A_{33}^{E_2}\phi_P \qquad \text{Eq.(D.5)}$$

$$\text{Flux Contribution from } E_3 \text{ to } CV_P = A_{11}^{E_3}\phi_P + A_{12}^{E_3}\phi_N + A_{13}^{E_3}\phi_M \qquad \text{Eq.(D.6)}$$

$$\text{Flux Contribution from } E_4 \text{ to } CV_P = A_{21}^{E_4}\phi_N + A_{22}^{E_4}\phi_P + A_{23}^{E_4}\phi_K \qquad \text{Eq.(D.7)}$$

Adding Eq.(D.4) through Eq.(D.7) and gathering terms gives the following expression for the total efflux through the boundary of CV_P.

$$\begin{aligned} \text{Total Efflux} &= a_P\phi_P + a_L\phi_L + a_M\phi_M + a_N\phi_N + a_K\phi_K \\ a_P &= A_{33}^{E_1} + A_{33}^{E_2} + A_{11}^{E_3} + A_{22}^{E_4} \\ a_L &= A_{31}^{E_1} + A_{32}^{E_2} \\ a_M &= A_{31}^{E_2} + A_{13}^{E_3} \\ a_N &= A_{12}^{E_3} + A_{21}^{E_4} \\ a_K &= A_{32}^{E_1} + A_{23}^{E_4} \end{aligned} \qquad \text{Eq.(D.8)}$$

Comparing Eq.(D.8) to the LHS of Eq.(D.1), a_L, a_M, a_N, and a_K are recognized as the a_{nb}'s.

The above process may be performed on each CV in the domain and a corresponding equation of the form of Eq.(D.1) derived. For internal CV's, the total efflux through the CV boundary is represented by the LHS of Eq.(D.8). For boundary CV's, additional terms are required.

APPENDIX E – INTERPOLATION FUNCTION FOR PRESSURE *(P)*

Pressure is assumed to vary linearly within elements. For linear interpolation, one may choose to work with the domain global coordinate system or the element local coordinate system. Choosing the domain global coordinate system for pressure interpolation allows calculation of the coefficients one time rather than during each solution iteration. (In general, the element local coordinate system changes with each iteration as the values of element velocity are updated.)

It is assumed that the pressure variation within an element may be described by an equation of the form

$$P(x, y) = Ax + By + C \qquad \text{Eq.(E.1)}$$

By applying the constraint that Eq.(E.1) is valid at each of an element's three nodes, the following set of three equations is obtained

$$\begin{aligned} P_1 &= Ax_1 + By_1 + C \\ P_2 &= Ax_2 + By_2 + C \\ P_3 &= Ax_3 + By_3 + C \end{aligned} \qquad \text{Eq.(E.2)}$$

Similar to the discussion of the interpolation function for ϕ in Appendix B, neither the *P*'s nor the coefficients *A, B,* or *C* are known. However, by considering the *P*'s to be knowns, the coefficients to be unknowns, and solving for the coefficients in terms of the *P*'s, the expressions for the coefficients take the following form.

$$\begin{aligned} A &= A_1P_1 + A_2P_2 + A_3P_3 \\ B &= B_1P_1 + B_2P_2 + B_3P_3 \\ C &= C_1P_1 + C_2P_2 + C_3P_3 \end{aligned} \qquad \text{Eq.(E.3)}$$

$$A_1 = \frac{(y_2 - y_3)}{DET_P} \qquad A_2 = \frac{(y_3 - y_1)}{DET_P} \qquad A_3 = \frac{(y_1 - y_2)}{DET_P} \qquad \text{Eq.(E.4)}$$

$$B_1 = \frac{(x_3 - x_2)}{DET_P} \qquad B_2 = \frac{(x_1 - x_3)}{DET_P} \qquad B_3 = \frac{(x_2 - x_1)}{DET_P} \qquad \text{Eq.(E.5)}$$

$$C_1 = \frac{(x_2 y_3 - x_3 y_2)}{DET_P} \qquad C_2 = \frac{(x_3 y_1 - x_1 y_3)}{DET_P} \qquad C_3 = \frac{(x_1 y_2 - x_2 y_1)}{DET_P} \qquad \text{Eq.(E.6)}$$

$$DET_P = x_1(y_2 - y_3) + x_2(y_3 - y_1) + x_3(y_1 - y_2) \qquad \text{Eq.(E.7)}$$

Eq.(E.1) in conjunction with Eq.(E.3) through Eq.(E.7) gives the pressure at any location (*x*, *y*) within the element. However, this is not particularly helpful in formulating the equations to solve for nodal pressures.

Recall that $\partial P/\partial x$ and $\partial P/\partial y$ appear in the source integrals for the momentum equations. Differentiating Eq.(E.1) with respect to *x* and then separately with respect to *y*, the following expressions for the derivatives are obtained.

$$\frac{\partial P}{\partial x} = A = A_1 P_1 + A_2 P_2 + A_3 P_3 \qquad \text{Eq.(E.8)}$$

$$\frac{\partial P}{\partial y} = B = B_1 P_1 + B_2 P_2 + B_3 P_3 \qquad \text{Eq.(E.9)}$$

The nodal pressures appear explicitly in the above expressions for the derivatives. These expressions in conjunction with the continuity equation may be used to derive CV conservation equations which may be solved for nodal pressures.

VITA

Name: Tracy Leo Fullerton

Address: Texas A&M University
Department of Mechanical Engineering
3123 TAMU
College Station TX 77843-3123

Email Address: TLFullerton@verizon.net

Education: B.S., Mechanical Engineering, Texas Tech University, 1986
M.S., Mechanical Engineering, Texas Tech University, 1988
Ph.D., Mechanical Engineering, Texas A&M University, 2011